

REPORT DOCUMENTATION PAGE

Form Approved
OMB No. 0704-0188

Public reporting burden for this collection of information is estimated to average 1 hour per response, including the time for reviewing instructions, searching existing data sources, gathering and maintaining the data needed, and completing and reviewing the collection of information. Send comments regarding this burden estimate or any other aspect of this collection of information, including suggestions for reducing this burden, to Washington Headquarters Services, Directorate for Information Operations and Reports, 1215 Jefferson Davis Highway, Suite 1204, Arlington, VA 22202-4302, and to the Office of Management and Budget, Paperwork Reduction Project (0704-0188), Washington, DC 20543.

1. AGENCY USE ONLY (Leave blank) 2. REPORT DATE 7 Sep 1989 3. REPORT TYPE AND DATES COVERED Final Report/1 Nov 87-31 Jan 89

4. TITLE AND SUBTITLE
Experimental Testing of Corpuscular Radiation Detectors
Vol I ~~II~~

5. FUNDING NUMBERS
62714E/5261/02
62714E/5261/03
62702E/5261/04

6. AUTHOR(S)
Mario D. Grossi
AD-A217 506

7. PERFORMING ORGANIZATION NAME(S) AND ADDRESS(ES)
Raytheon Company
Submarine Signal Division
Portsmouth, RI 02871

8. PERFORMING ORGANIZATION REPORT NUMBER
AFOSR TR. 89-1675

9. SPONSORING / MONITORING AGENCY NAME(S) AND ADDRESS(ES)
AFOSR/NP
Bolling AFB DC 20332-6448

10. SPONSORING / MONITORING AGENCY REPORT NUMBER
F49620-87-C-0050

11. SUPPLEMENTARY NOTES

12a. DISTRIBUTION / AVAILABILITY STATEMENT
Approved for public release; distribution is unlimited.

12b. DISTRIBUTION CODE

13. ABSTRACT (Maximum 200 words)
Computer simulation has been performed showing the magnitude of the neutrino signal from a 100 kilocurie tritium source, under the geometrical conditions of the experiments at Los Angeles National Laboratory, TA-33, is about an order of magnitude smaller than the gravity signal from a 2600 gr mass (the assumed value for the mass of the source). The observations were performed by using Professor Joe Weber's torsion balance, a room-temperature instrument.

DTIC
ELECTE
JAN 12 1990
S D

14. SUBJECT TERMS
torsion balance, neutrino signal, kilocurie tritium source

15. NUMBER OF PAGES
405

16. PRICE CODE

17. SECURITY CLASSIFICATION OF REPORT
UNCLASSIFIED

18. SECURITY CLASSIFICATION OF THIS PAGE
UNCLASSIFIED

19. SECURITY CLASSIFICATION OF ABSTRACT
UNCLASSIFIED

20. LIMITATION OF ABSTRACT
UL
SAR

GENERAL INSTRUCTIONS FOR COMPLETING SF 298

The Report Documentation Page (RDP) is used in announcing and cataloging reports. It is important that this information be consistent with the rest of the report, particularly the cover and title page. Instructions for filling in each block of the form follow. It is important to *stay within the lines* to meet optical scanning requirements.

Block 1. Agency Use Only (Leave blank).

Block 2. Report Date. Full publication date including day, month, and year, if available (e.g. 1 Jan 88). Must cite at least the year.

Block 3. Type of Report and Dates Covered. State whether report is interim, final, etc. If applicable, enter inclusive report dates (e.g. 10 Jun 87 - 30 Jun 88).

Block 4. Title and Subtitle. A title is taken from the part of the report that provides the most meaningful and complete information. When a report is prepared in more than one volume, repeat the primary title, add volume number, and include subtitle for the specific volume. On classified documents enter the title classification in parentheses.

Block 5. Funding Numbers. To include contract and grant numbers; may include program element number(s), project number(s), task number(s), and work unit number(s). Use the following labels:

C - Contract	PR - Project
G - Grant	TA - Task
PE - Program Element	WU - Work Unit Accession No.

Block 6. Author(s). Name(s) of person(s) responsible for writing the report, performing the research, or credited with the content of the report. If editor or compiler, this should follow the name(s).

Block 7. Performing Organization Name(s) and Address(es). Self-explanatory.

Block 8. Performing Organization Report Number. Enter the unique alphanumeric report number(s) assigned by the organization performing the report.

Block 9. Sponsoring/Monitoring Agency Name(s) and Address(es). Self-explanatory.

Block 10. Sponsoring/Monitoring Agency Report Number. (If known)

Block 11. Supplementary Notes. Enter information not included elsewhere such as: Prepared in cooperation with...; Trans. of...; To be published in.... When a report is revised, include a statement whether the new report supersedes or supplements the older report.

Block 12a. Distribution/Availability Statement. Denotes public availability or limitations. Cite any availability to the public. Enter additional limitations or special markings in all capitals (e.g. NOFORN, REL, ITAR).

DOD - See DoDD 5230.24, "Distribution Statements on Technical Documents."

DOE - See authorities.

NASA - See Handbook NHB 2200.2.

NTIS - Leave blank.

Block 12b. Distribution Code.

DOD - Leave blank.

DOE - Enter DOE distribution categories from the Standard Distribution for Unclassified Scientific and Technical Reports.

NASA - Leave blank.

NTIS - Leave blank.

Block 13. Abstract. Include a brief (Maximum 200 words) factual summary of the most significant information contained in the report.

Block 14. Subject Terms. Keywords or phrases identifying major subjects in the report.

Block 15. Number of Pages. Enter the total number of pages.

Block 16. Price Code. Enter appropriate price code (NTIS only).

Blocks 17. - 19. Security Classifications. Self-explanatory. Enter U.S. Security Classification in accordance with U.S. Security Regulations (i.e., UNCLASSIFIED). If form contains classified information, stamp classification on the top and bottom of the page.

Block 20. Limitation of Abstract. This block must be completed to assign a limitation to the abstract. Enter either UL (unlimited) or SAR (same as report). An entry in this block is necessary if the abstract is to be limited. If blank, the abstract is assumed to be unlimited.

Raytheon

AFOSR-TR. 89-1675

Final Report

**Experimental Testing of
Corpuscular Radiation
Detectors**

Submitted to:

**Defense Advanced Research
Project Agency (DARPA)**

DARPA Order No. 5271
Contract No. F49620-87-C-0050

Monitored by Air Force Office of
Scientific Research (AFOSR)

DARPA Program Director:
U.S. Army Lt. Col. G. P. Lasche', Ph.D

7 September 1989

Raytheon Company
Submarine Signal Division
1847 West Main Road
Portsmouth, RI 02871-1087 U.S.A.
Telephone (401) 847-8000

CN-RA-064

VOLUME I
TABLE OF CONTENTS

Section	Page
Acknowledgements.....	ii
Executive Summary.....	iii
1. Computer Simulation of Experiments with Weber Torsion Balance.....	1
2. Experimental Activity at LANL with Weber Torsion Balance.....	52
2.1 Instrumentation System.....	52
2.2 Calibration of Overall Instrumentation System.....	63
2.3 Report on the Results of Data Acquisition, Real-Time Data Processing and Analysis.....	71
3. The Cryogenic Force Sensor.....	82
4. Laboratory Tests on the Feasibility of the Magnetic Sensor.....	94
5. Conclusions and Recommendations.....	99
6. Bibliographic References.....	101
APPENDIX A- On the Scattering of X-rays and Neutrinos in Crystals; A Comparative Theoretical Study, by R.R. Lewis.....	A-1
ADDENDUM TO APPENDIX A- Added Comments on the Original Report (Appendix A), by R.R. Lewis.....	A-25
APPENDIX B- Estimate of X-ray Scattering from Crystals, by R.R. Lewis..	B-1
APPENDIX C - Comments on the Results of the Measurements Carried Out at LANL/TA-33 during Fall 1988, by M.D.Grossi.....	C-1



Accession For	
NTIS CRA&I	<input checked="" type="checkbox"/>
DTIC TAB	<input type="checkbox"/>
Unannounced	<input type="checkbox"/>
Justification	
By _____	
Distribution /	
Availability Codes	
Dist	Availability or Special
A-1	

ACKNOWLEDGEMENTS

This Final Report has been prepared by Mario D. Grossi, Principal Investigator, with inputs from all members of the program team. For each Section, credit is given to the writer who contributed it.

*** *** ***

Raytheon Company, Submarine Signal Division, Portsmouth, RI, was the Prime Contractor for this program. Raytheon PMO wishes to acknowledge the contributions of two major Subcontractors :Smithsonian Astrophysical Observatory (SAO), Cambridge, Massachusetts, and University of Maryland, Department of Physics, College Park, Maryland. In addition, we wish to express our appreciation to LANL-WX5, Los Alamos, NM, for having provided to the project laboratory space in Technical Area TA-33, and for having manufactured the tritium-filled source and the deuterium-filled reference, used in the tests illustrated in this Report. Special thanks to H. Richard Maltrud for the competent technical assistance and for the hospitality extended to Program personnel at TA-33.

EXECUTIVE SUMMARY

This Final Report, issued in two Volumes, is a self-contained documentation of the overall activity that Raytheon has performed under the terms of Contract F49620-87-C-0050. Volume I illustrates the program accomplishments in the most important, conclusive period of contract performance, from August 1988 through January 1989. Volume II is a collection of five Quarterly Reports, published by Raytheon to illustrate project activity between August 1987 and August 1988.

These past six months have been of great importance for the project, because of the availability of tritium sources of neutrinos at LANL, Los Alamos, NM. This has made it possible to acquire data of scientific value, and to answer some of the questions that had motivated the conduct of the investigation. These data were processed and analyzed at LANL, in real time, making it possible to draw immediate conclusions about the meaning of the measurements. The observations were performed by using Prof. Joe Weber's torsion balance, a room-temperature instrument that was constructed by University of Maryland under a subcontract from Raytheon, and was installed at LANL in Summer 1988. The torsion balance was mounted at a fixed location, close to the edge of a rotating table (1 RPM rotational speed) that Raytheon had constructed and moved to Los Alamos, NM. As the table rotated, the tritium-filled container (neutrino source) and the deuterium-filled container (that provided a "newtonian force" reference) were sensed by the instrument. At the time of writing of this Report, the results of the measurements are not fully conclusive. A six-month Contract extension, expected to last until 31 December 1989, will provide the final answer whether or not we could observe repulsion forces, attributable to neutrino pressure, with the torsion balance.

The experiment consisted, basically, of a comparison between the following two functions: (1) output of the torsion balance, integrated for 168 hours, with a deuterium-filled sphere mounted on the table (deuterium is non-radioactive, and the only forces applied to the torsion balance were newtonian attractions); and, (2) output of the same instrument, again integrated for 168 hours, with a tritium-filled sphere now mounted on the table (providing a newtonian attraction force because of its mass, with this force decreased by a repulsion force due to the hypothesized neutrino radiation pressure). The quality of the measurements was affected negatively by the following causes:

(1) The torsion balance is characterized by a very small damping factor (about 6%), while it would be advisable to operate with critical damping (a factor of 100%). As a consequence, once excited, the oscillation train lasts well beyond the 60-second period of table rotation, and interferes with the signal of the next table rotation.

(2) The torsion balance has an oscillation period (about 14 seconds) dependent upon room temperature. We noticed changes of about 5% from Summer to Winter 1988-1989. Fortunately, these changes in period were slow enough that the effect could be minimized by applying a numerical correction to the recorded outputs, after computer integration.

(3) The output of the torsion balance exhibits a DC drift from -10 V to + 10V (a full cycle in about two months). The required signal, characterized by a very small amplitude \pm (10 microVolt-to-100 microVolt), is on top of this slowly varying drift. By using a 16 bit resolution in the digitization process (instead of the 12 bit resolution of Prof. Weber's earlier tests), we were able to detect the signal most of the time.

Once the relevance of these torsion balance difficulties was fully appreciated, Raytheon (with the concurrence of Prof. Joe Weber) submitted a recommendation to DARPA to extend the present phase of the project for three-to-six months. This would at least, provide a new damper (characterized by critical, or near-critical, damping) and a thermal control subsystem for the instrumentation. Then the data collection could be resumed with 26 source-replicas mounted on the top of the 1 RPM table. LANL is already proceeding, under direct DARPA funding, to fabricate these 26 replicas and to mount them around the rim of the 1 RPM rotating table, in order to maximize the ratio "repulsion force/attractive force". The repulsion force represents the desired signal, and the attractive force, due to gravity-gradient background, the undesired one. Computer simulations, carried out at SAO under a Raytheon subcontract, have shown that, with this arrangement, we could expect an improvement in the ratio "repulsive force/attractive force" of 500-1000.

Thus far, data have been collected by Raytheon without using the 26 replicas. With all applicable caveats, we could draw the following tentative conclusions (we cannot stress strongly enough how tentative our current results are):

(1) There is a difference between the recordings (obtained with 168 hours integration time) performed with tritium and with deuterium. This difference would be consistent with a repulsion force which is present when experimenting with the tritium. The intensity of this repulsion force appears to be of a few microdynes. This tracks closely Prof. Weber's observations at U. of Maryland in 1986;

(2) If a 1/4" lead shield is wrapped around the 8" diameter cylinder that houses the torsion balance, this repulsion force seems to disappear;

(3) Observations (1) and (2) above have been performed only once, and the SNR was rather limited. That is why we say that the experimental evidence is, thus far, most tentative. Should these results be confirmed by the forthcoming tests during the contract extension, the question will arise as to the origin of a radiation pressure that produces a torsion balance force that disappears when a lead shield is interposed between source and sensor. We do not expect that this question will be easy to answer. A first candidate radiation that comes to mind is X-ray radiation. However, where do these X-rays come from? They cannot come from the inside of the tritium container: the thickness of its wall is too large to allow even the smallest leak. Another possible mechanism has been proposed that would generate 14.1 MeV neutrons, that, in turn, could produce secondary radiation affecting the torsion balance. Clearly, we need to add new sensors to our instrumentation at LANL such as a proportional counter, a X-ray detector, a gamma-ray detector, a neutron spectrometer, etc. Dependent upon the results of the measurements above, we could interpose shields between source and torsion balance, such as: (a) IR shield made of several layers of gold-coated mylar, each with 95% reflection coefficient in the IR band, or an equivalent shield; (b) Magnetic shield (several layers of flexible Permag metglass); (c) 1/4" lead shield, against X-rays; (d) Cadmium/boron/lead shield against 14 MeV neutrons.

* * *

In addition to the experimental activity that Raytheon has carried out at LANL with the torsion balance, we have constructed and tested in Portsmouth, RI (without using tritium sources of neutrinos, thus far) a cryogenic force sensor that has exhibited a sensitivity of about 10^{-9} dyne in 10^4 seconds integration time. Testing this cryogenic instrument (that operates at 4°K, is tuned at 100 Hz, and is suspended from a tripod equipped with a 2-stage vibration isolator) at

LANL requires a 2000 RPM rotating table, with three tritium sources mounted on the table top, 120° apart, to modulate the neutrino flux amplitude at 100 Hz. This table has not yet been built, although an analysis of its feasibility and a preliminary design have been completed by Raytheon and SAO.

Should the tests with the torsion balance, to be completed by December 1989, provide support to Prof. Weber's expectation of an abnormally large coherent scattering cross-section using tritium-radiated neutrinos, we would then have a simpler and cheaper alternative for the 100 Hz modulation of neutrino flux. This would consist of a modified Weber chopper, rotating at 100/n RPS, where n is the number of sapphire crystals mounted at the periphery of the rotating disk. The chopper could be used at LANL with a tritium source kept at a fixed station, on a stand. By replacing the tritium source with a deuterium-filled container, we could verify whether a tritium-induced signal would continue to be present, or would disappear, when using the deuterium.

The cryogenic force sensor that Raytheon has constructed provides a sensitivity improvement of more than 4 orders of magnitude with respect to the room-temperature torsion balance, thus reaching a threshold of less than 10^{-10} dynes, with a 168-hour integration time. The instrument has the potential of achieving a sensitivity of the order of a picodyne (10^{-12} dynes), by adding cryostat dilution refrigeration provisions, which would bring the operating temperature down to 4 milli°K.

* * *

Finally, concerning the laboratory tests on the feasibility of the magnetic interaction sensor, Raytheon has constructed a SQUID magnetometer under the 1988 Independent Development

Program (IDP), and has performed the following measurements, as contractually required:

(1) Determination of the SQUID system noise (this is called intrinsic noise, when the SQUID is unloaded): for frequencies larger than 10 Hz, our SQUID has an intrinsic noise of about $10^{-6} \phi_0 \text{ Hz}^{-1/2}$ (where $\phi_0 = 2.07 \cdot 10^{-15} \text{ Wb}$). This is a factor of 10 better than commercially available SQUIDs. However, we need a noise level less than, or equal to, $10^{-7} \phi_0 \text{ Hz}^{-1/2}$, when the SQUID is loaded by the target. Therefore, we have still a long way to go. JASON estimated that a loaded SQUID would have, at best, a system noise of $10^{-4} \phi_0 \text{ Hz}^{-1/2}$.

(2) Determination of the maximum achievable relative permeability for the interaction target. We have measured a $\mu_r = 10^6$, when operating on the steep side of the hysteresis cycle. We require $\mu_r = 10^8$. We have still a factor of 100 to gain. JASON had estimated that at best we could achieve a $\mu_r = 10^3$.

(3) Determination of the maximum achievable collecting area. We need 10^3 cm^2 . Our SQUID stopped operating with a 15 cm^2 area. JASON had estimated that at best we could achieve 1 cm^2 . Here also, we have a factor of 100 to gain. The use of a superconducting transformer offers great promise.

Our estimate of the effort that is required to complete the preliminary laboratory tests on the three basic JASON questions concerning magnetic sensor feasibility is as follows: (a) Laboratory work on SQUID improvement and on target testing, still using a 1 Kg mass for the high-permeability interaction target, will require about 3 man-years effort over a 1 year period. (This work does not require tritium sources and can be carried out at Raytheon, Portsmouth, RI);

(b) Completion of the SQUID improvement program, and laboratory work with a 25 Kg interaction target, will require about 4 man-years effort over a 1 year period (work still to be done in Portsmouth, RI).

Should the answers to the three JASON questions provide support for sensor feasibility, we could then move toward a program phase that includes construction of the actual sensor. This would be used at LANL/TA-33 with tritium sources of neutrinos (this instrument would use a 250 Kg interaction target, housed in a custom-made 4°K cryostat) for the conduct of fully-probative detection experiments.

Concerning an assessment of the likelihood of success, we must distinguish between two goals. Achieving the three goals in the instrumentation subsystem performance identified by JASON, could be characterized, in Raytheon's opinion, as better than 50%, while the probability of detecting neutrinos with the magnetic sensor cannot yet be assessed at this time. Notwithstanding this uncertainty, our strong recommendation is that support be provided by DARPA to build up, item by item, the technology basis that is a pre-requisite to fully develop this novel detector of low-energy neutrinos.

1. COMPUTER SIMULATION OF THE EXPERIMENTS WITH WEBER TORSION BALANCE(*)

1.1 Summary Of The Results

The computer simulations that we have performed show that the magnitude of the neutrino signal from a 100 kilocurie tritium source, under the geometrical conditions of the experiments at LANL, TA-33, is about an order of magnitude smaller than the gravity signal from a 2600 gr mass (the assumed value for the mass of the source). When the crystal of sapphire is closest to the rotating table (the so-called 180° case), the gravity and neutrino torques have similar shapes vs. time but opposite sign. At this orientation it is difficult to distinguish the neutrinos signal from a change in scale factor. In the so-called 90° case, the neutrino signal does not reverse sign so that the pulse shape is different from that of the gravity torque. Because the torsion balance is weakly damped, the response does not show the actual pulse shape. The response is dominated by the natural oscillation period of the torsion balance. If the rotating wheel is filled with a ring of balls of equal mass, the gravity signal is virtually eliminated with only a very small high-frequency ripple remaining. If the masses have a 1 percent random error, the noise

(*)Contributed by David A. Arnold, SAO

due to gravity is about 1 percent of the signal due to a single ball. If the mass errors are distributed along the rim by pairing light and heavy balls, the noise goes down by another factor of 3-5 so that it is a factor of 300-500 less than the signal of a single mass.

1.2 Computer Model Of The Weber Torsion Balance

The Weber torsion balance has been modelled as a one degree of freedom rotating object having a moment of inertia I , restoring stiffness k and damping coefficient b . The restoring stiffness and damping are provided electronically using two electrostatic plates. The torsion balance is cylindrically symmetric except for 4 masses placed on the balance. Two of these are a sapphire crystal in a holding structure and a lead weight of equal mass mounted opposite the crystal in another holding structure. The 4 masses can apply gravitational torques to the balance, and the crystal is modelled as being sensitive to neutrino radiation pressure.

The torsion balance has various cylindrical parts. The moment of inertia I of a cylinder of radius R , length ℓ , and density ρ is given by

$$I = \int dm r^2 \quad (1)$$

where

$$dm = 2\pi r \ell \rho dr \quad (2)$$

Substituting equation (2) into (1) gives

$$I = 2\pi \ell \rho \int r^3 dr \quad (3)$$

Integrating from $r = 0$ to R gives

$$I = 2\pi \ell \rho \frac{R^4}{4} = \frac{\pi \ell \rho R^4}{2} \quad (4)$$

The major cylindrical part is an aluminum disc 5" in diameter, and .314 inches in thickness. With $\rho = 2.6989 \text{ g/cm}^3$ equation (4) gives $I = 5497.5 \text{ g-cm}^2$. The next largest cylindrical part is a rod 1" in diameter and 1.25" in length. The moment of inertia from equation (4) is 35 g-cm^2 . A third piece of rod is $5/8$ " in diameter and $3/4$ " long with a moment of inertia 3.2 g-cm^2 , and a fourth is $1/2$ " in diameter, and 2.032" long with a moment of inertia 3.5 g-cm^2 . The total for these 4 parts is 5539.2 g-cm^2 .

The electrostatic plates extend from 1-1/4 inches to the edge of the disc at 2.5 inches. These are 1-3/8 inches high and .25 inches thick with a total mass of 19 grams. The length of the plates is 1-1/4 inches and the mass per unit length is $\sigma = 5.985 \text{ g/cm}$. The

moment of inertia of the plate is

$$I = \int \sigma r^2 dr = \frac{1}{3} \sigma (R_2^3 - R_1^3) \quad (5)$$

With $R_1 = 1\frac{1}{4}$ " and $R_2 = 2.5$ ", equation (5) gives 447 g-cm². For comparison, the moment of inertia computed as

$$I = M\bar{r}^2 \quad (6)$$

with $\bar{r} = 1.875$ " gives $I = 431$ g-cm².

The sapphire crystal and lead weight each have a mass of 26 grams. The holding structure is 14.3 grams for a total of 40.3 grams. These two masses are at a radius of 3" giving a moment of inertia for each of 2340 g-cm² using equation (6). The actual moment of inertia considering the distributed mass is larger. However, it has not been calculated, as the value above is considered adequate for the purpose of this report.

The total moment of inertia for the electrostatic plates, crystal and lead mass is $2 (447+2340) = 5574$ g-cm². Adding 5539 g-cm² for the cylindrical parts, gives a total of 11,113 g-cm². The

uncertainties in the basic data used for the calculations are estimated by Prof. Weber to be of the order of 10^{-1} g for the masses and 10^{-1} cm for the distances. Consequently, the error in determining the moment of inertia of 11,113 g-cm² is only 0.6%. This error is clearly negligible, and our computer simulation was carried out by adopting this value for the moment of inertia.

The moment of inertia is involved only in the dynamical calculations. The response to a static force does not depend on the moment of inertia. The torque on the system does, however, depend on the exact distribution of mass so that both the dynamic and static response require knowing the detailed geometry of the torsion balance.

The next parameter needed in the analysis is the stiffness k . This is determined by the electronics used to control the voltage on the electrostatic plates. The value of the stiffness was inferred from the period of the natural oscillations, observed to be around 14 seconds. In the simulations k has been assigned a nominal value of 2222 dyne-cm/radian. Using the equation

$$\omega = \sqrt{\frac{k}{I}} \quad (7)$$

with $I = 11,000$ gives $\omega = .44944$ rad/sec which is a period of 13.98 seconds.

The damping b in the electronics was inferred from the $1/e$ decay time, observed to be about 39 seconds. Since the decay of the amplitude is given by

$$A = e^{-\alpha t} \quad (8)$$

we have that $\alpha t = 1$ or

$$\alpha = \frac{1}{t} = \frac{1}{39} = .02564 \quad (9)$$

The critical damping coefficient for a simple harmonic oscillator is

$$b_c = 2\sqrt{Ik} \quad (10)$$

and the decay of the amplitude is given by

$$A = e^{-\frac{bc}{2I}t} \quad (11)$$

Substituting equation (10) into equation (11) gives

$$A = e^{-\sqrt{\frac{k}{I}}t} \quad (12)$$

Substituting equation (7) into equation (12) gives

$$A = e^{-\omega t} \quad (13)$$

for critical damping. Comparing equations (13) and (8) we see that the ratio of the actual damping to critical damping is α/ω . Since $\omega = .44944$ rad/sec and α is given by equation (9), the damping ratio is

$$\frac{\alpha}{\omega} = \frac{.02564}{.44944} = .057 \quad (14)$$

In the simulation a nominal value of 6% of critical damping has been used to approximate the behavior of the system. Parametric studies with 50% and 100% of critical damping have also been done.

In computing the gravitational force, the four masses of the disk have been treated as point objects. To take into account their actual mass distribution would complicate substantially the analysis, and we do not believe that it would modify appreciably the results. We will verify this point in the proposed follow-on effort, that includes a task devoted specifically to this issue.

The radial distance used for the electrostatic plates is 1.875" or 4.76 cm, and that of the crystal and lead weight is 3" or 7.62 cm. The angle between crystal and electrostatic plates is 67.5° (information received from U. of Maryland). In the simulations, the angles of the masses, measured counterclockwise, have been given the following values:

Table 1

m_1 (lead mass)	0°
m_2 (electrostatic plate)	67.5°
m_3 (crystal)	180°
m_4 (electrostatic plate)	202.5°

Table 1. Angular position of the masses on the torsion balance.

A diameter of 3/4" has been used for the crystal in the simulations. This is a cross-sectional area of 2.85 cm². The dimensions of the crystal have not been physically measured by us. A nominal value of 2.85 cm² for the crystal cross section has been provided to us by the U. of Maryland.

In the proposed follow-on effort, we plan to verify ourselves the dimensions of the crystal, and to include in the analysis the variation of the crystal's cross-section, as a function of the angle of incidence of neutrino radiation, while the 1 RPM table rotates.

1.3 Gravitational and Radiation Torques on the Torsion Balance

In the neutrino experiment, a sphere containing tritium is rotated on a wheel located close to the torsion balance. The sphere has holding and filling structures such that the center of mass of the unit does not coincide with the center of the sphere. Figure 1 shows the geometry of the experimental setup. The center of the sphere is located at a distance R_N from the center of the rotating wheel. The center of mass of the sphere plus its holding structure is located at a distance R_G . The gravitational force attracts all four masses in the torsion balance. The distance to mass m_2 is \vec{R}_{2G} . The radiation is assumed to act only on the sapphire crystal. The distance is \vec{R}_{3N} . The gravitational force on mass i is

$$\vec{F}_{iG} = -GM \frac{m_i}{|\vec{R}_{iG}|^3} \vec{R}_{iG} \quad (15)$$

where M is the mass of the sphere plus associated structures, and $G = 6.67 \times 10^{-8}$ cgs is the gravitational constant. A value of 2600 g has been used for M in the simulations. The force due to radiation pressure on the crystal is calculated using the equation

$$\vec{F}_N = j \frac{E_\nu}{c} A \frac{\vec{R}_{3N}}{|\vec{R}_{3N}|} \quad (16)$$

where j is the number of incident particles per unit area, A is the cross section of the crystal, E_ν is the energy per particle, c is the speed of light, and \vec{R}_{3N} is the vector from the center of the sphere to the crystal. The flux j is

$$j = \frac{N}{4\pi |R_{3N}|^2} \quad (17)$$

where N is the number of neutrinos per second generated by the tritium. Substituting equation (17) into equation (16) gives

$$\vec{F}_N = \frac{N E_\nu A}{4\pi c |R_{3N}|^3} \vec{R}_{3N} \quad (18)$$

$$\vec{F}_N = C_N \frac{A}{|R_{3N}|^3} \vec{R}_{3N} \quad (19)$$

where

$$C_N \equiv \frac{N E_\nu}{4\pi c} \quad (20)$$

In the simulations, the values used for the constants in equation (20) are

$$N = 3.4 \times 10^{15} / \text{sec} \quad (21)$$

$$E_\nu = 1.6 \times 10^{-8} \text{ergs} \quad (22)$$

$$c = 3 \times 10^{10} \text{cm} / \text{sec} \quad (23)$$

Using these values gives

$$C_N = 1.44 \times 10^{-4} \quad (24)$$

The forces given by equation (15) and (19) produce torques on the torsion balance. The total torque produced in

$$\tau = \vec{r}_3 \times \vec{F}_N + \sum_{i=1}^4 \vec{r}_i \times \vec{F}_{iG} \quad (25)$$

In the second quarterly report for this contract dated 16 November 1987 there is a description of program *FLYWHEEL* which computes the force on a detector from a set of radiation sources located on a rotating wheel. This program has been modified to compute the torque on the Weber torsion balance using equation (25). The third quarterly report dated February 1988 describes a program called *DETECT* that was written to calculate the response of a high Q mechanical oscillator to the signal produced by a set of radiation sources on a rotating wheel. Program *DETECT* uses the same equations as program *FLYWHEEL* for calculating the force on the detector. Program *DETECT* has been modified to calculate the motion of the Weber torsion balance in response to the torque given by equation (25).

1.4 Results of the Computer Simulations

A set of computer runs has been done using programs *FLYWHEEL* and *DETECT* to simulate the neutrino experiment which uses a tritium source on the 1 RPM rotating wheel and the Weber torsion balance containing a sapphire crystal. Runs have been done for two orientations of the torsion balance as shown in Figure 2. The rotating wheel is to the left. Figure 2a corresponds to the orientation shown in Figure 1 and the angles of the masses listed in Table 1. In Figure 2b the torsion balance has been rotated clockwise by 90°. The solid circle represents the crystal, the open circle the lead weights, and the thin boxes the electrostatic plates. All the experiments done to date use the orientation shown in Figure 2a labelled 180°.

Table 2 shows the values of the parameters used in the computer simulations. Certain parameters such as the orientation θ of the torsion balance, the number of balls on the rotating wheel, and the damping ratio b/b_c vary from run to run. The damping ratio applies only to the angles computed by program *DETECT*.

Moment of Inertia $I = 11000 \text{ g-cm}^2$

Restoring stiffness $k = 2222 \text{ dyne-cm/radian}$

Angular velocity of wheel $\Omega = .104720 \text{ rad/sec (1 RPM)}$

Radius of center of gravity $R_G = 37.59 \text{ cm}$

Radius of center of radiation $R_N = 39.08 \text{ cm}$

Distance from center of wheel to center of torsion balance
 $D = 63.5 \text{ cm}$

Mass of ball & holder $M = 2600 \text{ g}$

Gravitational constant $G = 6.67 \times 10^{-8} \text{ cgs}$

Neutrino constant (see equation 20) $C_N = 1.44 \times 10^{-4}$

Radius of electrostatic plates $r_2 = r_4 = 4.76 \text{ cm}$

Radius of crystal & lead weight $r_1 = r_3 = 7.62$

Mass of electrostatic plates $m_2 = m_4 = 19 \text{ g}$

Mass of crystal & lead weight $m_1 = m_3 = 40.3 \text{ g}$

Cross section of crystal $A = 2.85 \text{ cm}^2$

Table 2. System Parameters

Figure 3 shows three runs using program *FLYWHEEL* to compute the torque on the torsion balance with one source and the detector (torsion balance) at 180° (crystal closest to the rotating wheel). Part a) is the torque due to the gravity of the ball, part b) is the torque due to neutrino pressure and part c) is the combined torque due to both. The amplitude of the gravity torque (peak-to-peak)

is about 7×10^{-5} dyne-cm. The torque due to neutrino pressure is an order of magnitude smaller at about 7.2×10^{-6} dyne-cm. The signal shape for the neutrino torque is similar but of opposite sign to that of the gravitational torque. The gravity is attractive and the neutrino radiation pressure is repulsive. Both forces act primarily on the sapphire crystal which is heavier than the electrostatic plates and closer to the source on the wheel. The gravity also acts on the other masses whereas the neutrino force is modelled as acting only on the crystal. For this reason, the pulse shapes are not exactly the same although they appear reasonably similar. The effect of the gravity force is more difficult to understand intuitively because it is the net effect of the torques applied to 4 masses. The torque on the crystal is easier to understand intuitively since only the crystal is involved. In Figure 3c where both gravitational and neutrino torques are added together, the net effect is a slight cancellation of the signals leaving a net amplitude of 6.2×10^{-5} dyne-cm.

In Figure 4 the torsion balance has been rotated 90° clockwise to the orientation shown in Figure 2b. Now the closest mass to the table is one of the electrostatic plates. Figure 4a shows the gravity signal. The sign of the curve is opposite to that in Figure 3a and the amplitude is a little less at 5×10^{-5} dyne-cm. Figure 4b shows the neutrino torque. The signal does not reverse sign as in Figure 3b. From Figure 2b we see that the torque from the radiation pressure is always in the same direction because the radiation pressure is never from the other side of the crystal as in the case in Figure 2a. The amplitude of the neutrino signal is

4.7×10^{-6} dyne-cm which is less than in Figure 3b. For both Figures 3 and 4 the neutrino signal is about an order of magnitude less than the gravity signal. Figure 4c shows the combined signal. The amplitude is slightly less than with the gravity done.

Figure 5 shows the response of the torsion balance to the torque shown in Figure 3. The damping is 6% of critical damping (the value computed from observing the rate of decay of oscillations of the torsion balance). The behavior in Figure 5 is dominated by oscillations at the natural frequency of the torsion balance. The actual pulse shape does not resemble the driving torque. Parts a), b), and c) of the figure are for gravity, neutrino, and gravity plus neutrino respectively. The maximum amplitudes are 6.7×10^{-8} , 6.6×10^{-9} , and 5.9×10^{-8} radians respectively. The points where the amplitudes are computed are indicated by the bars. The maximum amplitudes are roughly proportional to the driving torques.

Figure 6 shows the response of the torsion balance to the torques shown in Figure 4 with the torsion balance oriented at 90° and 6% of critical damping. The amplitudes for G(gravity), N(neutrino), and G+N (gravity plus neutrino) are 4.9×10^{-8} , 5.0×10^{-9} , and 4.6×10^{-8} radians respectively. The responses are roughly proportional to the driving torques with the pulse shape dominated by the natural oscillations of the torsion balance.

Figure 7 shows the response of the torsion balance for the torques of Figures 3a and 3c with 50% of critical damping. The pulse shape is closer to that of the driving torque. The amplitudes are 2.9×10^{-8} and 2.5×10^{-8} radians for G and $G + N$ respectively. The amplitudes is less than half that of Figures 5a and 5c with 6% of critical damping. The low damping results in larger swings of the torsion balance but the input pulse shape is not reproduced.

Figure 8 is the response for the torques of Figure 4a and 4c with 50% of critical damping. The amplitudes are 2.2×10^{-8} and 2.1×10^{-8} radians which is less than half of the amplitudes for Figures 6a and 6c with 6% damping.

Figure 9 shows the response for the torques of Figure 3 with critical damping. The amplitudes are reduced still further (in comparison to the 50% and 6% damping cases) but the input pulse shape is much more accurately reproduced. The amplitudes for G , N , and $G + N$, are 1.8×10^{-8} , 1.9×10^{-9} , and 1.65×10^{-8} radians respectively.

Figure 10 shows the response to the torques of Figure 4 with critical damping. The pulse shapes are well reproduced. The amplitudes for G , N , and $G + N$ are 1.4×10^{-8} , 1.6×10^{-9} , and 1.35×10^{-8} radians respectively.

In the simulations described so far, the neutrino signal is measured by taking the difference between the response with $G + N$ and just G alone. Since N is an order of magnitude smaller than G , the experiment depends on taking the

difference between two large numbers. In the remaining simulations, there are 30 balls equally spaced around the rim of the wheel. For the $G + N$ case one of the balls is filled with tritium and the others are filled with an equal mass of deuterium.

Figure 11 shows the torque produced by 30 balls with and without a tritium source. In part a) the gravity signal produces a torque with an amplitude of 5.7×10^{-8} dyne-cm peak-to-peak. Comparing this with Figure 3a showing the gravity signal for one ball we see that the amplitude is reduced by a factor of about 1200 by adding dummy balls of equal mass. Figure 11b shows the signal with 30 balls, one of which has a tritium source. The amplitude is 7×10^{-6} dyne-cm, the same as Figure 3b for only the neutrino source. In Figure 11 the $G + N$ signal is two orders of magnitude greater than for G alone. A small ripple is visible on Figure 11b.

Figure 12 is for 30 balls with the detector oriented at 90° . For G alone the amplitude is 2.65×10^{-9} dyne-cm. Comparing this with the signal in Figure 4a for one ball which is 5×10^{-5} dynes, there is a reduction of about a factor of about 19000 in amplitude. The difference between this result and that for 180° as shown in Figure 11a is probably due to the increased distance of the heavier masses on the torsion balance from the edge of the rotating wheel. Figure 12b shows the torque for $G + N$. The amplitude is 4.8×10^{-6} dyne-cm, the same as Figure 4b for the neutrino alone. There is no visible ripple from the gravity of the 30 balls.

Figure 13 shows the response of the torsion balance to the torques shown in Figure 11 with critical damping. For G alone, the amplitude is 5×10^{-13} radians, and for $G + N$, it is 1.9×10^{-9} radians, the same as in Figure 9b for N alone. The $G + N$ signal is 3800 times bigger than the G signal. In Figure 11, the $G + N$ torque was only 120 times bigger than the G torque. The reason the response to G in Figure 13a is so small is that the frequency of the ripple is too fast for the detector to respond, so that the detector filters out much of the remaining gravity ripple torque for the 30 balls. No ripple is visible on the $G + N$ response in Figure 13b. The 30 balls produce a non zero average torque and displacement of the torsion balance. The simulations of Figure 13 were begun with an initial displacement of -1.48×10^{-8} radians so that the system is nearly in equilibrium at $t = 0$. This avoids a large initial transient. There is still a small initial transient visible in Figure 13a, but the scale of the plot is adequate for seeing the steady state ripple.

Figure 14 shows the response for the torques of Figure 12 with critical damping. The ripple with G alone is 2×10^{-14} radians. The amplitude with $G + N$ is 1.6×10^{-9} the same as for Figure 10b with N alone. The initial value of the angle used for these simulations is 1.54194×10^{-8} radians in order to be close to equilibrium and avoid a large initial transient that would obscure the steady state behavior by changing the plot scale. The signal for $G + N$ is 80,000 times as large as the gravity ripple.

The results in Figures 11 to 14 assume that all 30 balls have exactly the same mass. In order to see the effect of manufacturing errors some runs have been done with random errors in the mass of the balls. A random number generator was used to assign errors in the range 0 to 1 percent to the masses of each of the 30 balls. The actual errors used are shown in Figure 17a for each of the 30 balls. Figure 15 shows the effect of these errors on the torque and detector response with the detector oriented at 90° . Figure 15a is the torque with just the gravity signal G plus gravity errors ΔG . The peak to peak variation in torque between the lines shown is 5×10^{-7} dyne-cm. The gravity torque with one ball from Figure 4a is 5×10^{-5} dyne-cm so that there is an improvement of a factor of 100 with 30 balls having errors between 0 and 1 percent. Figure 15b shows the response of the detector with critical damping. The peak to peak amplitude between the lines shown is 1.2×10^{-10} radians. Since the response with a single mass in Figure 10a is 1.4×10^{-8} radians, there is an improvement of a factor of 115 with the 30 balls and 1% mass errors. Figure 15c shows the response with $G + \Delta G + N$ and 6% damping. The amplitude of the response between the lines shown is 4.7×10^{-9} . The response in Figure 6b with just N was 5×10^{-9} . The two curves look similar but are not exactly the same. Since the neutrino signal is about 10 times as small as the gravity signal of 1 ball, reducing the gravity signal by a factor of 100 should leave about a 10% error in the neutrino signal.

Figure 16 shows the torque and detector response with 1% errors and the detector oriented at 180° . The torque in Figure 16a with $G + \Delta G$ has an

amplitude of 7.8×10^{-7} dyne-cm between the lines shown. This is 90 times smaller than the torque for 1 ball in Figure 3a. Figure 16b is the response of the detector with critical damping. The amplitude of 1.55×10^{-10} radians is a factor of 115 smaller than the response of 1.8×10^{-8} radians in Figure 9a. Figure 16c shows the response with N added and 6% damping. The amplitude of 6.3×10^{-9} radians between the lines shown is close to the amplitude of 6.6×10^{-9} radians for N alone in Figure 5b. As in the 90° case the mass errors should have an effect equal to about 10% of the neutrino signal.

Errors of 1% in the mass of a ball can be measured to a high degree of precision. Without attempting to remachine the balls, the information on the errors could be used to minimize their effect by pairing light and heavy balls to even out the effect. An example of such a redistribution of errors is shown in Figure 17b. Some runs have been done with these redistributed errors $\Delta G'$.

Figure 18a shows the torque with the redistributed errors and the detector oriented at 90° . The amplitude between the lines shown is 9.5×10^{-8} dyne-cm. This is a factor of 5 smaller than the torque of 5×10^{-7} dyne-cm in Figure 15a, and a factor of 500 smaller than the torque of 5×10^{-5} dyne-cm for 1 ball in Figure 4a. The response of the detector in Figure 18b is 3.5×10^{-11} radians between the lines shown with critical damping. This is a factor of 3.4 smaller than in Figure 15b with random errors and a factor of 400 smaller than the response of 1.4×10^{-8} radians in Figure 10a with 1 ball.

Figure 19 shows the response and torque with redistributed errors and the torsion with balance oriented at 180° . In Figure 19a the amplitude of 2.3×10^{-7} dyne-cm between the lines shown is a factor of 3.4 smaller than the torque of 7.8×10^{-7} dyne-cm in Figure 16a with random errors, and a factor of 300 smaller than the torque of 7×10^{-5} dyne cm for a single ball in Figure 3a. The response of 4×10^{-11} radians in Figure 19b with critical damping is a factor of 3.9 smaller than the response of 1.55×10^{-10} radians in Figure 16b with random errors, and a factor of 450 smaller than the response of 1.8×10^{-8} radians in Figure 9a with one ball.

Table 3. Summary of the peak-to-peak amplitudes of the graphs in Figures 3-14

Fig.	G	N	G+N	UNITS	b/b _c	θ	# Balls
3	7×10^{-5}	7.0×10^{-6}	6.2×10^{-5}	dyne-cm	-	180	1
4	5×10^{-5}	4.7×10^{-6}	4.8×10^{-5}	dyne-cm	-	90	1
5	6.7×10^{-8}	6.6×10^{-9}	5.9×10^{-8}	radians	.06	180	1
6	4.9×10^{-8}	5.0×10^{-9}	4.6×10^{-8}	radians	.06	90	1
7	2.9×10^{-8}	-	2.5×10^{-8}	radians	.50	180	1
8	2.2×10^{-8}	-	2.1×10^{-8}	radians	.50	90	1
9	1.8×10^{-8}	1.9×10^{-9}	1.65×10^{-8}	radians	1.00	180	1
10	1.4×10^{-8}	1.6×10^{-9}	1.35×10^{-8}	radians	1.00	90	1
11	5.7×10^{-8}	-	7.0×10^{-6}	dyne-cm	-	180	30
12	2.65×10^{-9}	-	4.8×10^{-6}	dyne-cm	-	90	30
13	5×10^{-13}	-	1.9×10^{-9}	radians	1.00	180	30
14	2×10^{-14}	-	1.6×10^{-9}	radians	1.00	90	30

In Table 3, the first column is the figure number, the second is the amplitude with only gravity, the third is for neutrino only, the fourth column is

gravity plus neutrino, the fifth is the units (torque in dyne-cm, or rotation angle of the torsion balance in radians), the sixth column is the damping ratio (for angle units only), the seventh is the orientation of the torsion balance, and the eighth is the number of balls on the rotating wheel.

Table 4. Peak-to-peak amplitudes with random and redistributed mass errors in the 30 balls

Fig.	$G + \Delta G$ (dyne-cm)	$G + \Delta G$ (radians) ($b/b_c = 1.00$)	$G + \Delta G + N$ (radians) ($b/b_c = .06$)	θ (deg)	Mass Errors
15	5×10^{-7}	1.2×10^{-10}	4.7×10^{-9}	90	random
16	7.8×10^{-7}	1.55×10^{-10}	6.3×10^{-9}	180	random
18	9.5×10^{-8}	3.5×10^{-11}	-	90	redistributed
19	2.3×10^{-7}	4.0×10^{-11}	-	180	redistributed

In Table 4 the first column is the figure number, the second is the amplitude of the torque with 30 balls having mass errors between 0 and 1 percent, the third is the rotation angle of the torsion balance for $G + \Delta G$, the fourth is the rotation angle of the torsion balance with gravity, gravity errors and neutrino radiation pressure, the fifth is the orientation of the torsion balance, and the sixth is the manner of distributing the mass errors.

1.5 Computer Plots and Figures

Figure Captions

- Figure 3. Torque with 1 ball and detector at 180°.
- Figure 4. Torque with 1 ball and detector at 90°.
- Figure 5. Angle vs. time with 1 ball, 6% damping and detector at 180°.
- Figure 6. Angle vs. time with 1 ball, 6% damping and detector at 90°.
- Figure 7. Angle vs. time with 1 ball, 50% damping, and detector at 180°.
- Figure 8. Angle vs. time with 1 ball, 50% damping, and detector at 90°.
- Figure 9. Angle vs. time with 1 ball, 100% of critical damping and detector at 180°.
- Figure 10. Angle vs. time with 1 ball, 100% of critical damping and detector at 90°.
- Figure 11. Torque with 30 balls and detector at 180°.
- Figure 12. Torque with 30 balls and detector at 90°.
- Figure 13. Angle vs. time with 30 balls, 100% of critical damping, and detector at 180°.

- Figure 14. Angle vs. time with 30 balls, 100% of critical damping and detector at 90° .
- Figure 15. Amplitudes with 30 balls, 1% random mass errors and detector at 90° .
- Figure 16. Amplitudes with 30 balls, 1% random mass errors and detector at 180° .
- Figure 17. Mass errors in the 30 balls.
- Figure 18. Amplitudes with 30 balls, 1% redistributed mass errors and detector at 90° .
- Figure 19. Amplitudes with 30 balls, 1% redistributed mass errors and detector at 180° .

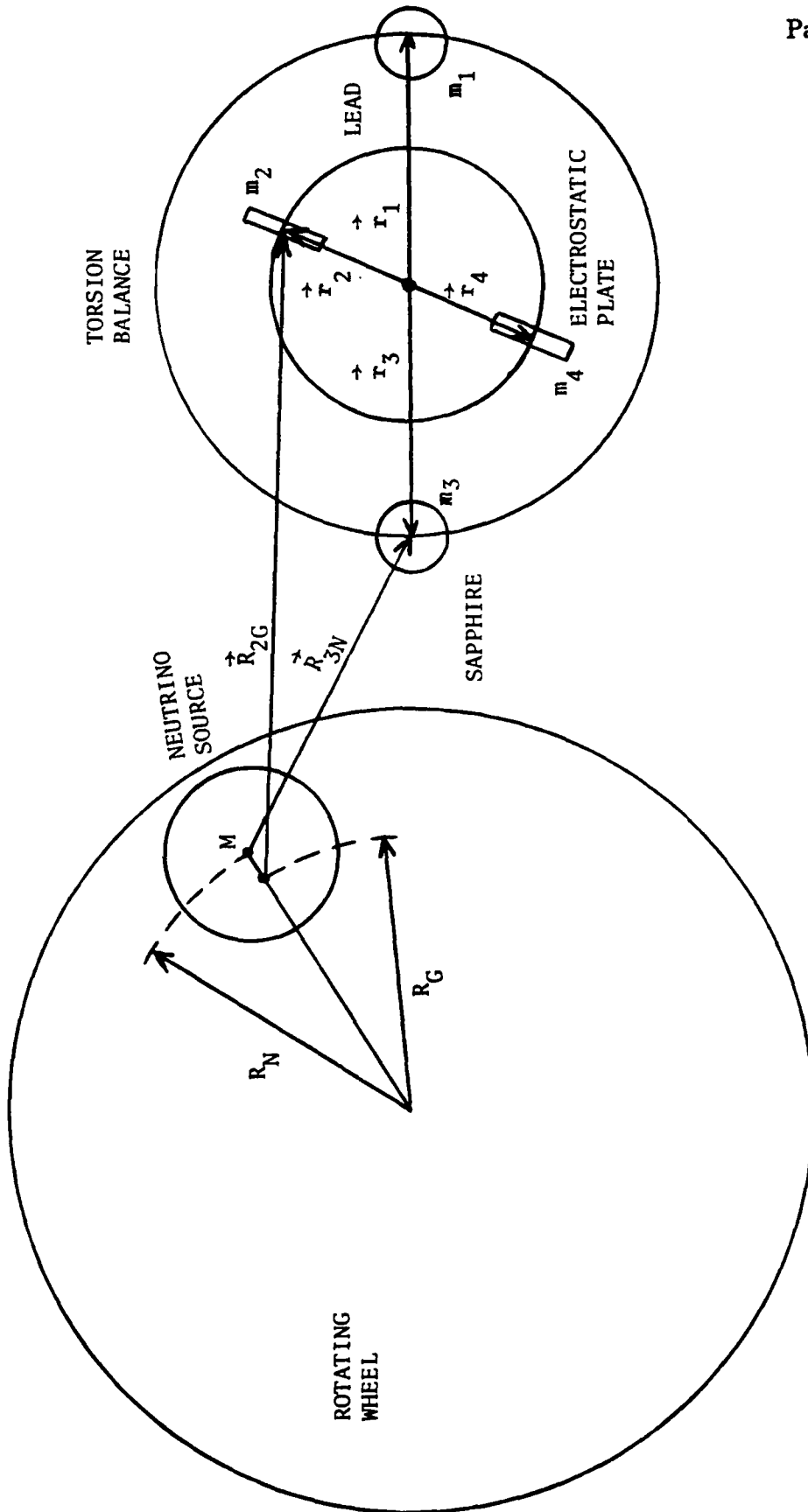


Figure 1. Model used for calculating gravitational and radiation torques on the torsion balance.

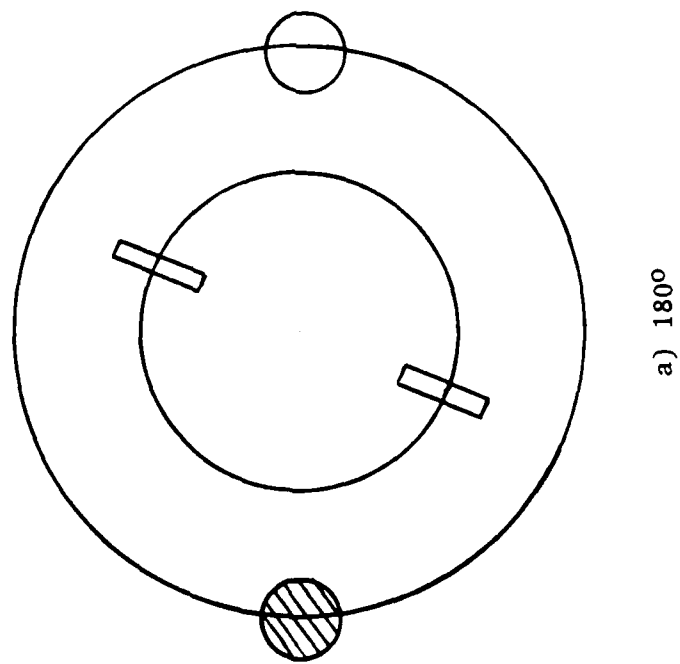
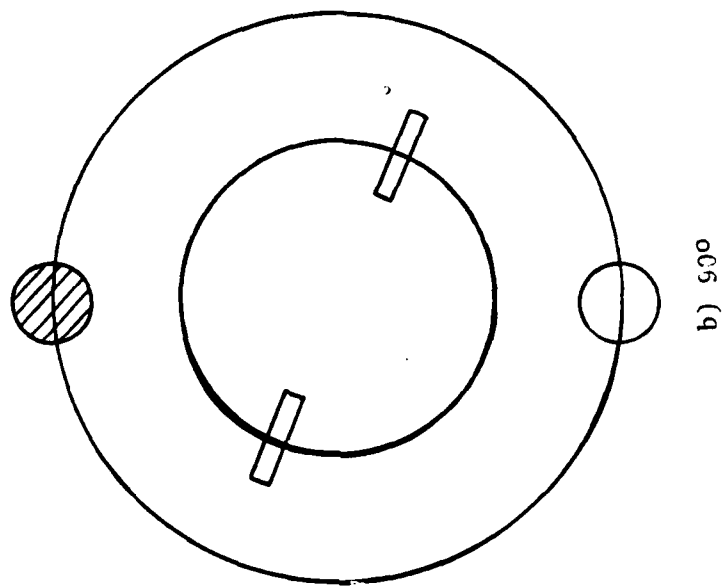


Figure 2. Orientation of the torsion balance used in computer simulations.

Torque (dyne-cm)

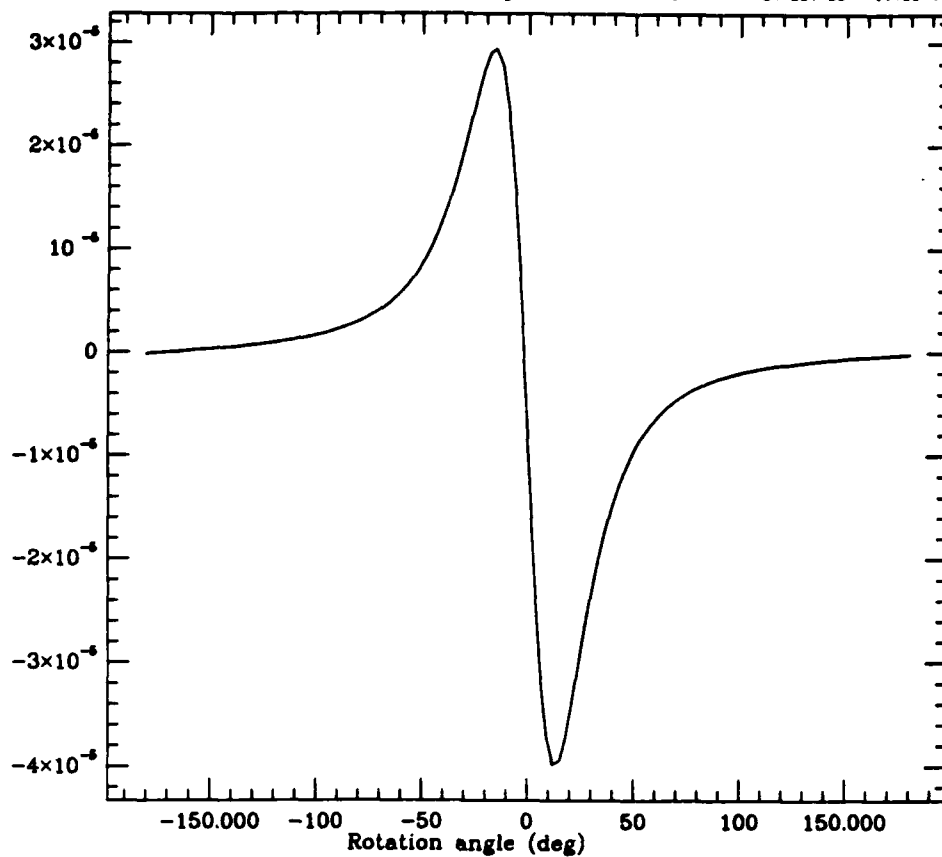


Figure 3(a). G

Torque (dyne-cm)

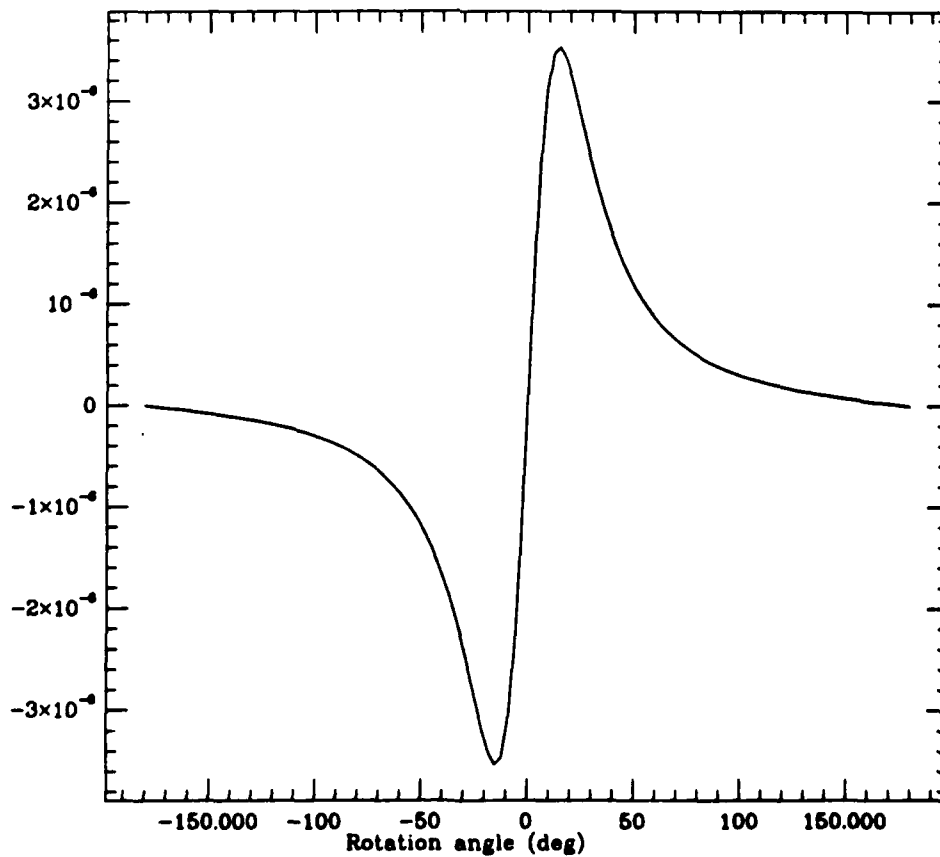


Figure 3(b). N

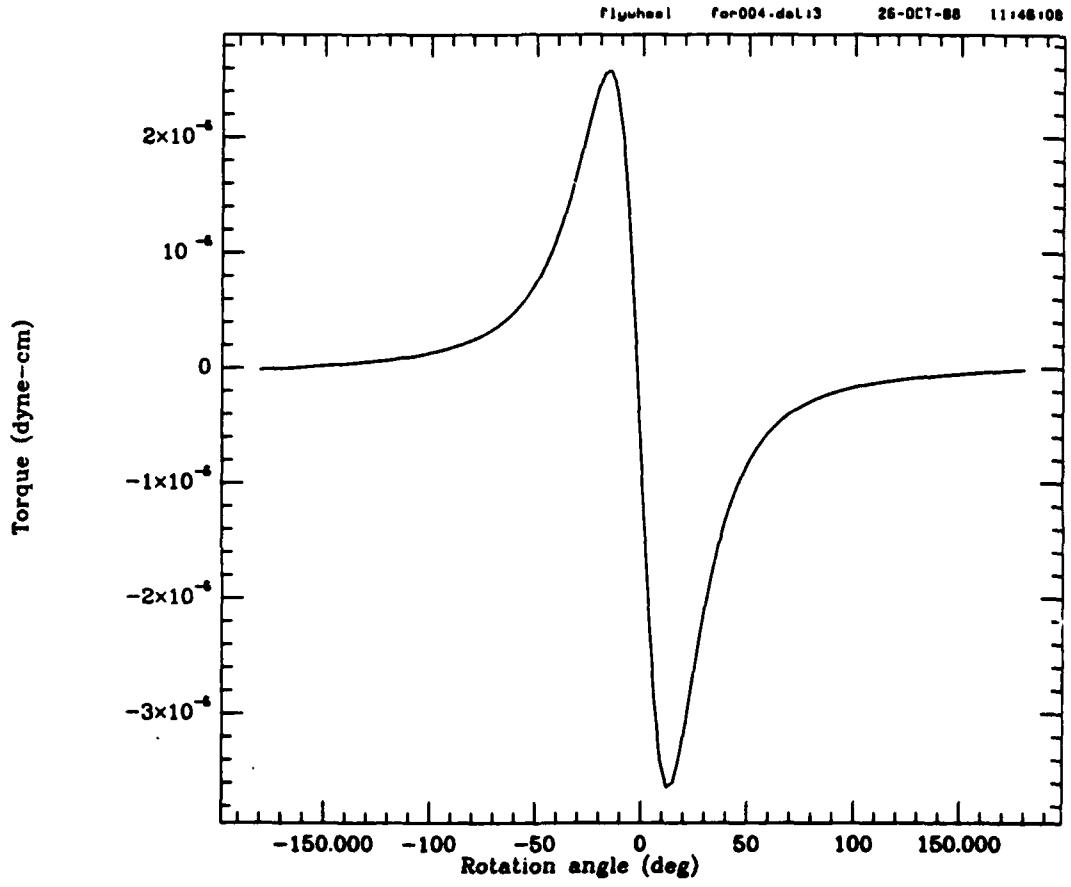


Figure 3(c). G+N

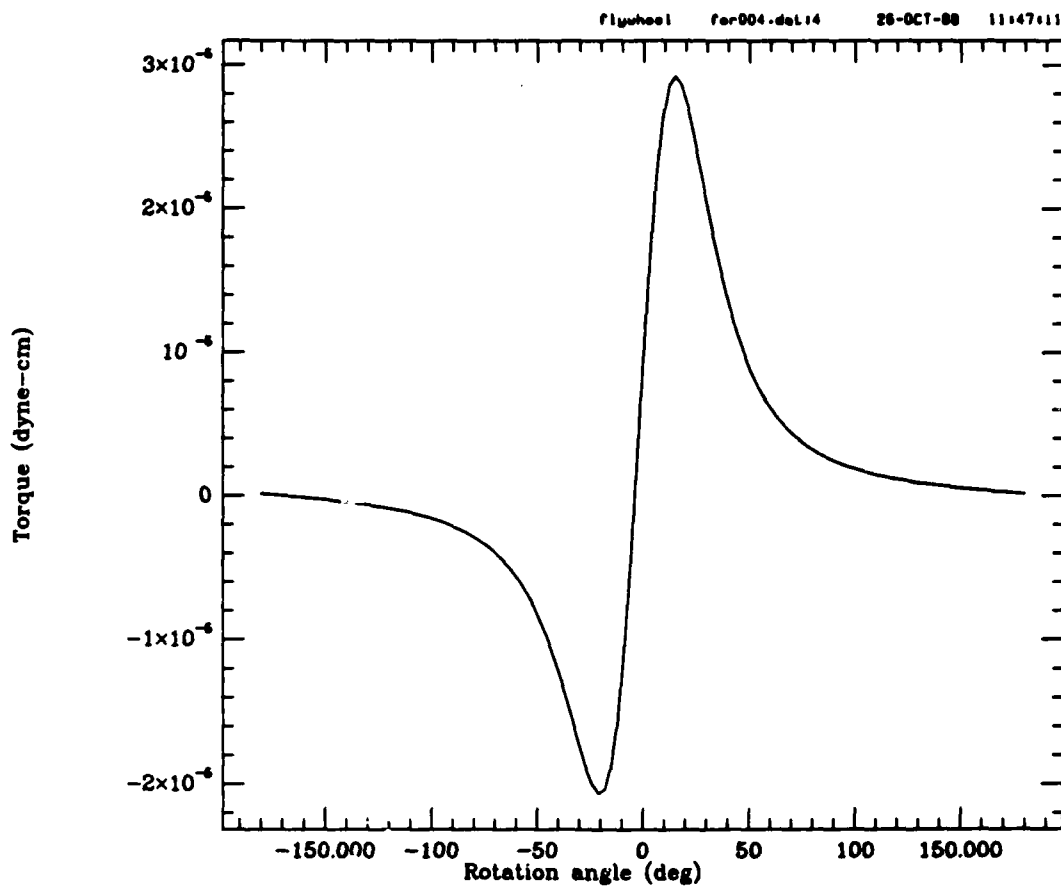


Figure 4(a). G

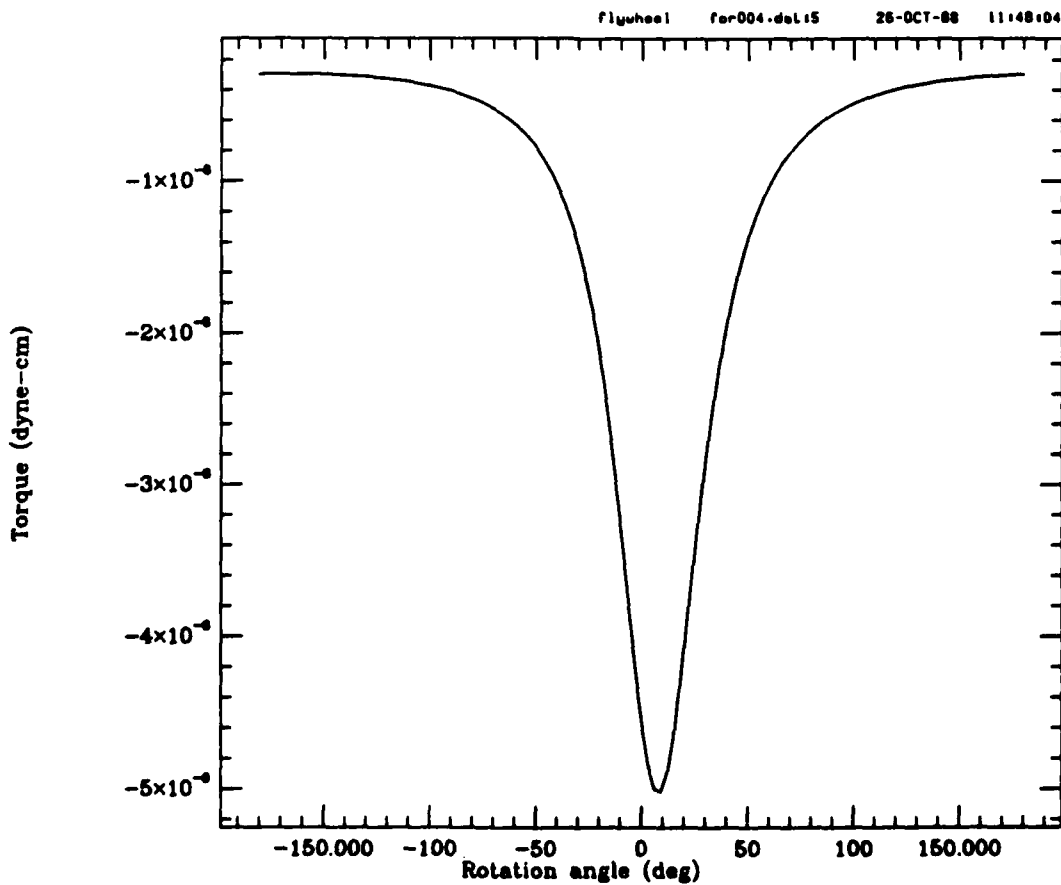


Figure 4(b). N

Figure 4(c) for004.dat:6 26-OCT-88 11:48:43

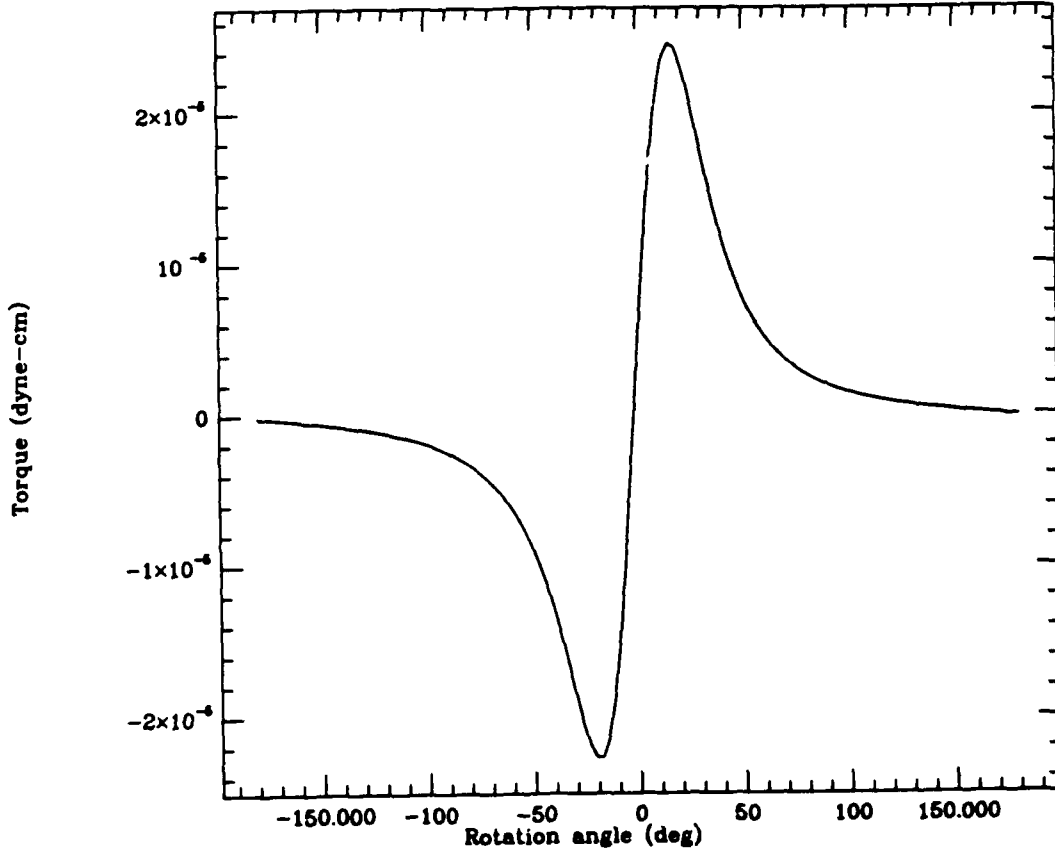


Figure 4(c). G+N

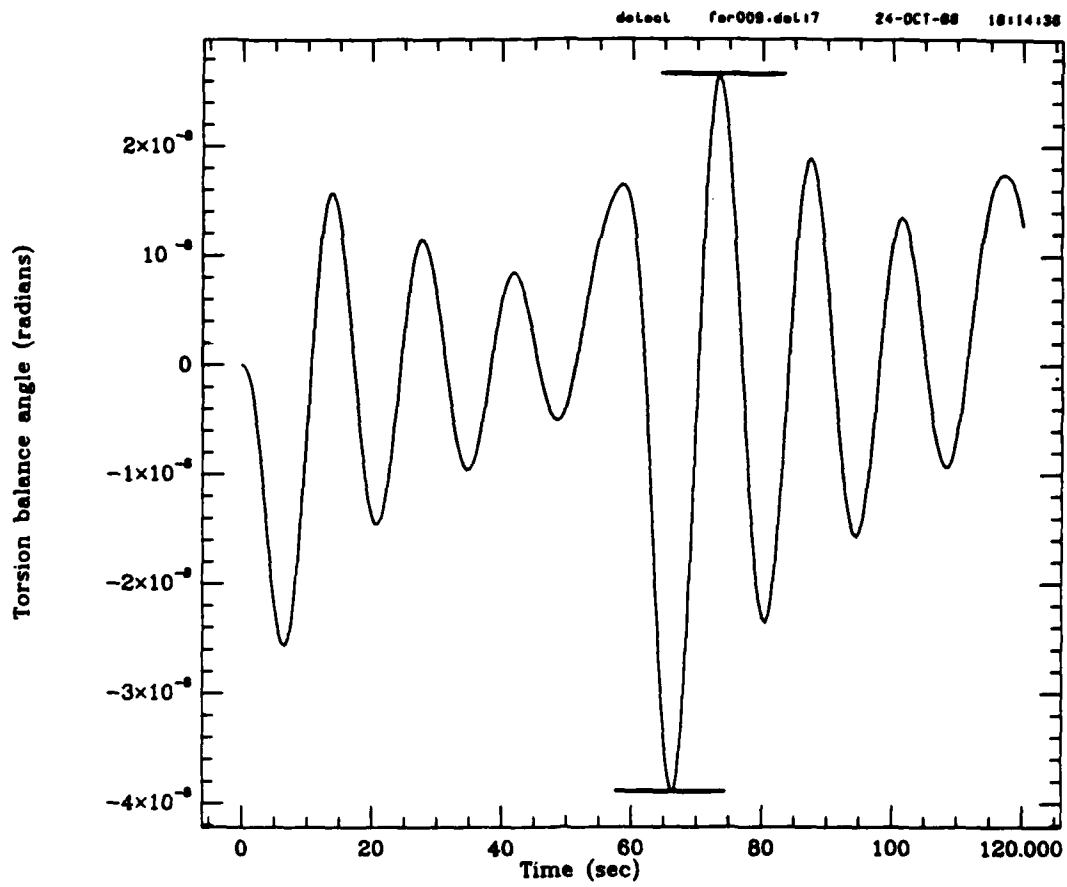


Figure 5(a). G

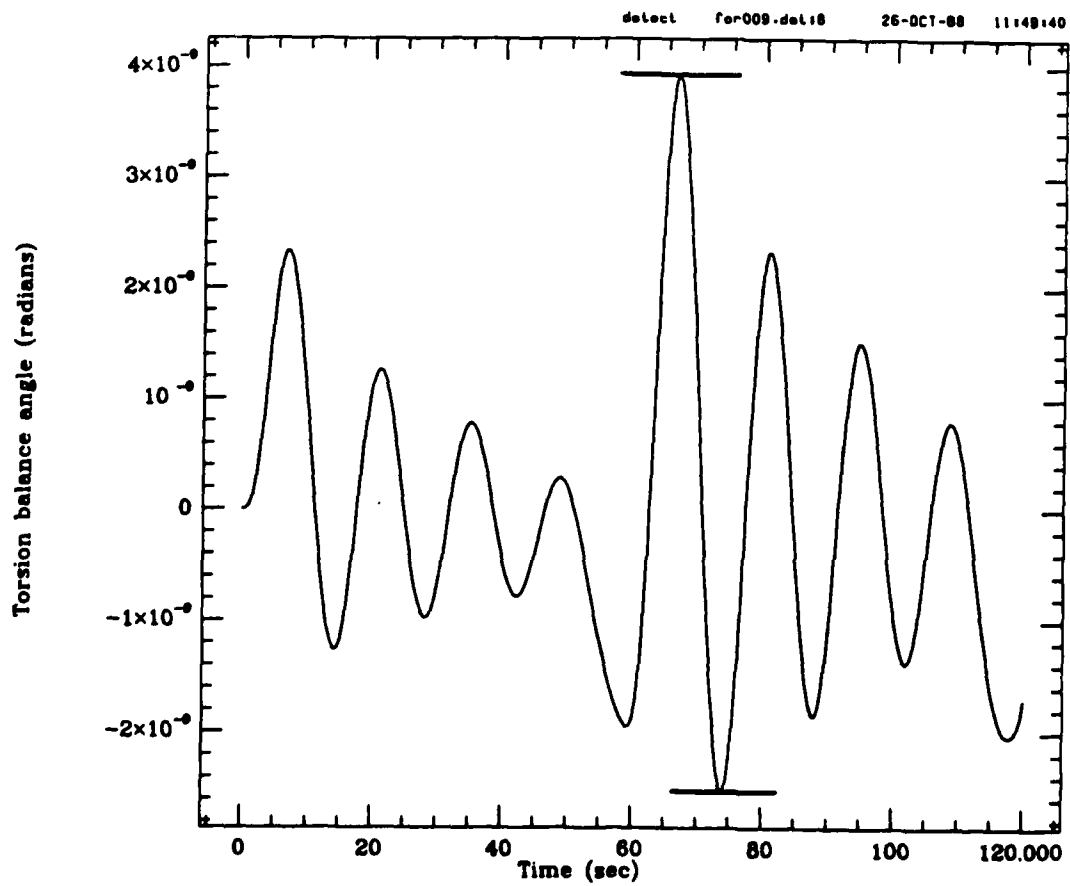


Figure 5(b). N

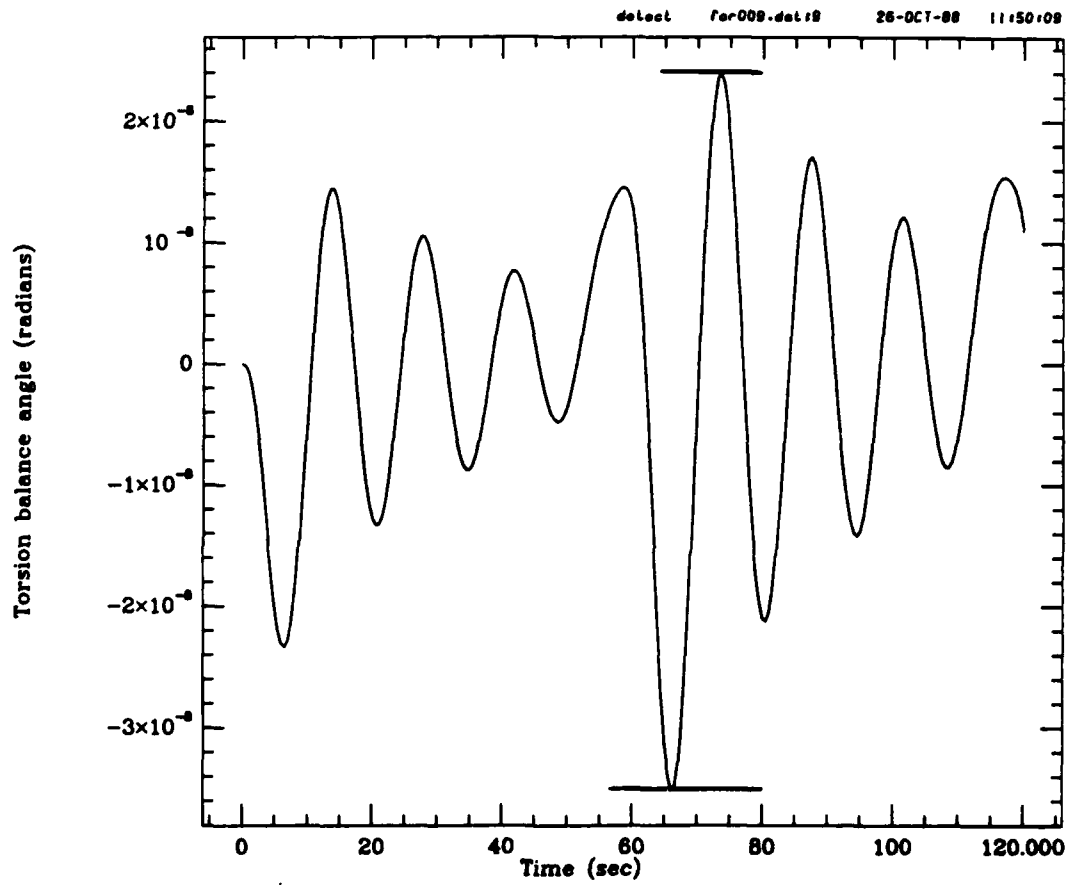


Figure 5(c). G+N

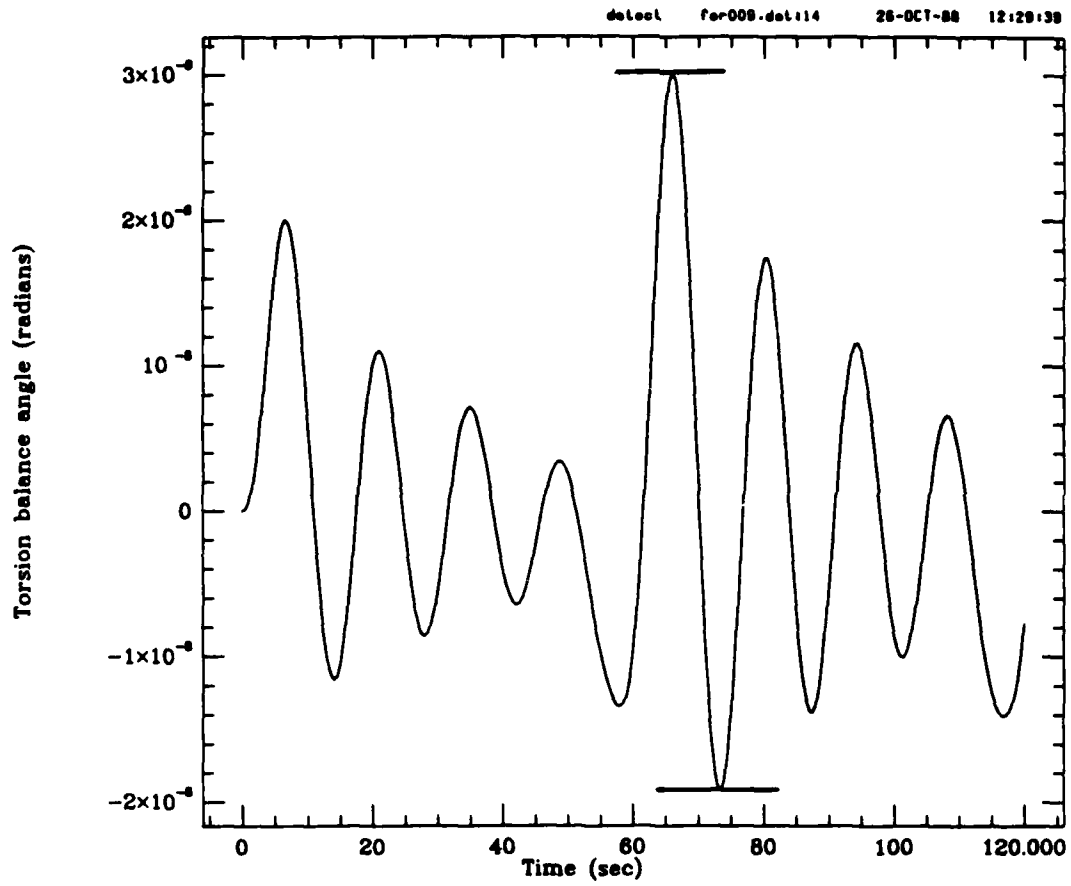


Figure 6(a). G

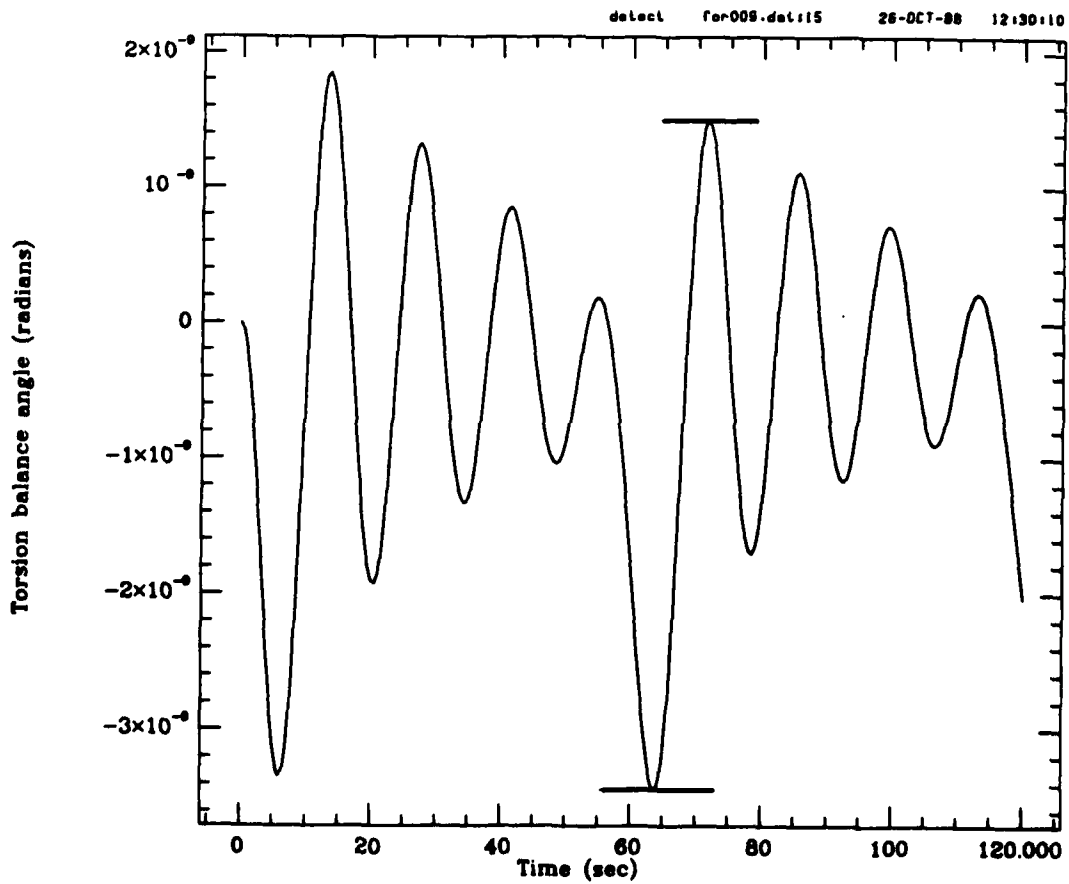


Figure 6(b). N

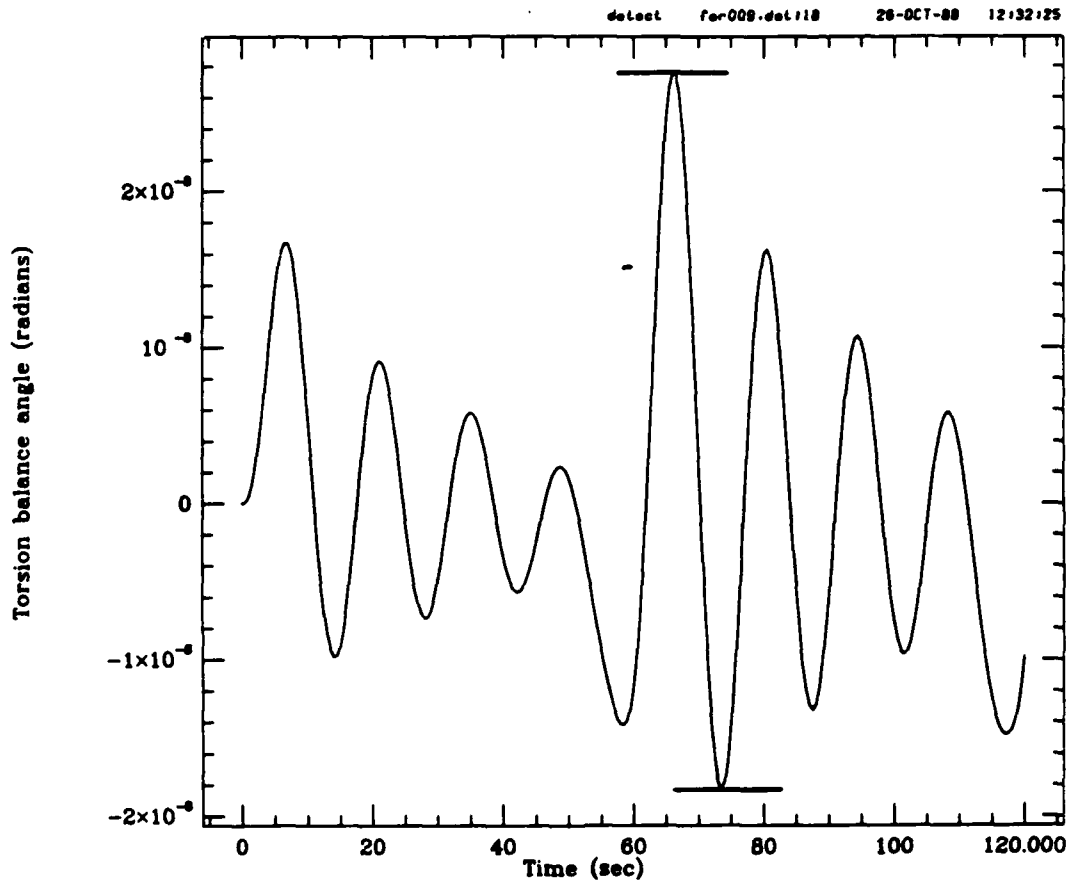


Figure 6(c). G+N

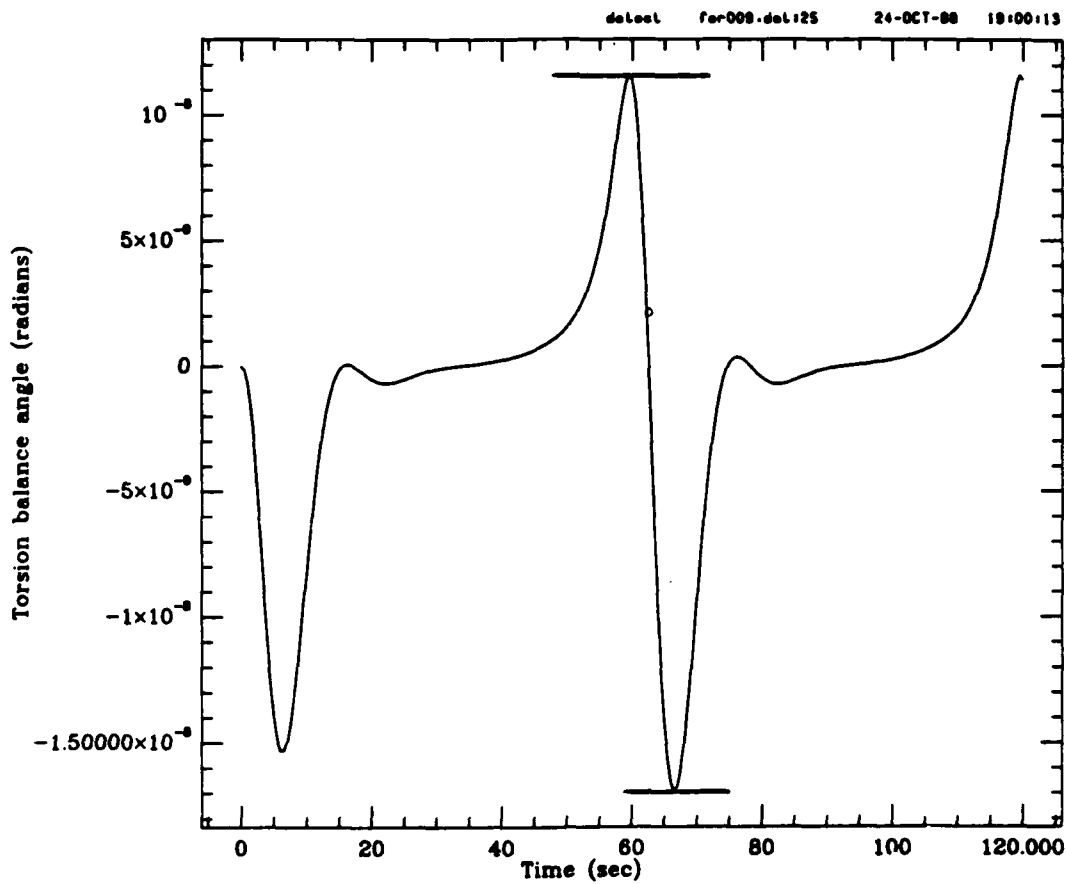


Figure 7(a). G

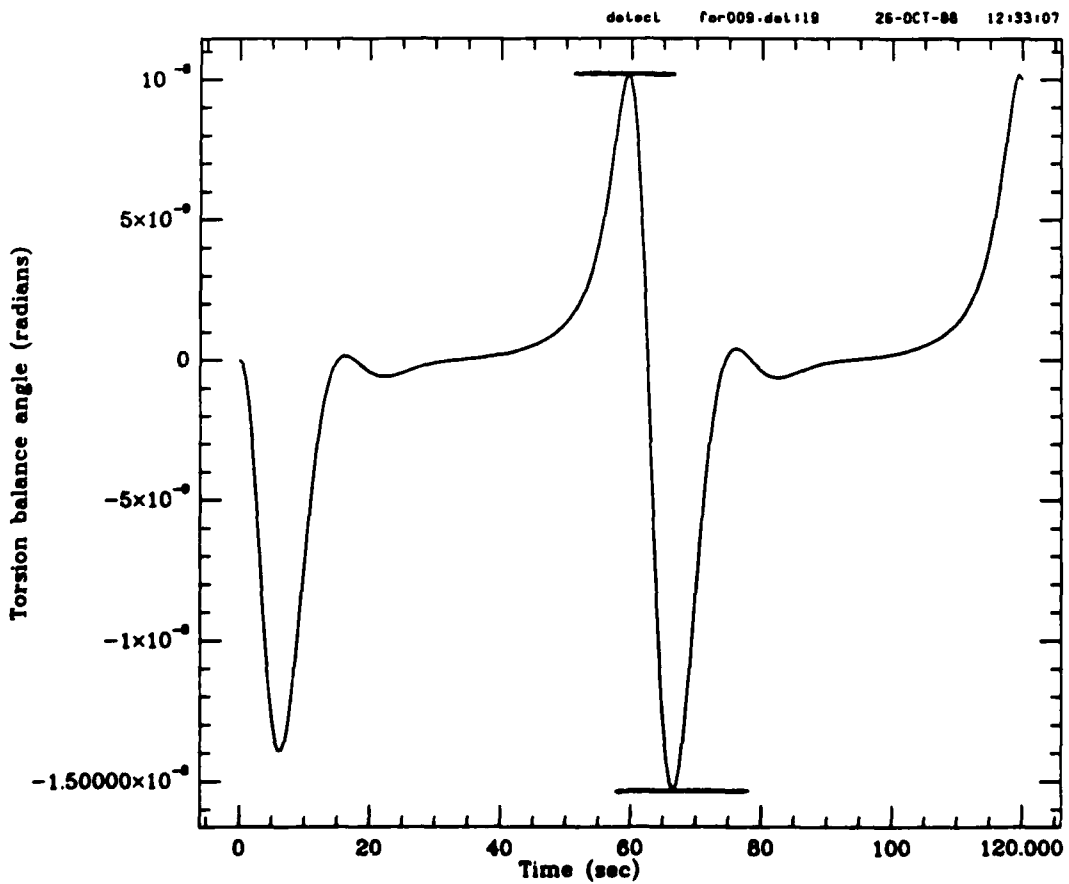


Figure 7(b). G+N

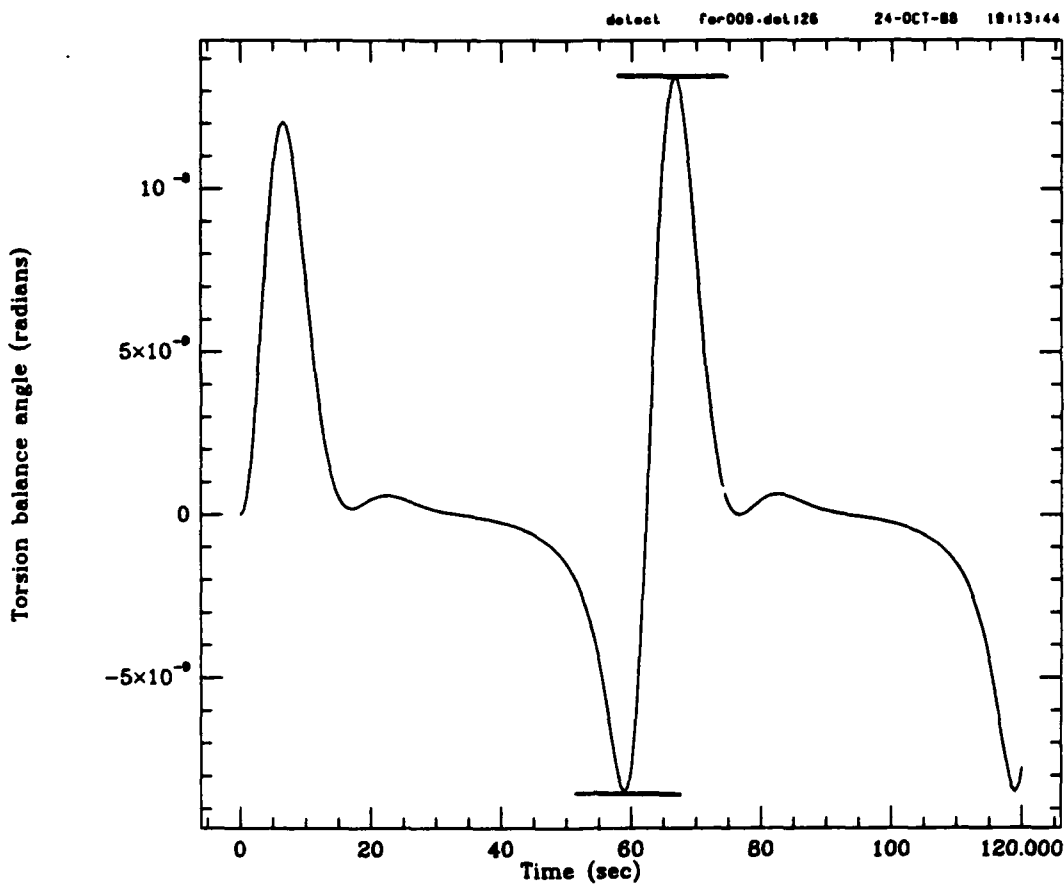


Figure 8(a). G

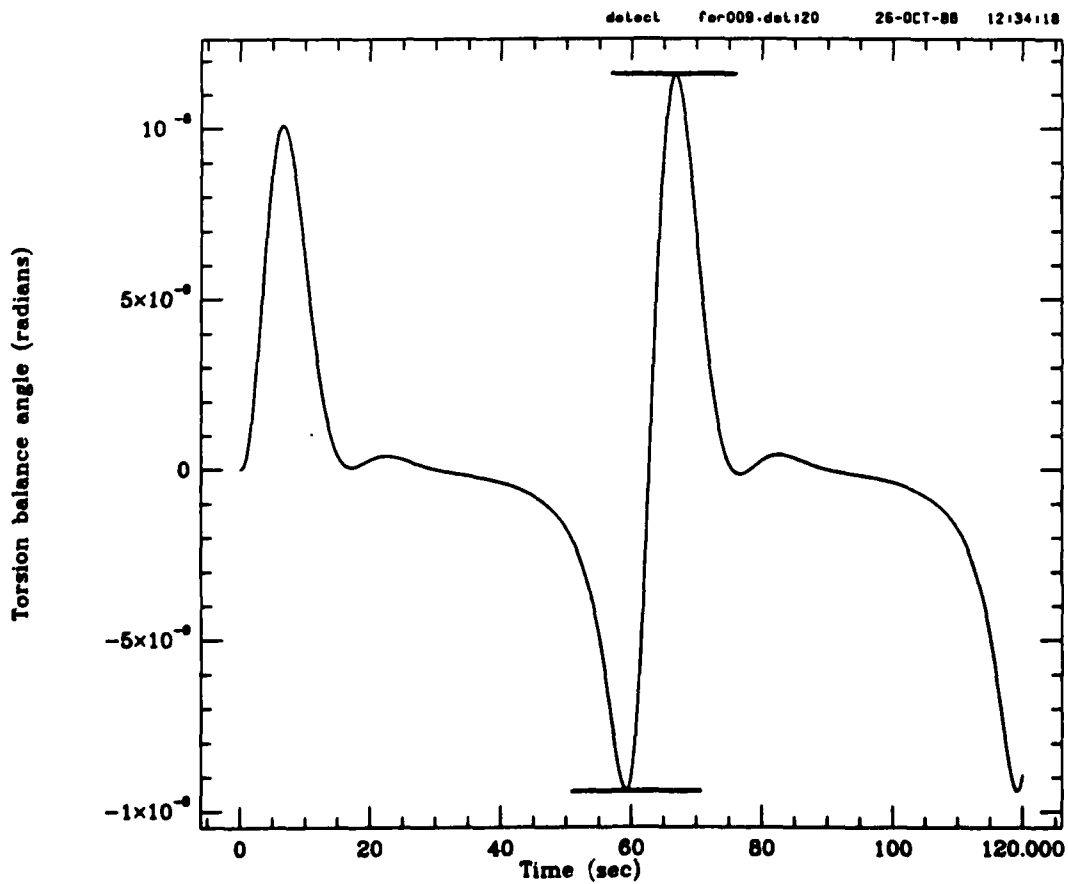


Figure 8(b). G+N

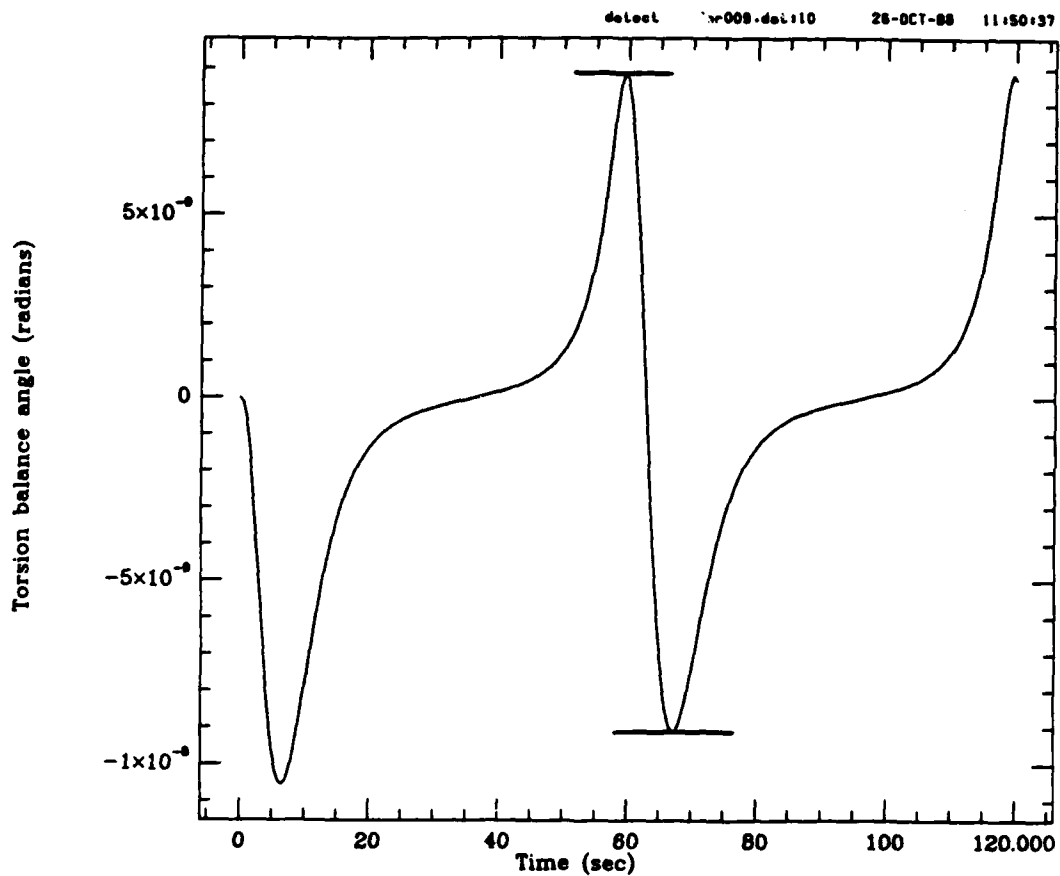


Figure 9(a). G

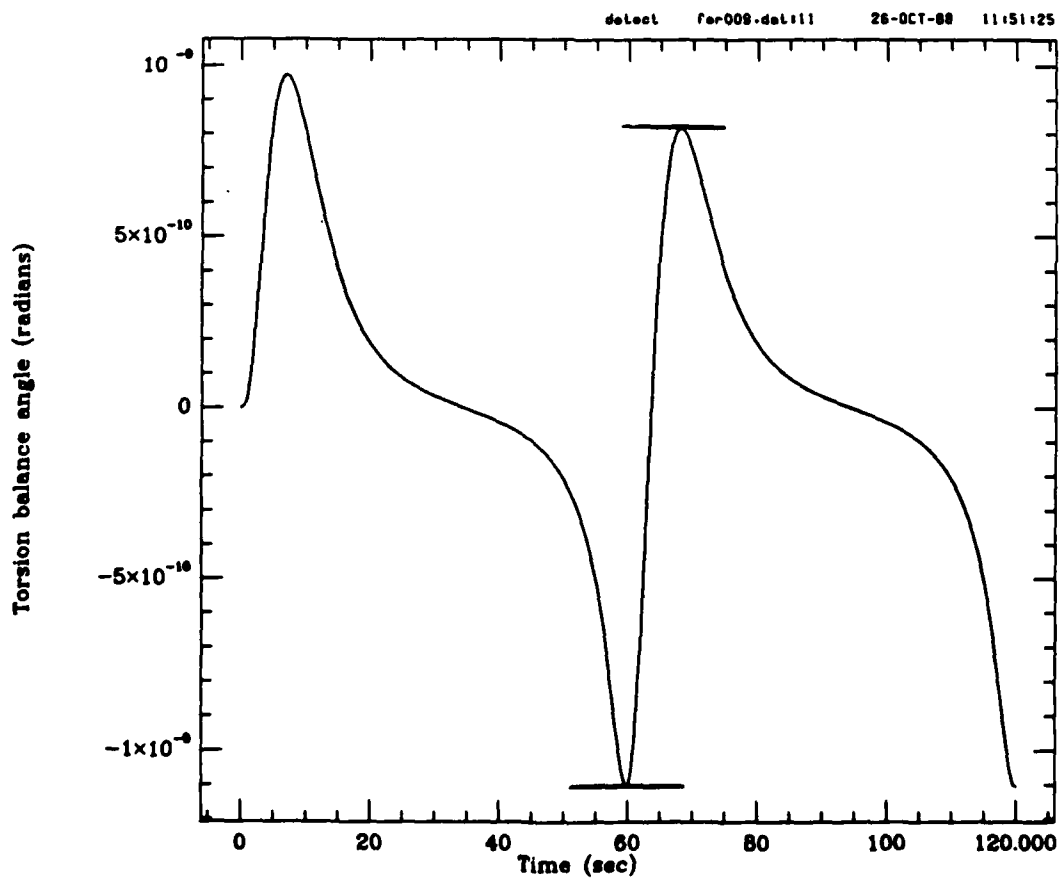


Figure 9(b). N

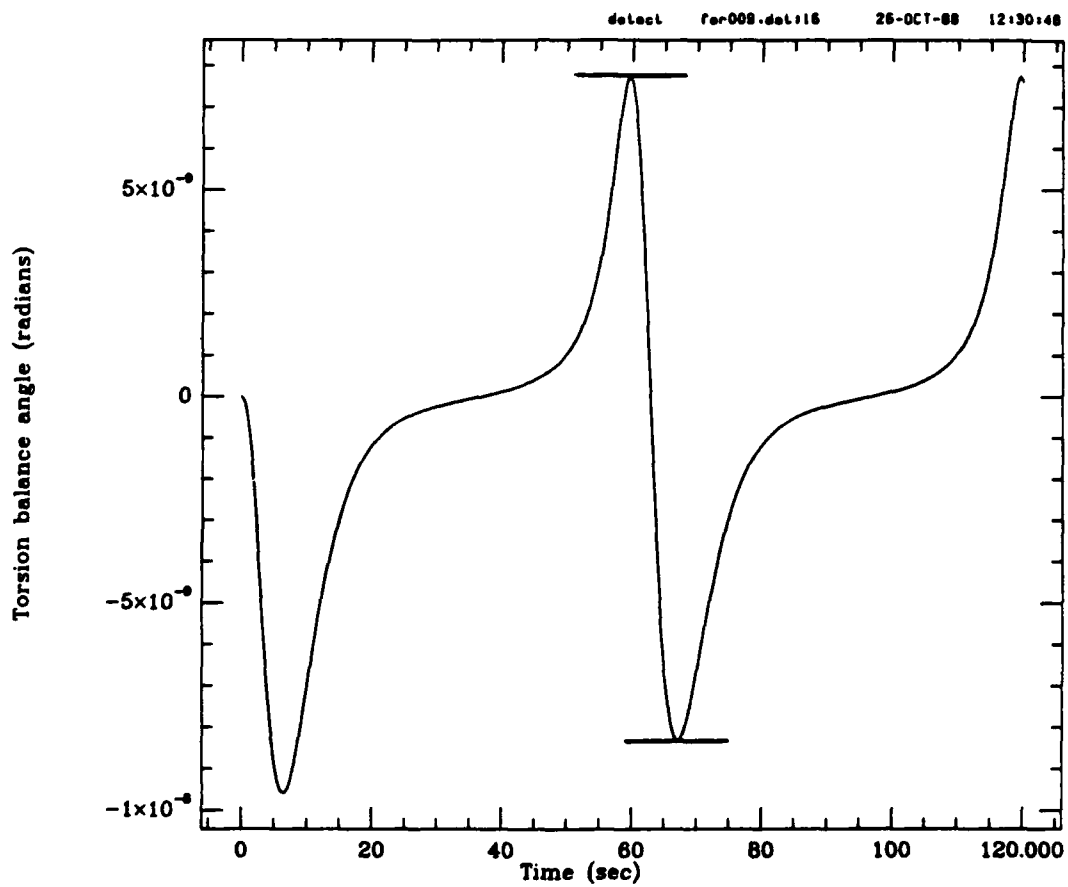


Figure 9(c). G+N

detect for008.dat:112 26-OCT-88 11:51:59

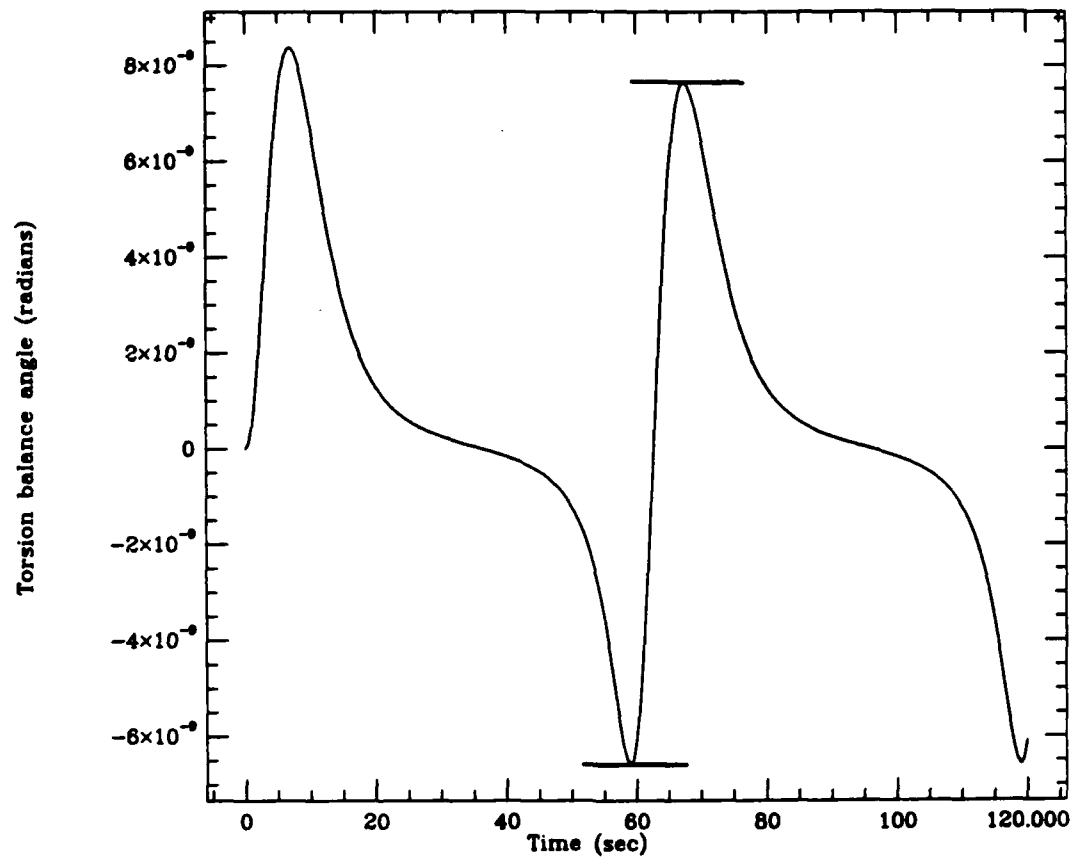


Figure 10(a). G

detect for008.dat:113 26-OCT-88 12:24:11

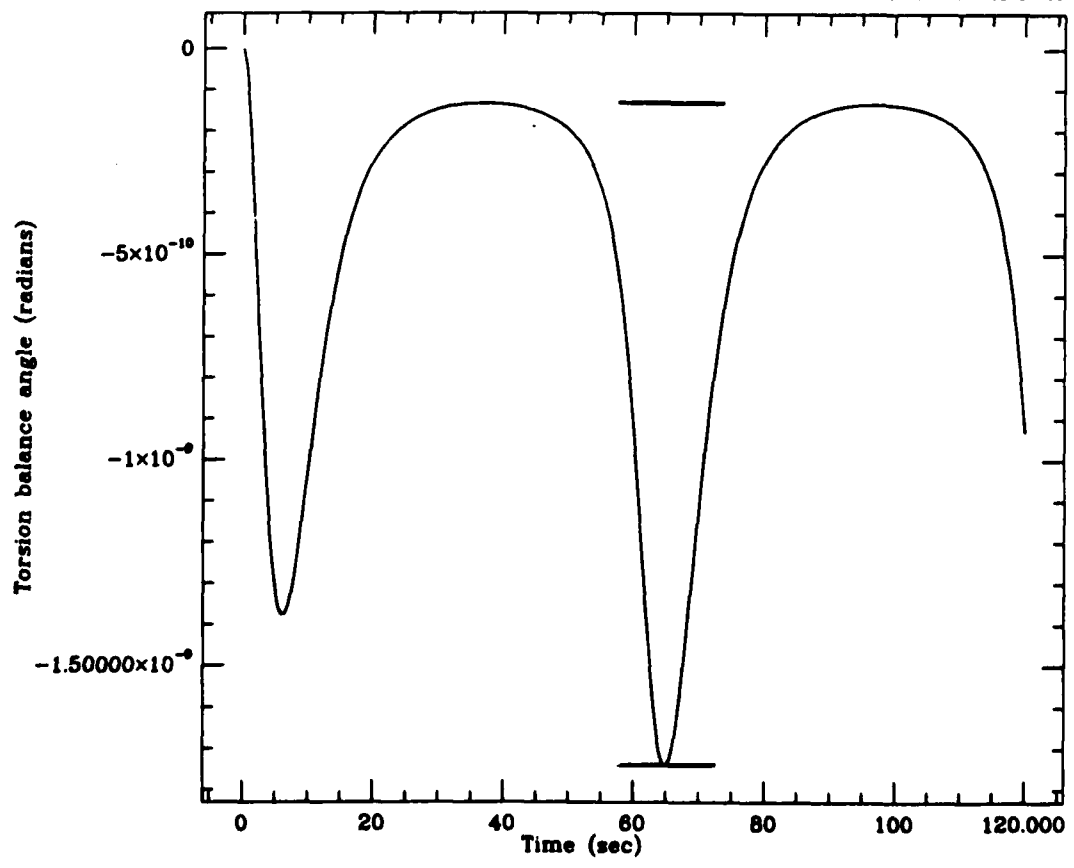


Figure 10(b). N

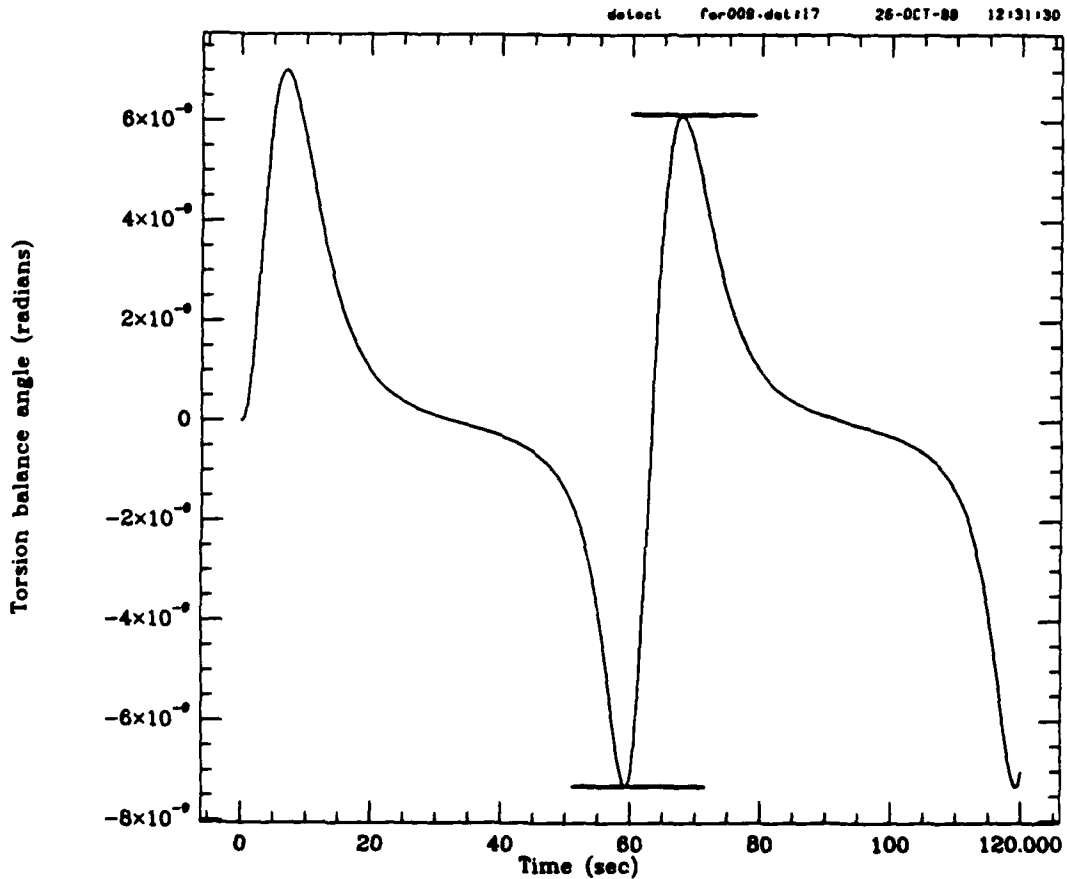


Figure 10(c). G+N

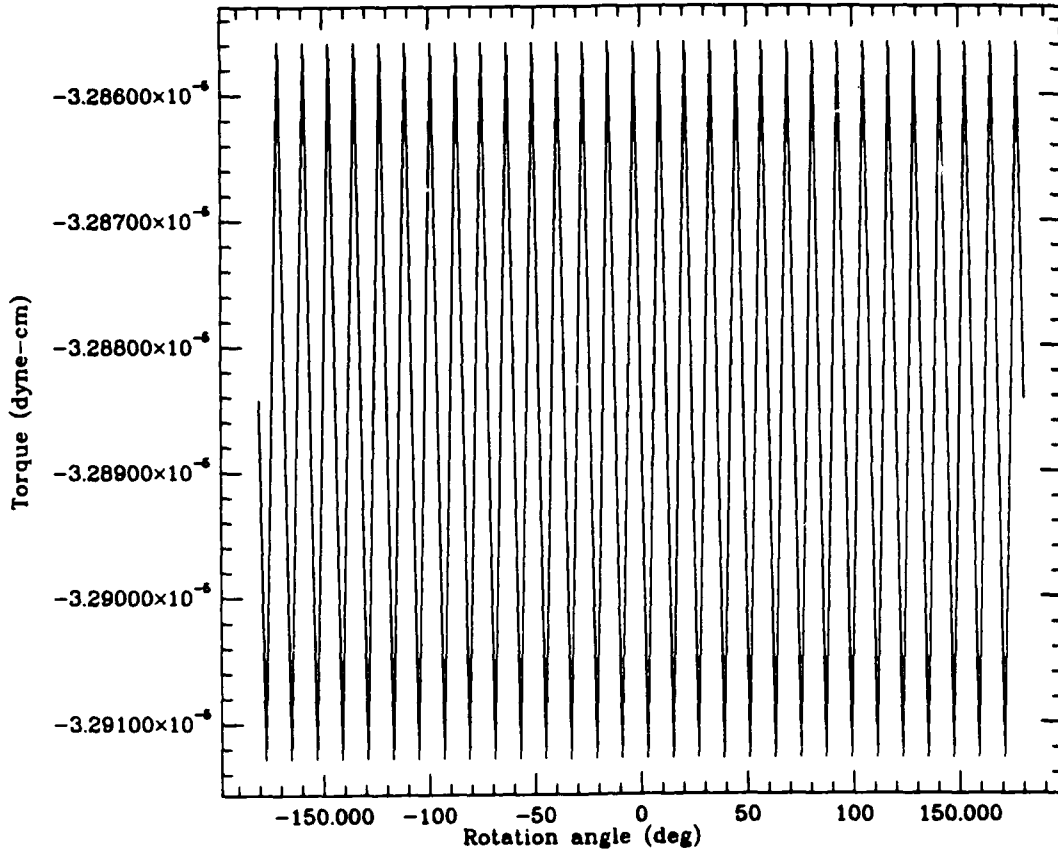


Figure 11(a). G

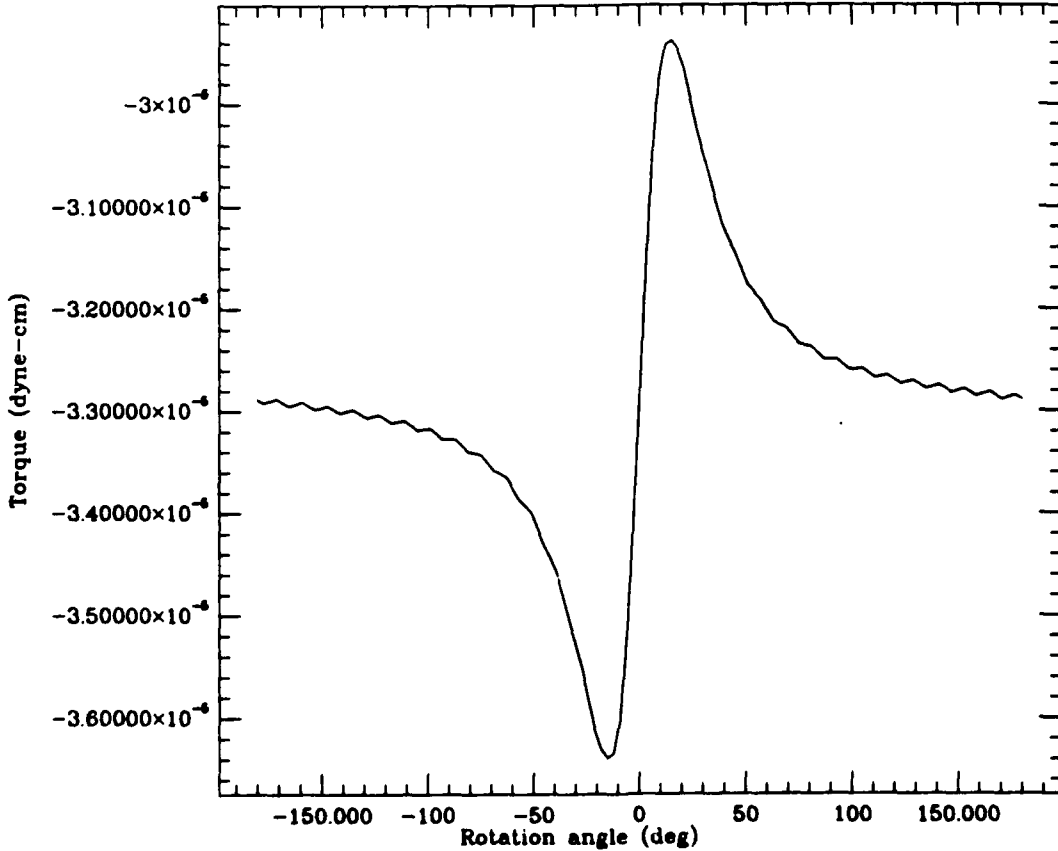


Figure 11(b). G+N

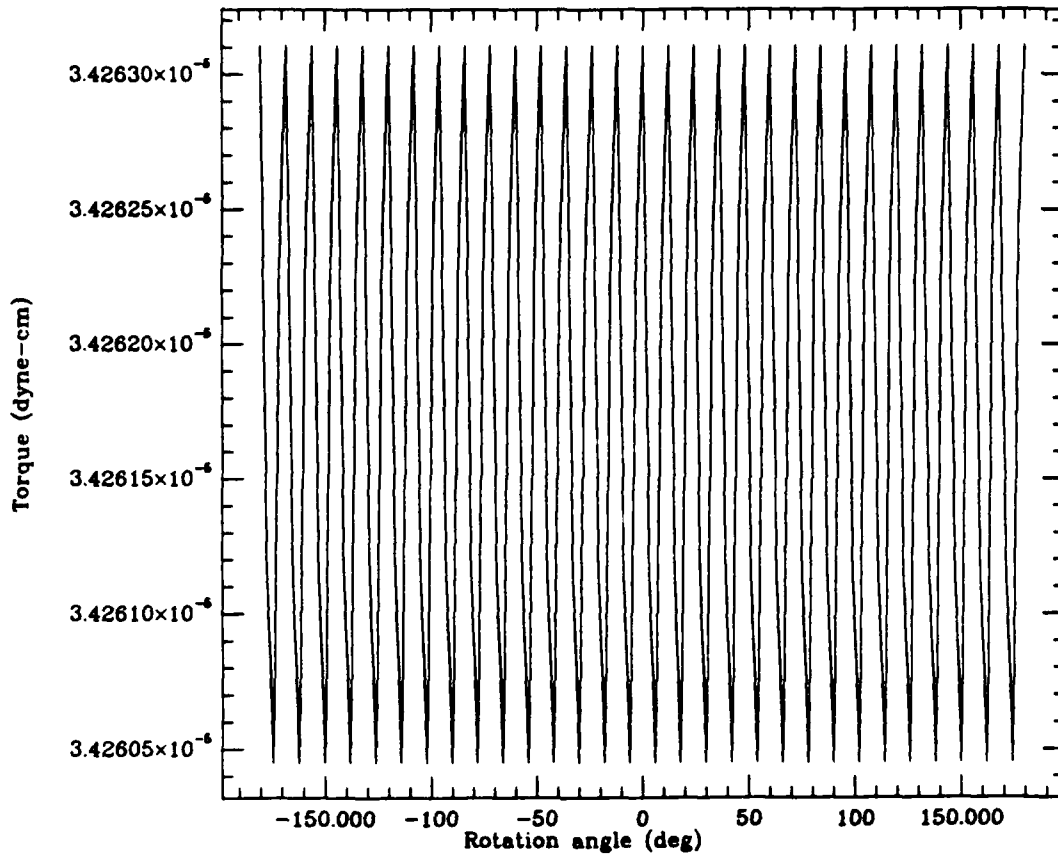


Figure 12(a). G

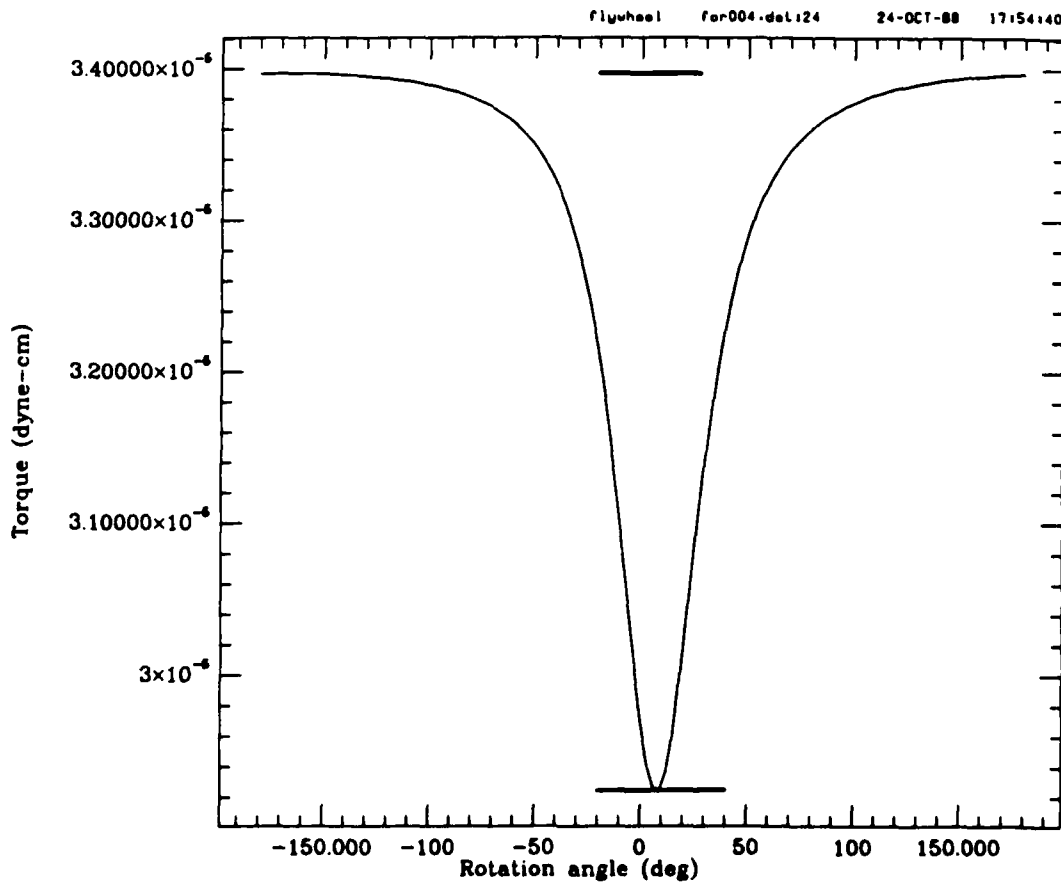


Figure 12(b). G+N

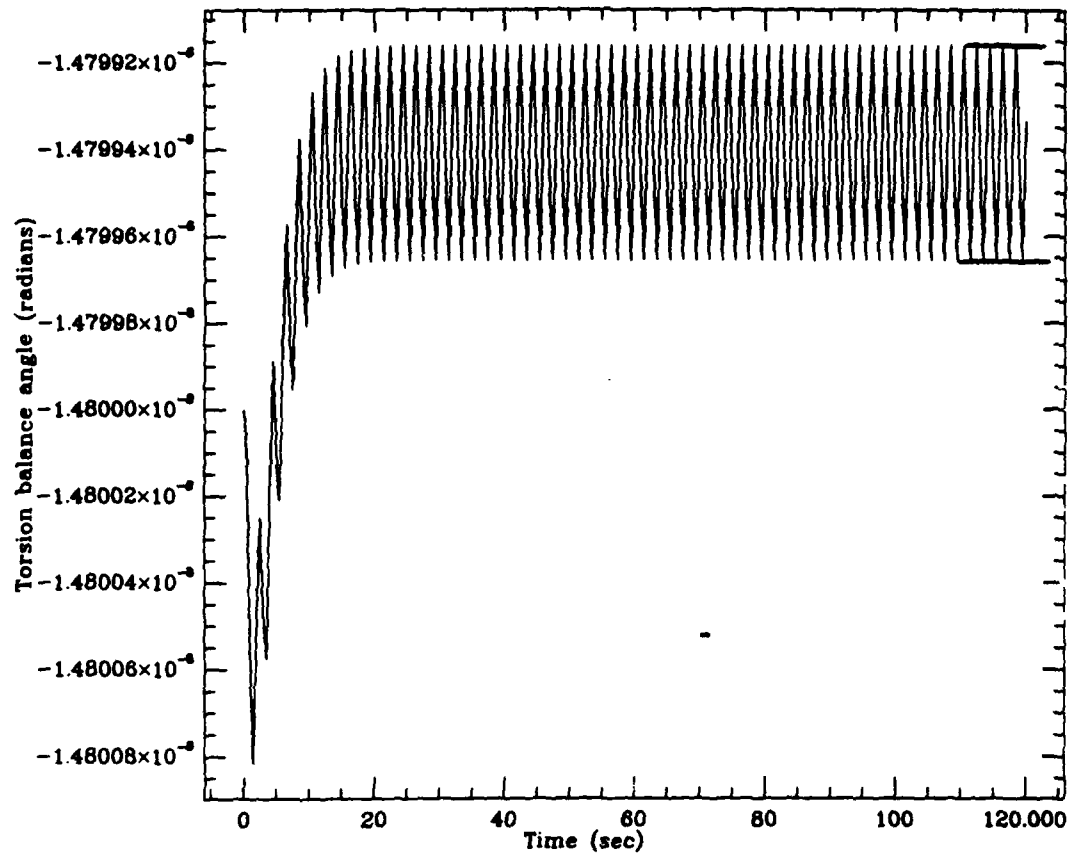


Figure 13(a). G

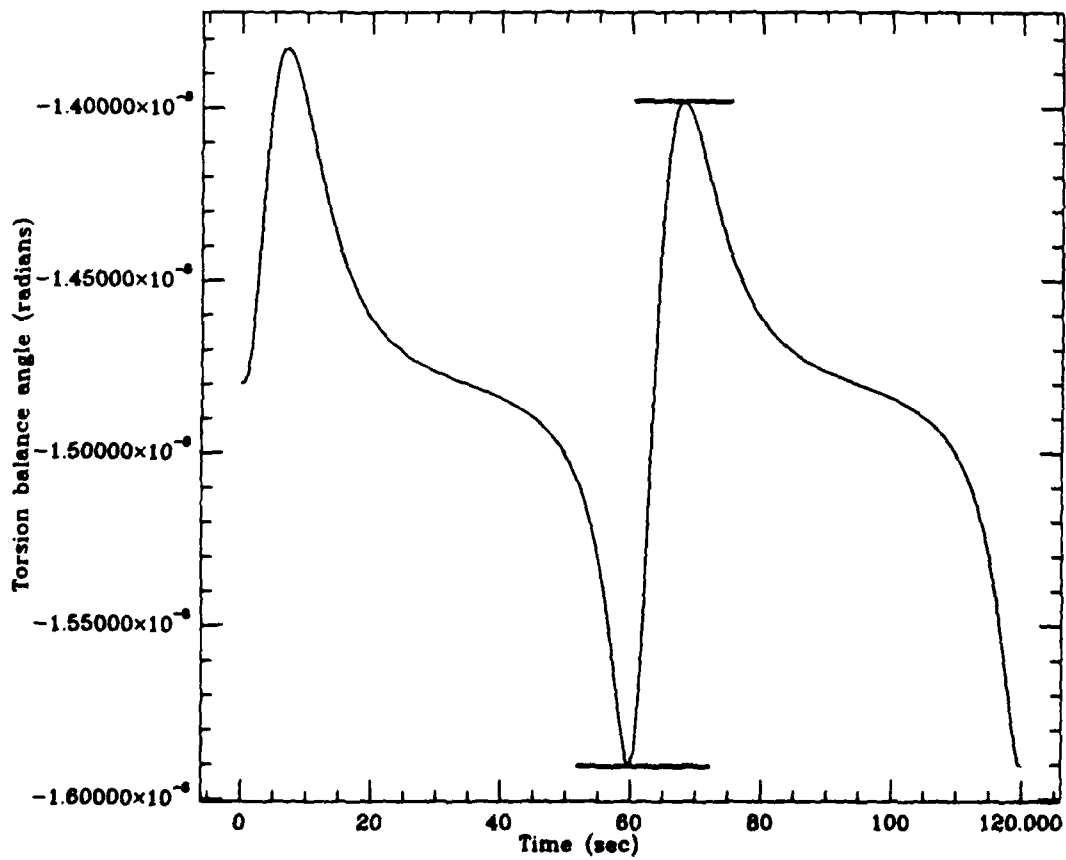


Figure 13(b). G+N

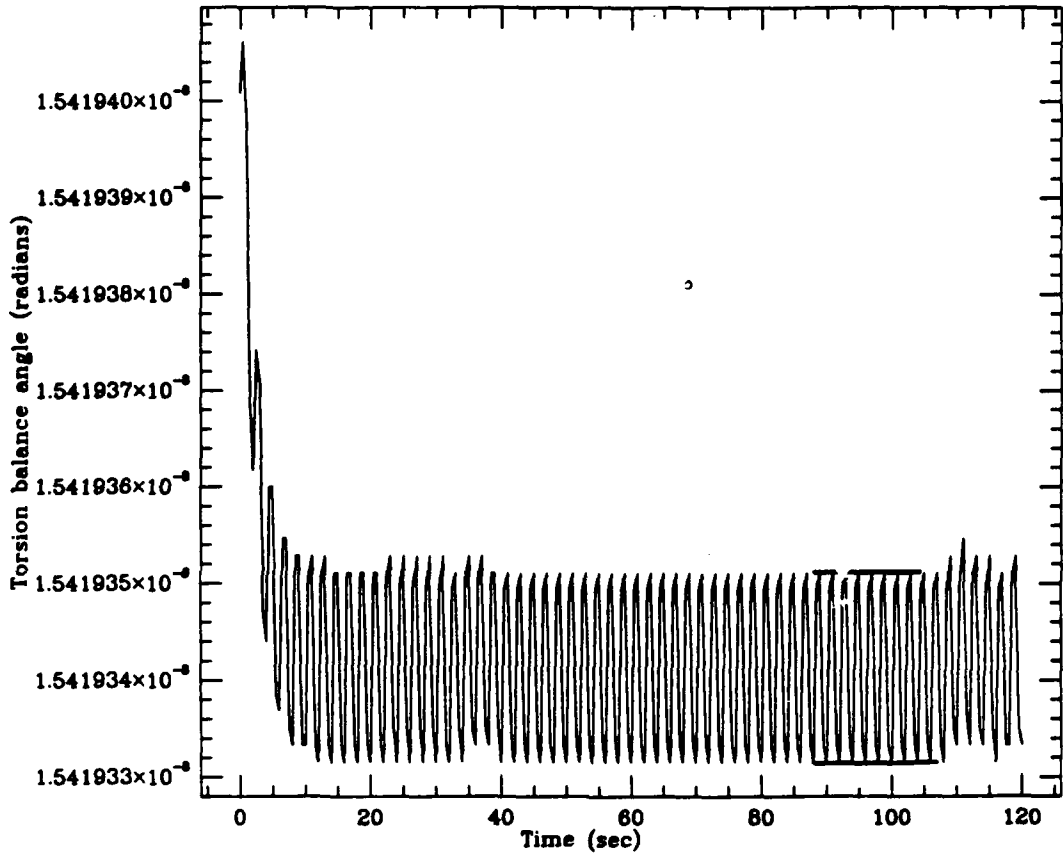


Figure 14(a). G

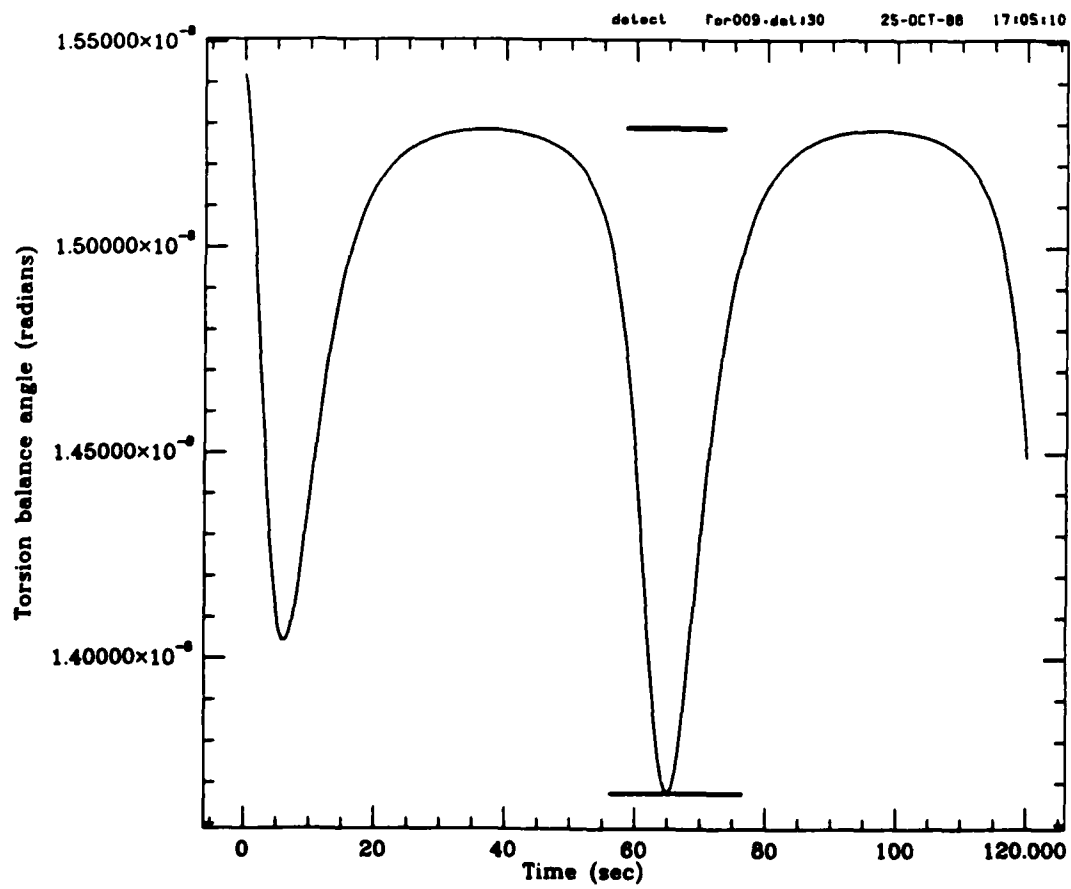


Figure 14(b). G+N

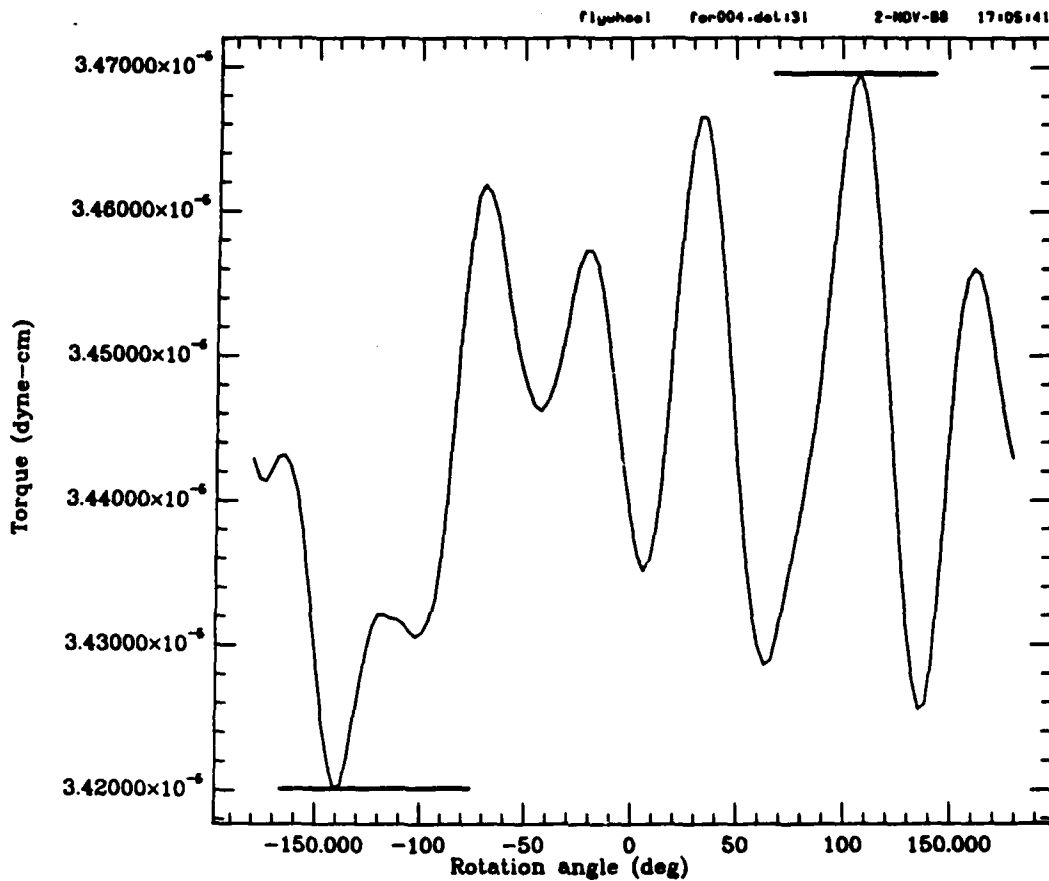


Figure 15(a). G+ΔG

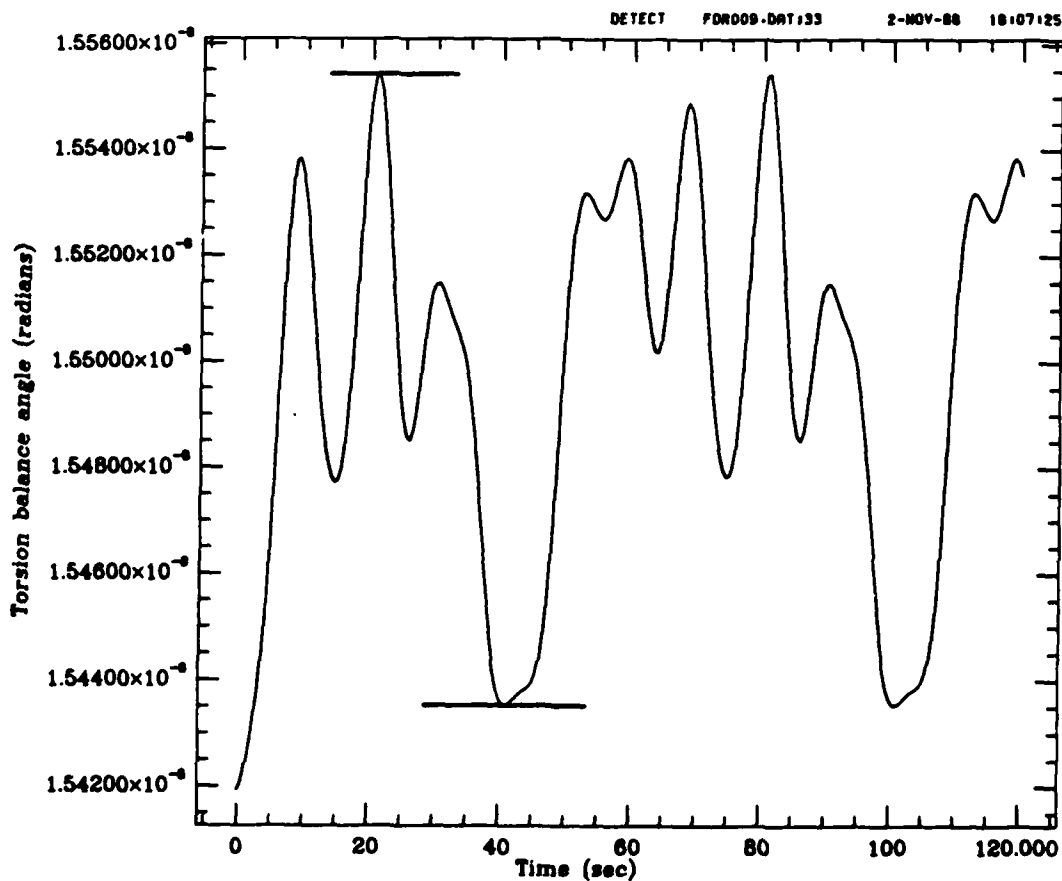


Figure 15(b). G+ΔG

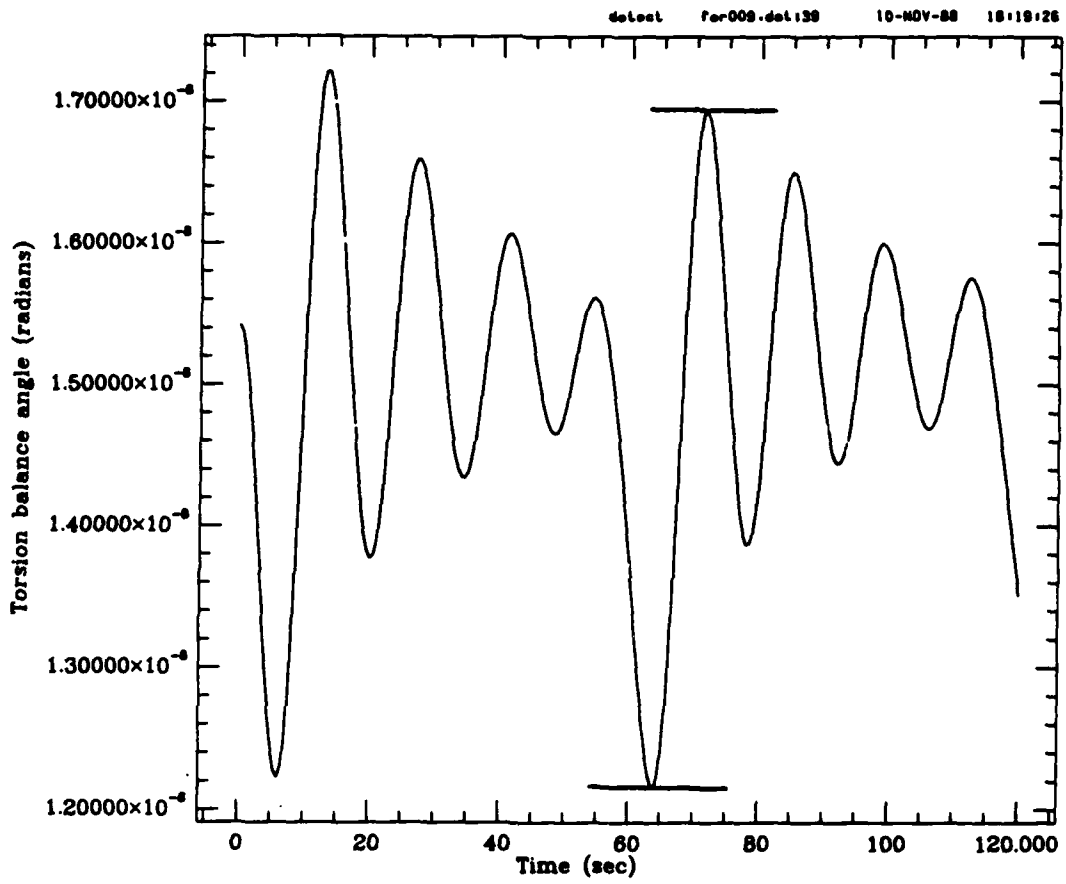


Figure 15(c). $G+\Delta G+N$

Flgwhel for004.del132 2-NOV-88 17:11:06

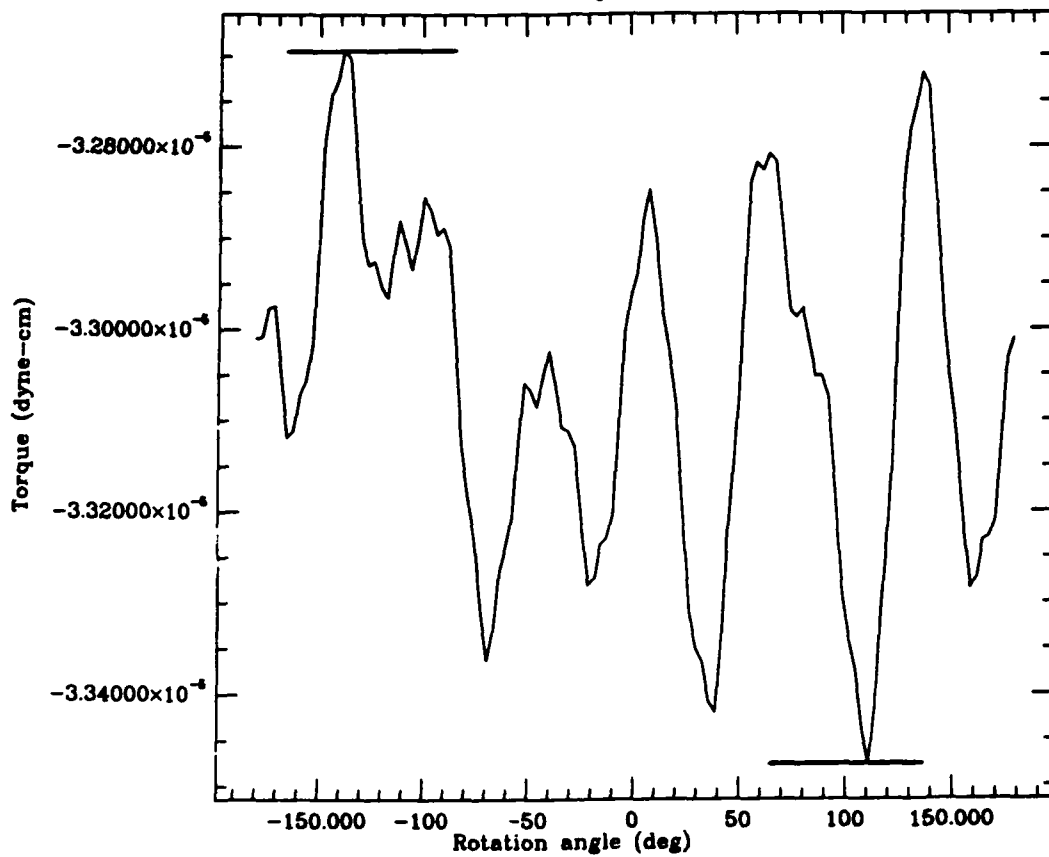


Figure 16(a). G+ΔG

DETECT FOR009.DRT:34 2-NOV-88 18:13:15

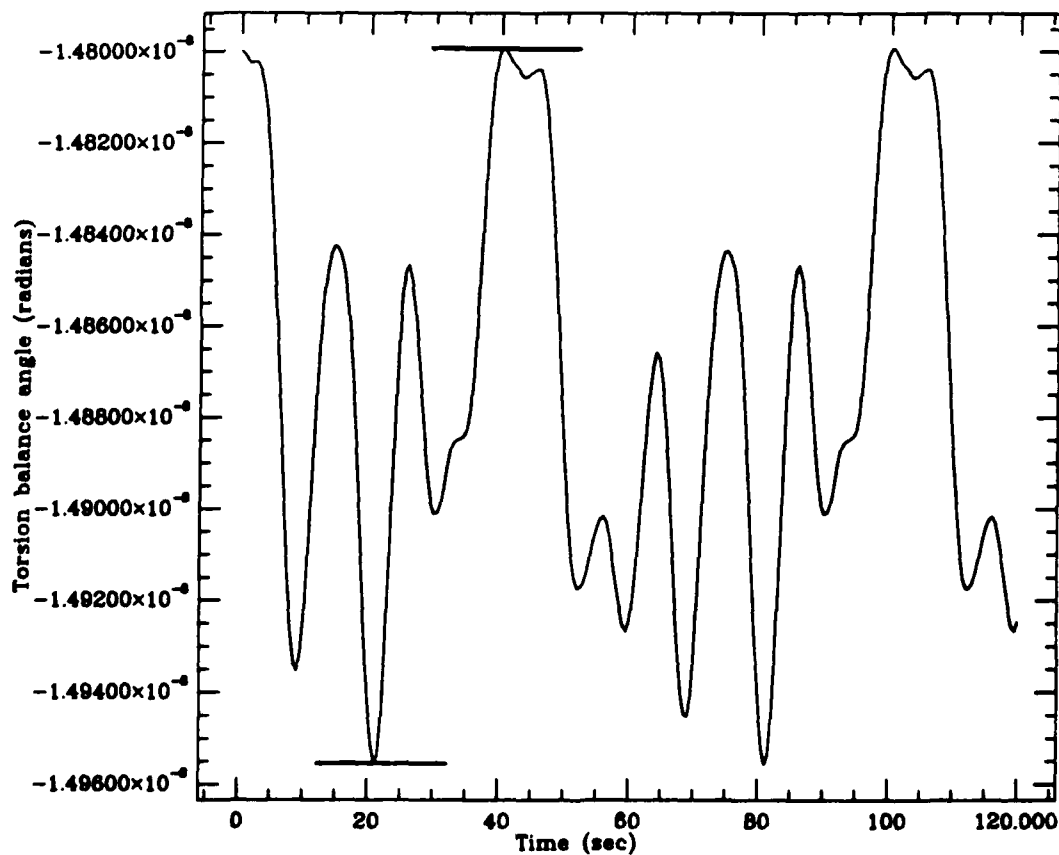


Figure 16(b). G+ΔG

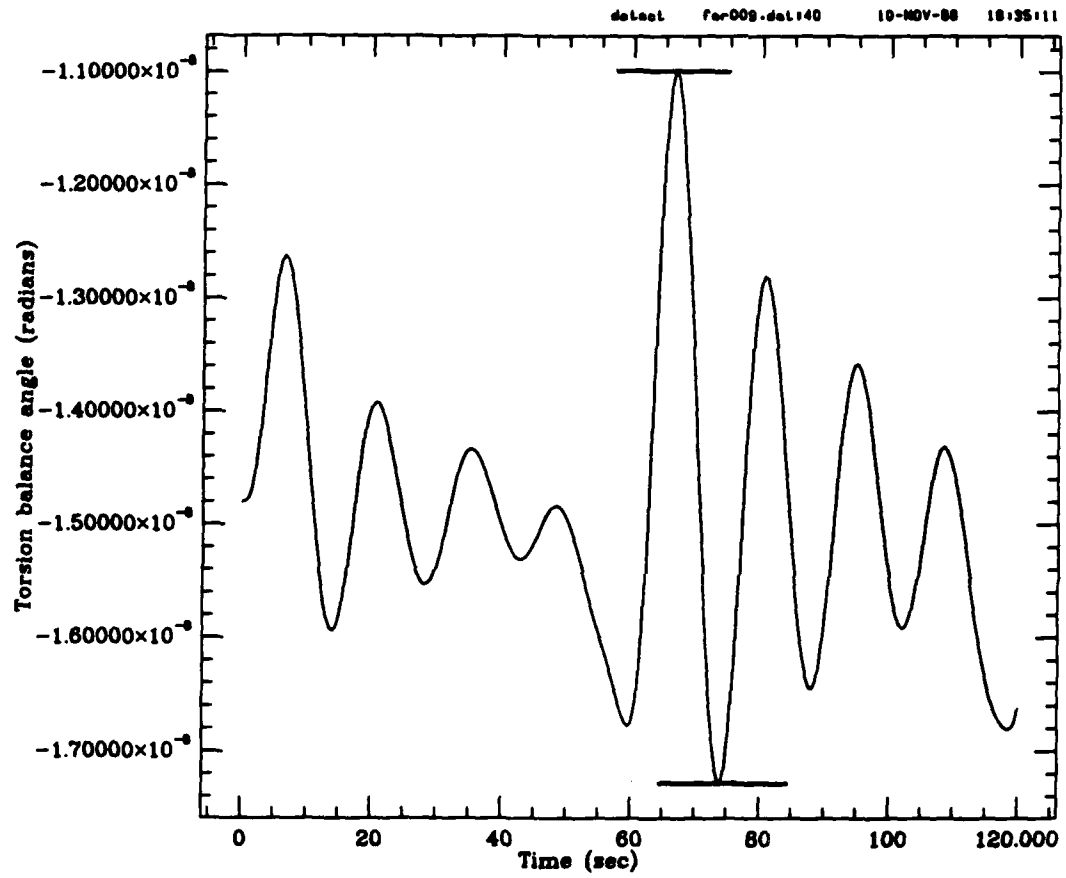


Figure 16(c). G+ΔG+N

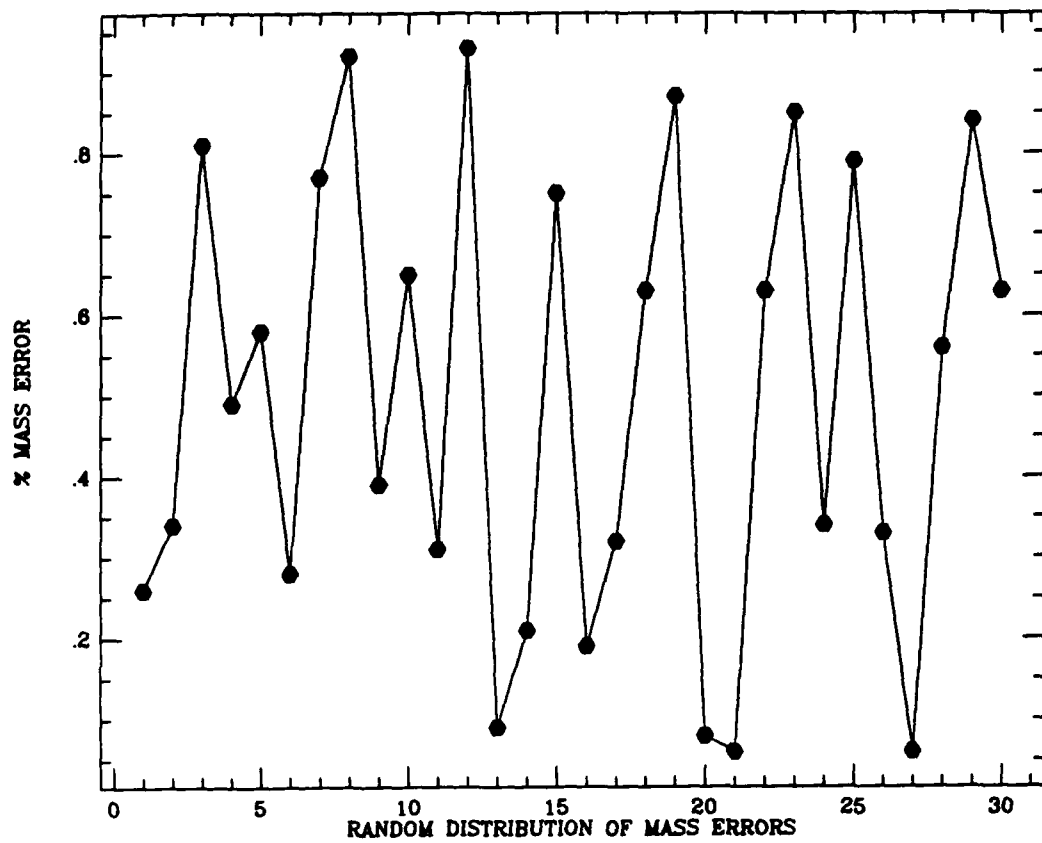


Figure 17(a).

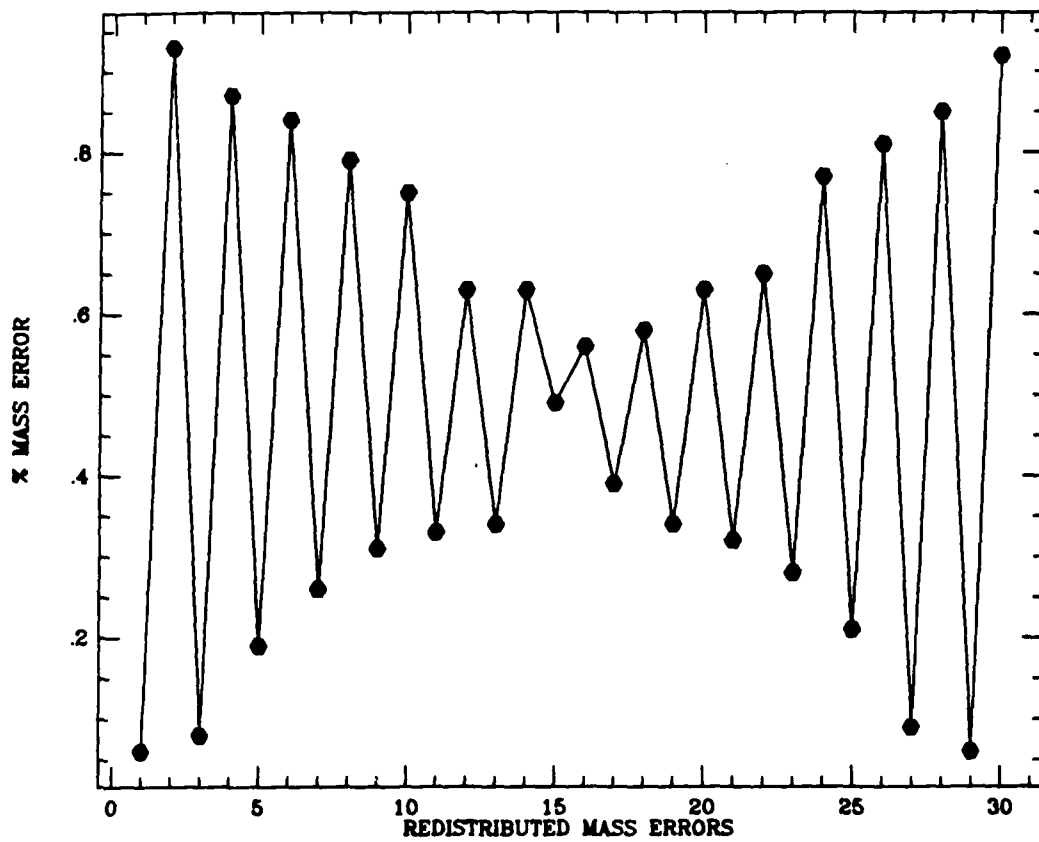


Figure 17(b).

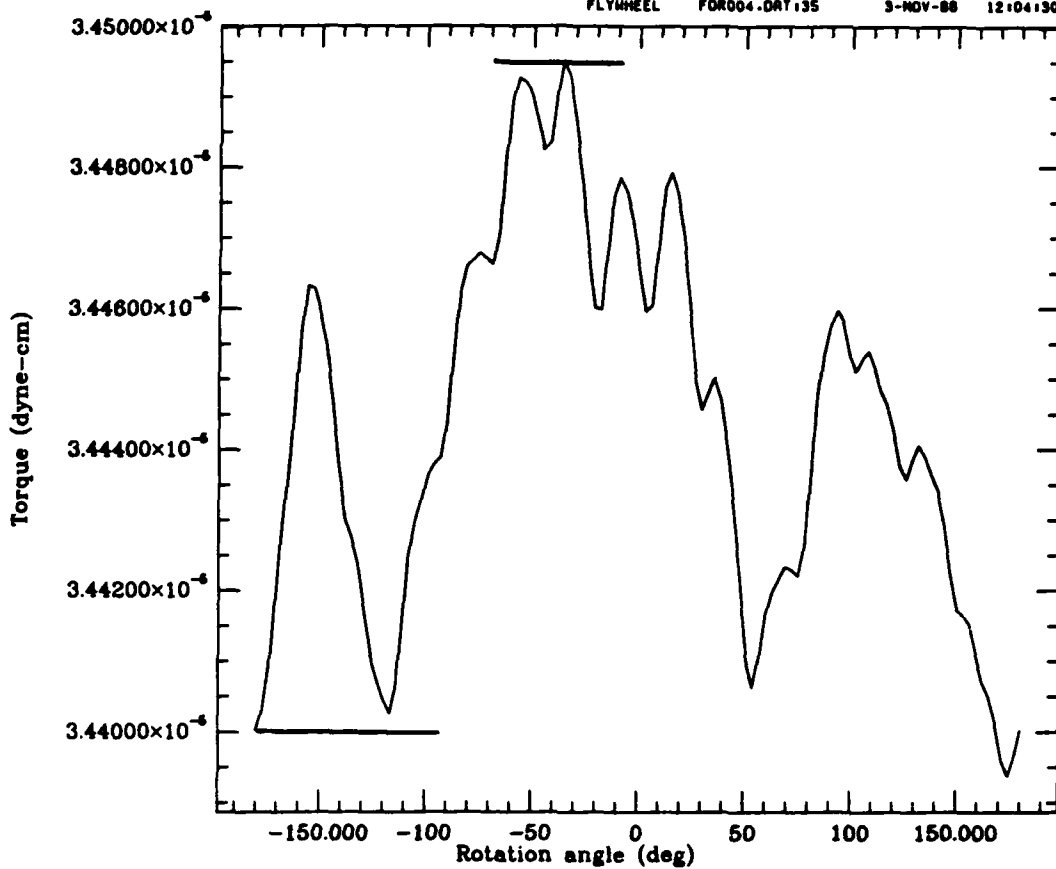


Figure 18(a). $G+\Delta G'$

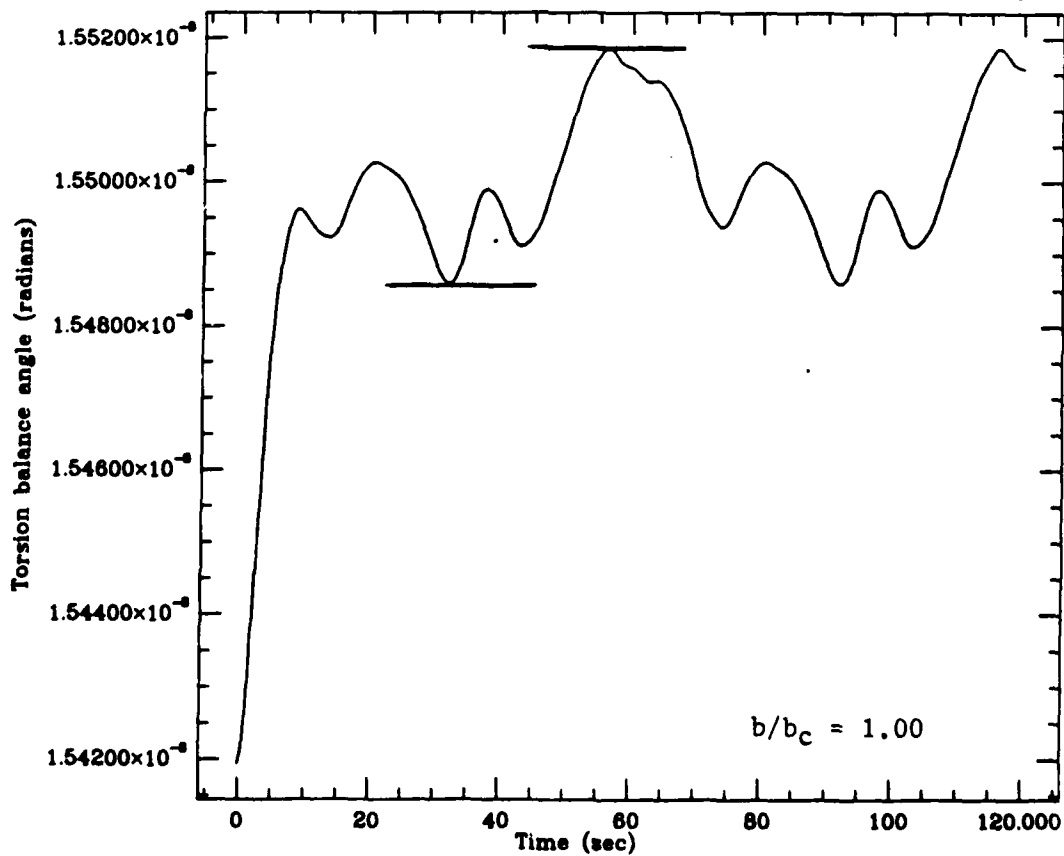


Figure 18(b). $G+\Delta G'$

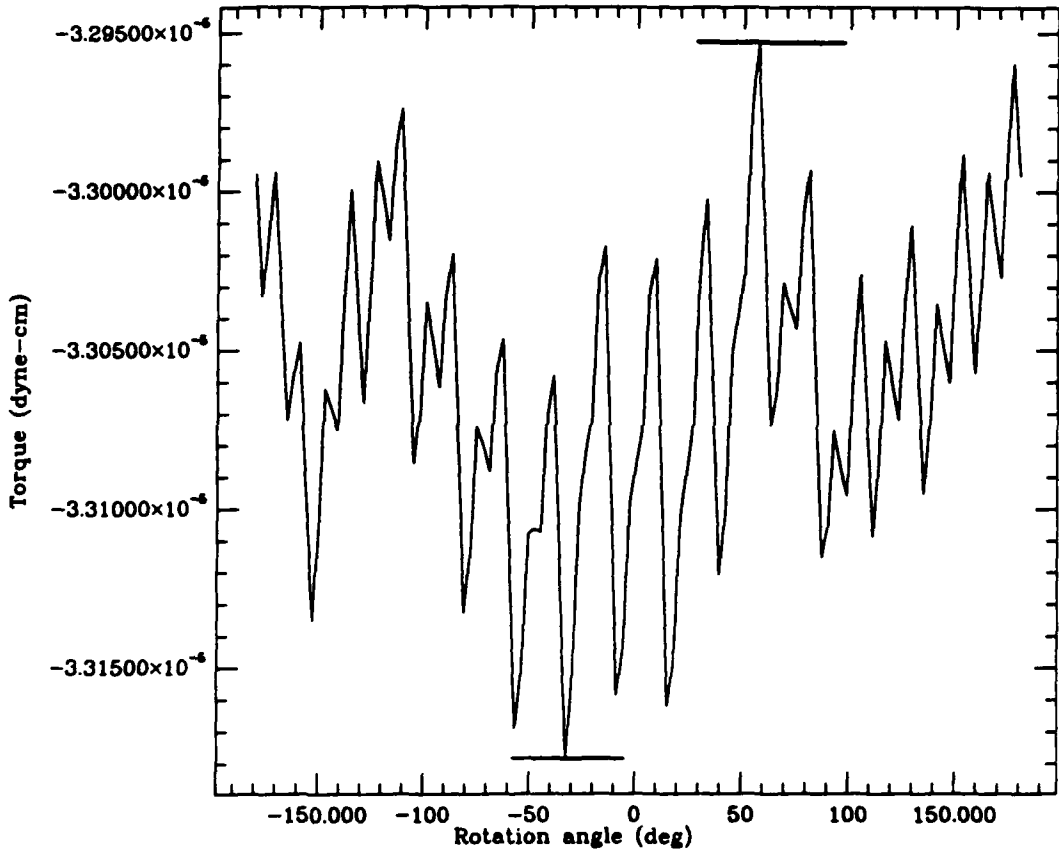


Figure 19(a). $G + \Delta G'$

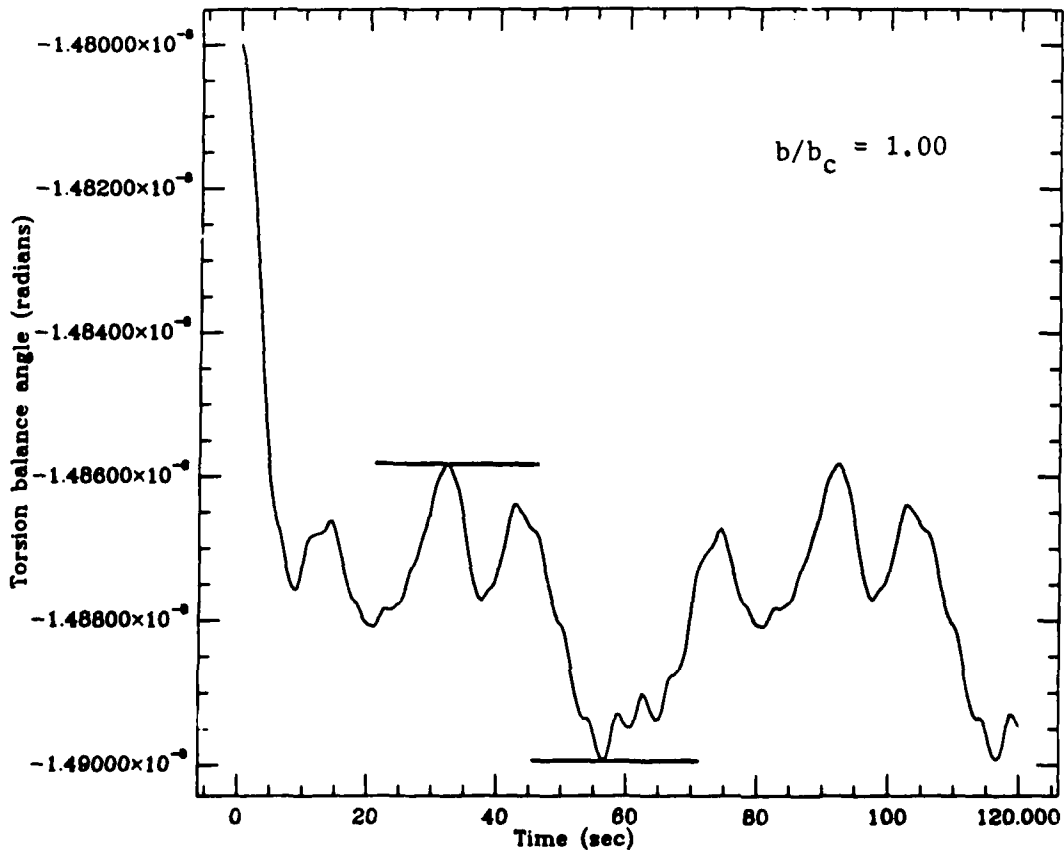


Figure 19(b). $G + \Delta G'$

2. EXPERIMENTAL ACTIVITY AT LANL WITH WEBER TORSION BALANCE

2.1 Instrumentation System (*)

2.1.1 General

The instrumentation system consists of the room-temperature torsion balance constructed by Prof. Joe Weber at University of Maryland, the Raytheon 1 RPM rotating table (with mountings, at the edge of its rim, for the tritium source or the deuterium container), and the data acquisition system (with signal integration provisions) that Raytheon designed and implemented, based on a computer-controlled LabTech Notebook data acquisition/processing approach.

A description of the room-temperature torsion balance and the 1 RPM rotating table can be found in our Fifth Quarterly Report dated 15 August 1988, and will not be repeated here. A summary of the characteristics of the overall instrumentation system can be found in Section 2.2 of this report, with emphasis on those aspects of the data acquisition system that have not been illustrated before.

We remind the reader that the output of the torsion balance is an analog voltage \pm (10 to 100) microVolt, superimposed on a slowly varying, drifting DC bias in the range \pm 10 Volt. Equivalent noise input is about 278 microVolt rms. The signal goes by coaxial cable to the analog input interface of a DT 2801/5716 data acquisition card in the data acquisition system.

(*) Contributed by Michael Thibodeau, Raytheon Submarine Signal Division

2.1.2 Data Acquisition System

2.1.2.1 System Composition

Data Acquisition System Hardware

Personal Computer

- Leading Edge Model D2 (IBM PC/AT compatible)
- 30 MB Hard Disk
- Epson Color Monitor

Data Acquisition Computer Card

- Data Translation Inc. Analog and Digital Data Acquisition Board
- Model DT2801/5716 (for IBM PCs and compatibles)
- 8 Analog (differential) inputs - 16 bit A/D
- 2 Analog (differential) outputs - 12 bit D/A
- 16 bit Digital I/O (separated into two 8 bit I/O ports)
- Maximum Analog Input Rate - 2.5 kHz
- Maximum Analog Output Rate - 14.8 kHz

Data Acquisition Software

- LABTECH NOTEBOOK Data Acquisition Software
- Real-time display processing and data streaming to hard disk at rate of up to 400 samples per second

Supporting Hardware

SA 5115B-3 1-RPM Rotating Table

- Used to rotate experimental masses close to the Torsion Balance
- Masses are placed on outside edge of table

- Controlled by SD-538 Pedestal/Interface Controller

SD-538 Pedestal/Interface Controller

- Used to maintain the SA 5115B-3 Rotating Table at an angular velocity of 1 RPM
- Outputs angular position data of the Rotating Table via 18 digital data lines

HP9845B Computer

- Outputs Start and Stop Codes to the SD-538 Pedestal Interface Controller

Please refer to Figure 2.1 for a layout of the Data Acquisition System and Supporting Hardware.

2.1.2.2 Inputs to Data Acquisition System

Room-Temperature Torsion Balance Input

As we have already indicated, Prof. Weber's room-temperature Torsion Balance produces an analog voltage signal in the range of \pm (10 to 100) microvolts. There is a slowly varying DC bias in the Torsion Balance output. This DC bias changed from -0.5 Volt to -1.0 volt over the initial few weeks of system operation. It went all the way from -10V to +10V in a few months.

The Torsion balance signal is carried on a coaxial cable to the Analog Input Interface of the DT2801/5716 Data Acquisition Card. Before being passed to the Analog Input Interface, the Torsion Balance input line passes through a grounded metal box to prevent outside EM wave interference.

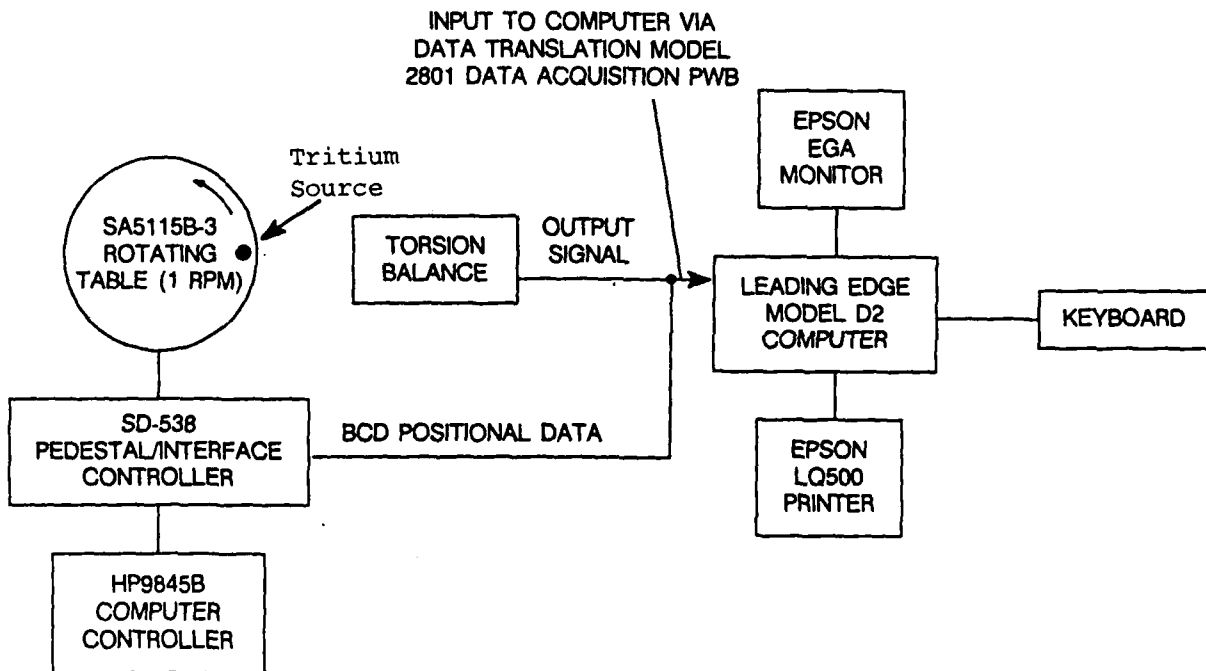


Figure 2.1. Data Acquisition System in use with the 1 RPM Rotating Table at LANL/TA-33

SD-538 Pedestal Controller Digital Input

The SD-538 Pedestal Controller Unit is a servomechanism controlling the rotation of the 1-RPM rotating table. One of the usable outputs of this unit are 18 digital data lines that report the current angular position of the rotating table. The angular position is given in degrees using a Binary Coded Decimal (BCD) code. One bit of this code is output by each digital data line. A group of four bits represents one digit of the angular position in degrees.

The Data Acquisition System is able to use only 14 of the 18 bits available in the angular position. This allows for a range of 000.0 to 359.9 degrees of angular position with an accuracy of one decimal place. The Data Acquisition System uses this angular position information to determine exactly when to sample the Torsion Balance signal.

The 14 digital data lines transfer the angular position to the DT2801/5716 Data Acquisition Card. Each digital data line carries a TTL level signal and is buffered at the point of origin to prevent loading effects caused by the Digital I/O Interface of the Data Acquisition Card. As with the Torsion Balance Input, the digital data lines pass through a grounded metal box to prevent outside EM wave interference.

2.1.2.3 Sampling

Samples of the Torsion Balance signal are taken every 10 degrees of table rotation. This sampling definition results in a total of 36 samples for every cycle of table rotation.

The Data Acquisition System uses the angular position information to determine when the table has moved 10 degrees, as per sampling definition. The angular position is sampled at a rate

of 5 Hz. This is the maximum sampling rate allowable in the current Data Acquisition System configuration.

When the rotating table passes through a 10 degree increment, a certain bit pattern is present in the angular position information. Upon detection of this pattern, the Labtech Notebook software instructs the DT2801/5716 Data Acquisition Card to take a sample of the Signal at the output of the Torsion Balance. In this way we do not rely on time information to establish the instant at which a sample is taken at the output of the torsion balance. This would require time synchronization between table rotation and sample taking, a provision that proved difficult to mechanize with the LabTech Notebook approach. We adopted instead another criterion: we decided to take a sample at the output of the torsion balance on the basis of the angular position of the rotating table. Every time that the table rotates 10°, we take a sample at the output of the torsion balance, therefore we take 36 samples during an entire rotation (360°) of the table.

2.1.2.4 Data Storage

Each sample of the Torsion Balance signal is stored in a file on the hard disk in the computer. For each Torsion Balance signal sample, the angular position of the rotating table and the time since the start of the experiment are also recorded on the hard disk.

Due to the duration of the time integration, the amount of data stored for each run of the experiment will be 7 - 10 megabytes.

2.1.2.5 Display Algorithm

The Labtech Notebook software allows for real-time data processing and displays. The real-time processing that is currently being performed by the software is a transversal integration. A transversal integration, due to the inherent properties of random Gaussian noise, increases the signal-to-noise ratio of a periodic signal and can be applied to the periodic Torsion Balance signal to improve its signal-to-noise ratio.

As noted above, the Torsion Balance signal is sampled 36 times per cycle of rotation of the table. Each separate sample of the period of the Torsion Balance signal corresponds to a certain angular position of the rotating table.

For each experiment run, data are collected for approximately 168 hours. This corresponds to approximately 10,000 rotations of the table. This means that data on approximately 10,000 one-minute periods (with 36 samples per period) of the Torsion Balance signal are collected.

What we call a "transversal integration" consists of the following:

- a) for each rotation of the 1 RPM table (360° in about 1 minute, 6° per second, 10° in 1.66666 seconds), we take 36 samples, each 10° apart. They are labeled the 0^{th} , 1^{st} , 2^{nd} , 35^{th} sample, and are recorded with this label on the hard disk;
- b) We then add together the samples that have the same order number (0^{th} , 1^{st} , 35^{th}) in each cycle of table rotation (there are about 10,000 table turns in every experiment). In other words, we add up all the 0^{th} together, all the 1^{st} together, etc. This is actually done

by adding the results, sample-by-sample, of the $(n + 1)^{\text{th}}$ table rotation to the accumulation of the previous n table rotations. However, every time that we add a new set of 36 samples, we take out the mean value. The reason is as follows: we have already indicated that the torsion balance has a DC drift of ± 10 Volt in a few months of operation. We want to take out this drift before the new set of 36 samples goes on record.

- c) The end result of the "transversal integration" is a set of 36 sums (each one made of about 10,000 addends) displayed on an x-axis of 36 angular intervals. The Signal-to-Noise ratio, in performing the "trasversal integration", increases from the initial value to a final value that is $(10,000)^{1/2}$ = 100 times better.

The zero-mean transversal integration consists of simply adding together the samples in each separate table rotation period that correspond to the same angular position (i.e. add together all the samples taken at 10 degrees, then add together all the samples taken at 20 degrees, etc.). The result of the transversal integration is a set of 36 sums that represents one minute of the original Torsion Balance signal, but with an increased signal-to-noise ratio.

These 36 sums are shown in Figure 2.2 as a set of vertical bars. The sum of all samples taken at 0 degrees is shown as the left-most vertical bar. The sum of all samples taken at 350 degrees is shown as the rightmost vertical bar. The number labelled "Cycle No." shows over how many table periods the Torsion Balance signal has been transversally integrated over. In Figure 2.2, the Cycle No. is 3846 which means each one of the vertical bars represents the sum of 3846 signal samples.

Figure 2.2 is a hard copy of what is displayed on the computer color monitor during the course of each run of the experiment.

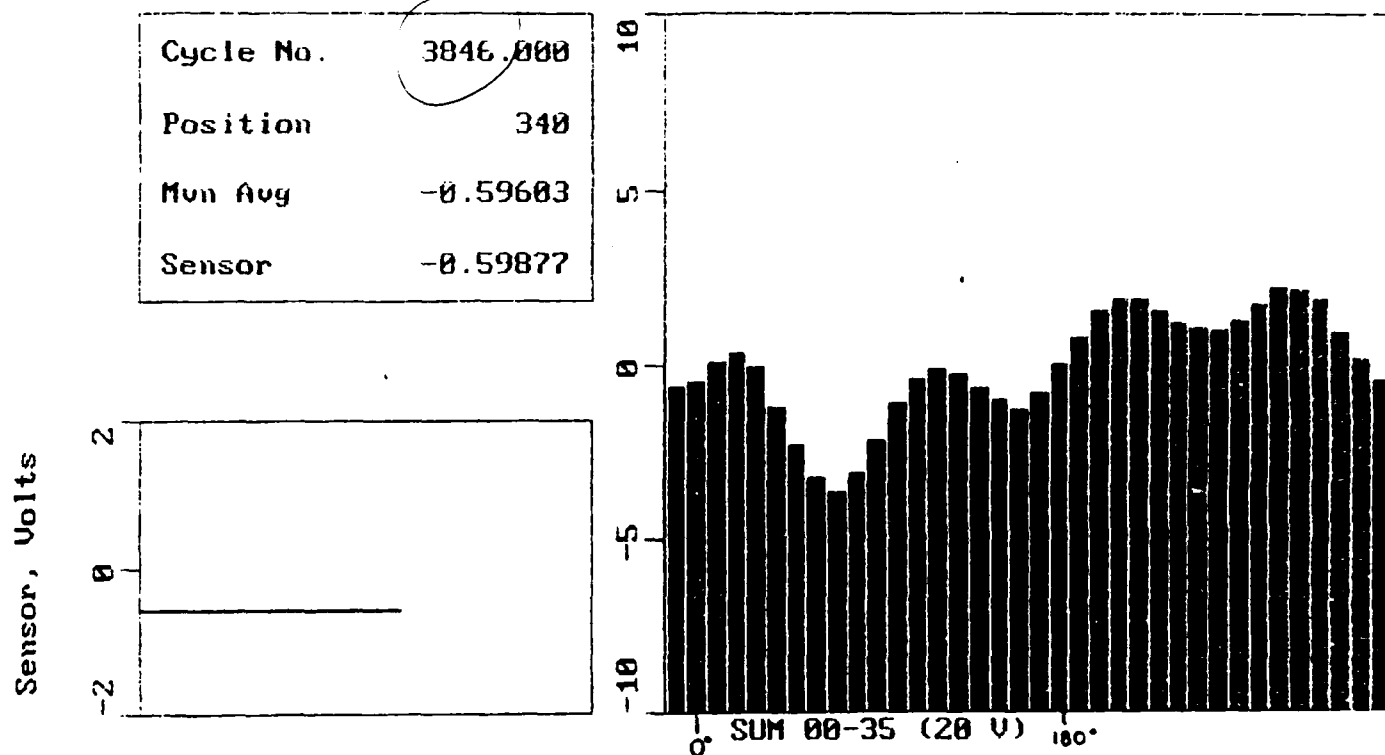


Figure 2.2 Display of the output of the data acquisition system (an example of system calibration runs)

10/24/88 - 9:30 AM (end) MDT

WEBER OUTPUT ATTACHED TO DATA ACQUISITION SYSTEM

20 kg, 6" radius brass sphere placed at approximately 355° position

BRASS SPHERE PLACED ON 3/4" radius, 1/8" height RUBBER O-RING

CENTER OF MASS OF 6" BRASS SPHERE APPROX 1/2" ABOVE TORSION BALANCE "+" LOCATOR

Figure 2.2. Display of the Output of the Data Acquisition System (An Example of System Calibration Runs)

This hard copy can be obtained only at the end of each run of the experiment.

The photographs in Figure 2.3 (a), (b), (c), (d), and (e) give various views of the instrumentation system installed at TA-33.

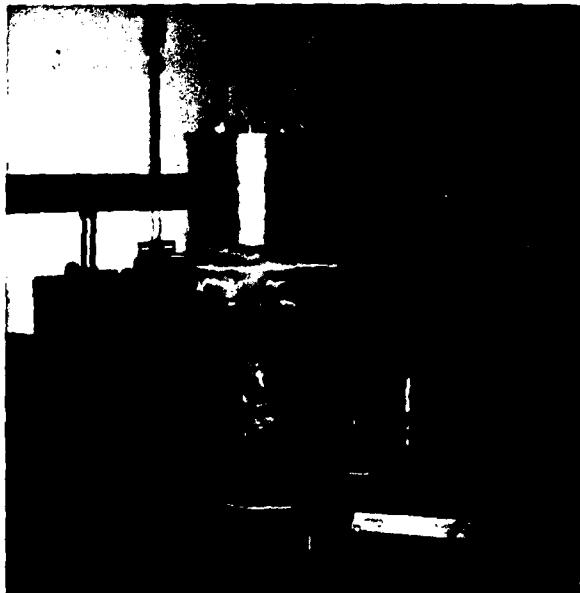
Figure 2-3 (a) shows the 1 RPM rotating table, with the table top (40.01" diameter) removed from the table. Figure 2.3 (b) shows the tritium source mounted on the table top, Figure 2.3 (c) illustrates how the 1/4" lead sheet is wrapped around the 8" cylinder that contains the torsion balance. In Figure 2.3 (d) the shielding of the torsion balance has been complemented with a PERMAG metglass magnetic shield. This is how the sensor looks from the outside when in use for data collection. Finally, Figure 2.3 (e) gives an overall view of the instrumentation system, inclusive of the Leading Edge D2 Computer, the Epson EGA Monitor, and the Epson LQ 500 Printer.



(a)



(b)



(c)



(d)

Figure 2.3. Photographs of the Instrumentation System: (See Text for Details) (a), (b), (c), (d) (Sheet 1 of 2)



(e)

Figure 2.3. Photographs of the Instrumentation System:
(e) Overall View (Sheet 2 of 2)

2.2 CALIBRATION OF THE OVERALL INSTRUMENTATION SYSTEM (*)

In order to calibrate the overall instrumentation system (inclusive of the 1 RPM rotating table, torsion balance and data acquisition system), we have mounted a brass sphere (constructed by LANL), of precisely known mass, on the rim of the table. The mass of the sphere (with diameter 16.4 cm) was measured to be 19,934.06 gram, with 3 sigma error 0.08 gram. The distance of the center of the sphere from the axis of the torsion balance (at the closest approach) was measured to be 19.84 cm, with 3 sigma error 0.1 cm. The calibration consisted of determining the ratio:

$$\frac{\text{Signal Intensity at the output of the torsion balance (in Volt)}}{\text{Grav. grad. produced at torsion balance by calibr. sphere (in EU)}}$$

In the fraction above, EU= Eötvös Units, with $1 \text{ EU} = 10^{-9} \text{ sec}^{-2}$. The noise of the torsion balance, connected to the data acquisition system (with table in rotation, but without any mass mounted on the table top) was measured (see Figure 2.2-1) by integrating it for 25 cycles (25 minutes) and by determining its rms value. This was found to be 1.39 millivolt after 25 integration cycles, corresponding to a rms value of 277.97 microVolt before integration. By displaying the input noise on a very sensitive Nicolet digital scope, we could determine that this noise is the superimposition of 60 cps hum on random noise (unabatable thermal noise at the input of the amplification chain). It should be possible in follow-on efforts to eliminate the hum. In this case, the residual noise would have an intensity of about 45 microVolt rms. At present, the Signal-to-Noise ratio after integration, when using the calibration sphere is +20.6 dB rms/rms and + 25.75 dB peak/rms. From Figure 2.2-2, we derive the following values for the intervening parameters :

● Waveform peak intensity ($S_{pk} + N_{rms}$) (the waveform in Figure 2.2-2 has been obtained after 180 integrations)	76.05 Millivolt (peak of the first swing of torsion balance oscillation)
● Waveform rms (S + N) rms	43.71 Millivolt
● rms Noise (after 180 integrations)	3.7293 millivolt

(*) Contributed by M.D.Grossi, PI.

Sample Number	Amplitude A	A ²
# 1	+ 1.13	1.28
2	- 1.7	2.89
3	- 0.8	0.64
4	+ 1.81	3.28
5	- 0.5	0.25
6	-1.4	1.96
7	- 0.5	0.25
8	+ 2.76	7.62
9	+ 1.48	2.19
10	+ 2.98	8.88
11	+ 0.15	0.02
12	- 0.8	0.64
13	+ 1.18	1.39
14	- 2.00	4.00
15	- 0.15	0.02
16	- 1.75	3.06
17	- 0.85	0.72
18	+ 0.86	0.74
19	+ 1.96	3.84
20	+ 0.33	0.11
21	+ 1.28	1.64
22	+ 1.23	1.51
23	- 0.4	0.16
24	+ 0.33	0.11
25	- 0.75	0.56
26	- 1.4	1.96
27	- 2.85	8.12
28	+ 0.53	0.28
29	- 1.65	2.72
30	+ 0.63	0.40
31	+ 1.23	1.51
32	- 0.15	0.02
33	+ 1.23	1.51
34	- 2.0	4.00
35	- 0.4	0.16
36	- 1.05	1.10

Computation of rms amplitude :

$$\left[\frac{1}{T} \int_0^T f(t)^2 dt \right]^{\frac{1}{2}} = \left[\frac{1}{36 \times 1.667} \sum_0^T f(t)^2 \Delta t \right]^{\frac{1}{2}} = \left[\frac{1}{36} \sum_0^T f(t)^2 \right]^{\frac{1}{2}}$$

$$\sum A^2 = 69.54$$

$$\frac{\sum A^2}{36} = 1.9317$$

$$\sqrt{\frac{\sum A^2}{36}} = 1.39 \text{ millivolt} \quad (\text{with 25 integration cycles})$$

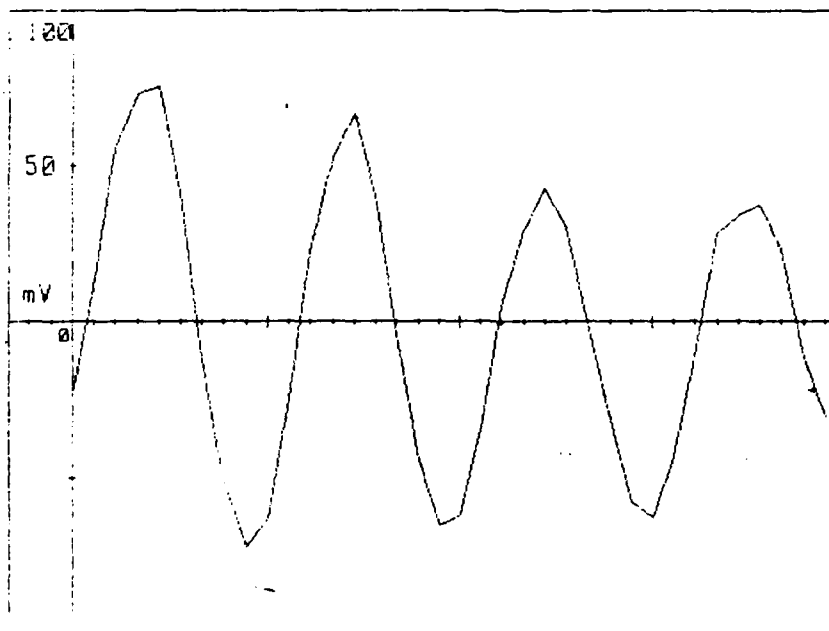
rms intensity of the noise, prior to integration : 277.97 microVolt
 mean value of noise \approx 0 microVolt

Figure 2.2-1 . Computation of the rms intensity of the Noise at the output of the torsion balance

BRASS BALL 703 RUN 01: 180 CYCLES - WEBER INPUT - 20 KG BRASS BALL AT 0.00
 - TABLETOP ON - TABLE POSITION NORMAL - NO MAGNET

1	-.02335	13	.05271	25	-.00049
2	.01113	14	.06697	26	-.03155
3	.05597	15	.04096	27	-.05805
4	.07304	16	-.0046	28	-.06321
5	.07605	17	-.04432	29	-.04364
6	.04214	18	-.06547	30	-.01095
7	-.01211	19	-.06216	31	.02841
8	-.05046	20	-.03414	32	.03394
9	-.07248	21	.00472	33	.03761
10	-.06277	22	.02952	34	.02359
11	-.02469	23	.0427	35	-.01177
12	.02256	24	.03056	36	-.03038

INPUT ITEM # TO CHANGE (0 FOR NONE)



NOTE- Amplitude of the first peak is 0.07605 Volt = 76.05 millivolt
 after 180 integration cycles.

Figure 2.2-2 Calibration Run With the 20 Kg
 Brass Ball-Torsion Balance Tests

• Processing gain (180 integrations)	+22.55 dB
• Signal after integration	
rms value	43.44 millivolt
peak value	75.95 millivolt
• Signal before integration	
rms value	242 microvolt
peak value	422 microvolt

In order to determine the gravity gradient produced by the brass sphere, we verified from the graphs in Section 1 of this report, that the maximum torque on the balance occurs when the sphere is about 15° away from closest approach (see Figure 3 (a).G). At the closest approach, the torque is nearly zero. In order to determine the gravitational accelerations induced in the four masses (m_1 , m_2 , m_3 and m_4) of Figure 2.2-3, we proceed as follows.

Starting from the two masses m_1 and m_2 (one of them is made of sapphire and the other of aluminum, and both have a 40.3 gr mass), we need to determine first of all \overline{CD} and \overline{CE} , so that we can compute the force acting on each one of them. We have:

$$\overline{AF} = R_o \cos 15^\circ = 39.95 \text{ cm}$$

$$\overline{FC} = R_o \sin 15^\circ = 9.633 \text{ cm}$$

$$\overline{FB} = \overline{AB} - \overline{AF} = 1.268 \text{ cm}$$

$$\overline{FD} = \overline{FB} + \overline{BD} = 13.488 \text{ cm}, \quad \overline{FE} = \overline{FD} + 15.24 = 28.73 \text{ cm}$$

$$\overline{BD} = \overline{BG} - \overline{DG} = 12.22 \text{ cm}$$

Therefore, the needed quantities are:

$$\overline{CD} = 16.57 \text{ cm}$$

$$\overline{CE} = 30.3 \text{ cm}$$

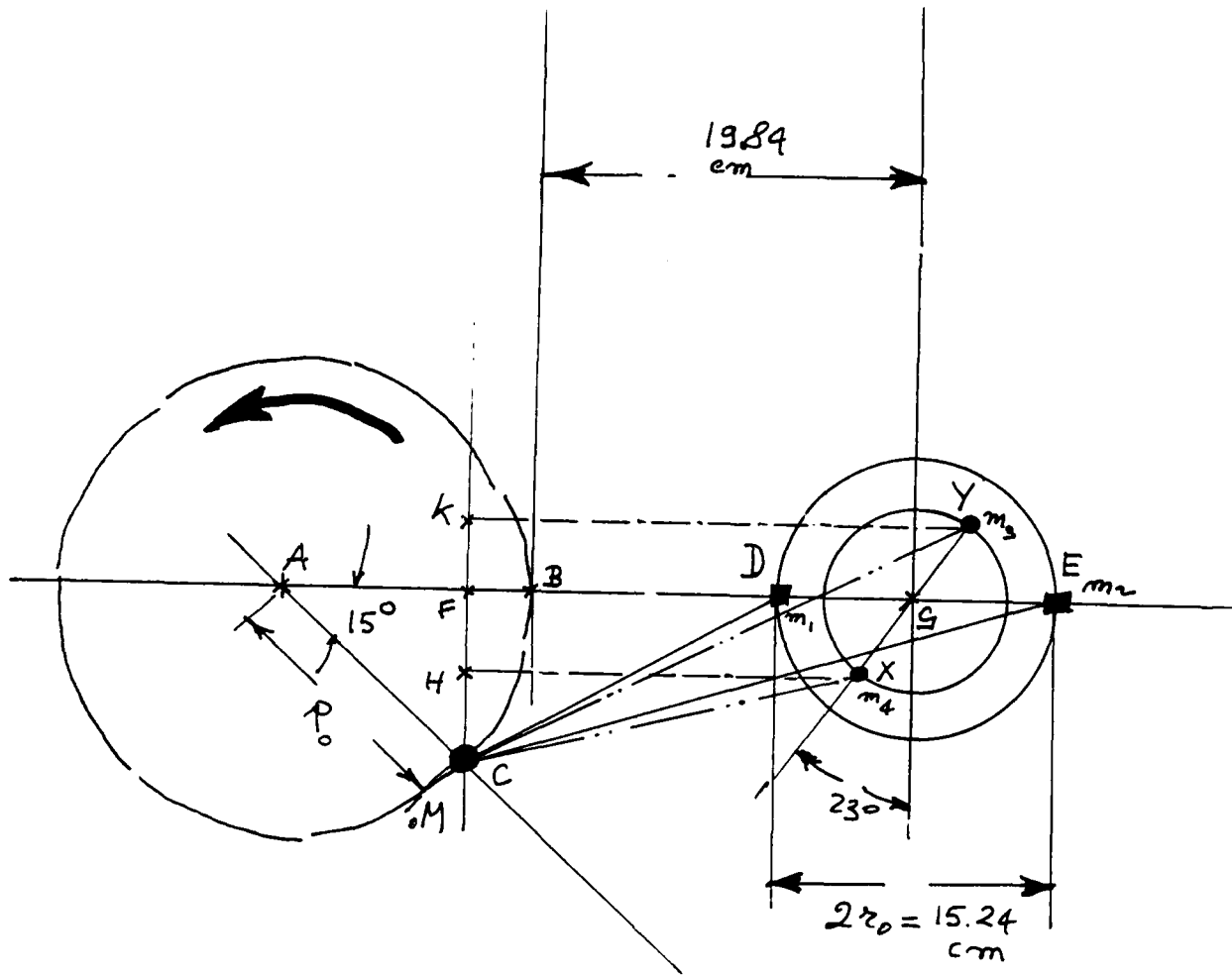


Figure 2.2-3. Geometry for Torsion Balance Calibration

The force acting on m_1 can now be computed, and is $1.95 \cdot 10^{-4}$ dyne, while the force acting on m_2 is 0.584 dynes. The projections of these forces in a direction perpendicular to \overline{DE} are respectively $1.133 \cdot 10^{-4}$ dyne and $0.185 \cdot 10^{-4}$ dyne. The differential acceleration is $2.35 \cdot 10^{-6}$ cm sec⁻² and its gradient, across \overline{DE} is $0.154 \cdot 10^{-6}$ sec⁻² = 154.32 EU.

Considering now the two masses m_3 and m_4 (these are part of the electrostatic servo and damping system, each of 19 gram), we must compute first of all the two distances \overline{CX} and \overline{CY} . We have:

$$\overline{XY} = 9.52 \text{ cm}$$

$$\overline{CF} = 9.63 \text{ cm}$$

$$\overline{FK} = 4.38 \text{ cm}$$

$$\overline{CK} = 14.01 \text{ cm}$$

$$\overline{KY} = \overline{FG} + 4.76 \sin 23^\circ = 22.97 \text{ cm}$$

$$\overline{FG} = \overline{FB} + \overline{BG} = 21.11 \text{ cm}$$

Therefore, the needed quantities are:

$$\overline{CY} = 26.91 \text{ cm}$$

$$\overline{CX} = 17.41 \text{ cm}$$

The force acting on m_3 can now be computed and amounts to $0.3489 \cdot 10^{-4}$ dyne, while the force on m_4 is $0.8333 \cdot 10^{-4}$ dyne. The projections of these forces in a direction perpendicular to \overline{XY} are respectively $1.99 \cdot 10^{-6}$ dyne and $7.354 \cdot 10^{-6}$ dyne. The differential acceleration is $2.82 \cdot 10^{-7}$ cm sec⁻² and its gradient across \overline{XY} $29.64 \cdot 10^{-9}$ sec⁻² = 29.64 EU.

When the rotating table is in the position approaching the closest approach (as shown in Figure 2.2-3) the two gradients acting respectively on the pair (m_1, m_2) and on the pair (m_3, m_4) have opposite sign and the overall gradient experienced by the torsion balance is 124.68 EU.

The calibration constant, therefore, has the value :

$$\frac{422 \mu\text{Volt peak}}{124.68 \text{ EU}} = 3.385 \frac{\mu\text{Volt peak}}{\text{EU}}, \text{ and } \frac{242 \mu\text{Volt rms}}{124.68 \text{ EU}} = 1.94 \frac{\mu\text{Volt rms}}{\text{EU}}$$

The calibration error can be evaluated as follows:

- Symbols: $(\Delta\text{Cal})^2$ mean square error in calibration (the quantity that we want to determine)
- $\frac{\partial f}{\partial a}$ sensitivity of the calibration to error in signal amplitude
 a signal amplitude, Volt; M mass, grams; r distance, cm
- $\epsilon_a =$ error in signal amplitude measurement (= rms noise)
- $\epsilon_M =$ error in determining the mass of the source on the rotating table (0.08 gr rms)
- $\epsilon_r =$ error in measuring distances (1 mm rms)
- $\frac{\partial f}{\partial M}$ sensitivity of calibration to error in mass measurement
- $\frac{\partial f}{\partial r}$ sensitivity of calibration to error in distance measurement

We have:

$$(\Delta\text{Cal})^2 = \left(\frac{\partial f}{\partial a}\right)^2 \epsilon_a^2 + \left(\frac{\partial f}{\partial M}\right)^2 \epsilon_M^2 + \left(\frac{\partial f}{\partial r}\right)^2 \epsilon_r^2$$

where

$$\frac{\partial f}{\partial a} = \frac{r^3}{GM}, \text{ with } G = 6.67 \cdot 10^{-8} \text{ cgs}$$

$$\frac{\partial f}{\partial M} = \frac{-a r^3}{G M}$$

$$r = 19.84 \text{ cm}$$

$$M = 19.93406 \cdot 10^3 \text{ gr}$$

$$\frac{\partial f}{\partial r} = \frac{3 a r^2}{G M}$$

Therefore:

$$\left(\frac{\partial f}{\partial a}\right)^2 = 3.4499 \cdot 10^{13}$$

$$\left(\frac{\partial f}{\partial M}\right)^2 = 1.54977 \cdot 10^{-2}$$

$$\left(\frac{\partial f}{\partial r}\right)^2 = 1.40807 \cdot 10^5$$

and, finally,

$$(\Delta \text{Cal})^2 = 2.4436 \cdot 10^6 + 9.988 \cdot 10^{-5} + 1.4080 \cdot 10^3$$

$$\Delta \text{Cal} = 1563.647 \text{ Volt/sec}^{-2} = 1.56365 \frac{\text{microVolt, rms}}{\text{EU}}$$

$$\frac{\Delta \text{Cal}}{\text{Cal}} \cong 46 \% \text{ rms/peak}$$

Should we succeed in reducing the noise at the input of our data acquisition chain, loaded by the torsion balance, down to 45 microVolt (this is a distinct possibility because most of the noise is 60 cps hum), the overall error in calibration (that is dominated by the SNR) would be reduced to about 7.9 % (rms/peak), and to about 13.76 % (rms/rms).

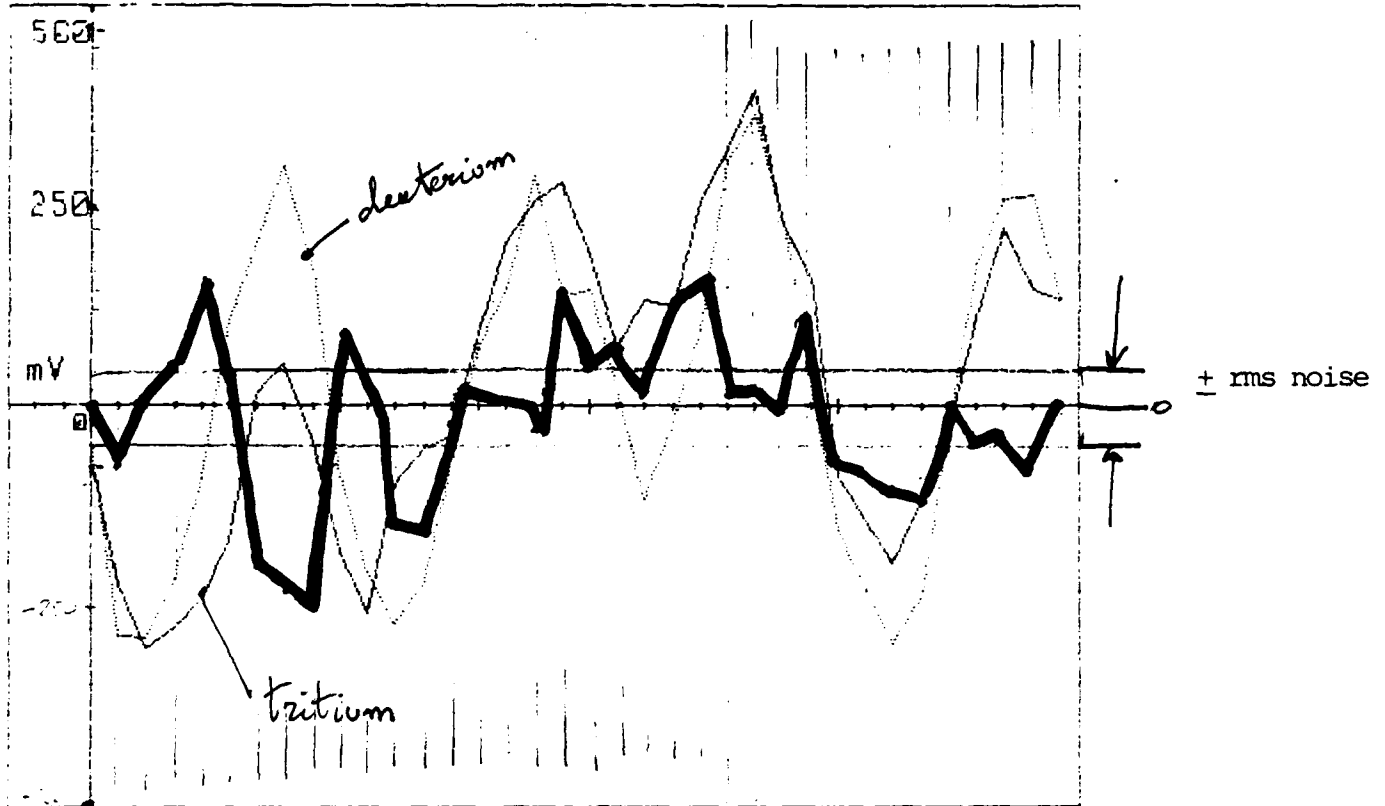
2.3 REPORT ON THE RESULTS OF DATA ACQUISITION, REAL-TIME DATA PROCESSING AND ANALYSIS (*)

The first two signal integrations of scientific value took place between November 3 and November 17, 1988. Each one lasted 8072 minutes (about 134.5 hours) and the processing gain was therefore about 39 dB.

The torsion balance was shielded by several layers of PERMAG high- μ flexible Metglass material. In these two integrations, no lead shield was in use in the system. Figure 2.3-1 shows the waveform at the output of the torsion balance for each of the two cases that we experimented with, using respectively a deuterium-filled container and a tritium-filled one. The figure provides an indication that the damped oscillations of the torsion balance are of smaller amplitude when the tritium source is in use, as compared to the case of deuterium in use. This could be interpreted to mean that the tritium container (that has the same mass of the deuterium container) is characterized by the presence of some kind of repulsion force that decreases the gravitational pull exerted on the torsion balance. The calculation of the difference curve, to determine this repulsion force, is shown in Table 2.3-1. The rms value of the (S+N) difference curve is 103.37 millivolt. Noise after integration is $\sqrt{8072} \times 2 \times 0.278 = \sqrt{8072} \times 0.3931 = 35.31$ mV, so that the Signal S, after integration, is 97.145 mV rms. Before integration, the difference Signal S (rms) is $S = \frac{97.145}{8072} = 12$ μ Volt; $\left(\frac{(103.37)^2 - (35.31)^2}{8072} \right)^{1/2} = 97.145$ mV rms).

The calibration constant (see Section 2.2) was determined to be 1.94 μ V rms/EU. We have therefore a differential Δ EU, when going from tritium to deuterium of $12/1.94 = 6.186$ EU. This correspond to a differential force ΔF of about $6.186 \times 10^{-9} \times 40.3$ gr $\times 15.24$ cm $\approx 3.8 \times 10^{-6}$ dyne. This repulsion force, of a few microdynes, would be close to the measurements performed by Professor Weber at University of Maryland in 1985.

(*) Contributed by M.D.Grossi, PI.



Dotted Dark Plot - Tritium, after 8072 integrations
 Dotted Light Plot - Deuterium, after 8072 integrations

————— Difference Curve

Figure 2.3-1. Plotting of Difference Curve
 ($|$ tritium record $| - |$ deuterium record $|$)
 No lead shield was in use.

Table 2.3-1. Computation of rms Value of Difference Curve
(See Figure 2.3-1)

NOTE: No lead shield was in use.

Sample No	A (mV)	A-Av = \bar{A}	\bar{A}^2	σ^2 (mV) ²	After	Before
					σ (S + N) (mV)	Signal & Noise
1	0	+ 17.63	310.8169	10685.399	103.37 mV _{rms}	Signal=
2	- 75	- 57.37	3291.3169			12 μ V rms
3	+ 10	+ 27.63	763.4169	(after integration)	Noise= $\sqrt{2} \times$ 277.97 μ V= = 393.1 μ V (before integration)	
4	+ 60	+ 77.63	6026.4169			
5	+160	+177.63	31552.417	Noise= $0.3931 \sqrt{8072} =$ = 35.32 mV	Signal= 97.145 mV	
6	+ 50	+ 67.63	4573.8169			
7	-200	-182.37	33258.817	● Mean Value after integration: -17.6389 millivolt (S+N)		
8	-240	-222.37	49448.417			
9	-260	-242.37	58743.217			
10	+100	+117.63	13836.817			
11	0	+ 17.63	310.8169			
12	-150	-132.37	17521.817			
13	-160	-142.37	20269.217			
14	- 20	- 2.37	5.6169			
15	+ 20	+ 37.63	1416.0169			
16	+ 20	+ 37.63	1416.0169			
17	+ 15	+ 32.63	1064.7169			
18	- 30	- 12.37	153.0169			
19	+140	+157.63	24847.217			
20	+ 60	+ 77.63	6026.4169			
21	+ 20	+ 37.63	1416.0169			
22	+130	+147.63	21794.617			
23	+150	+167.63	28099.817			
24	+ 10	+ 27.63	763.4169			
25	+ 25	+ 42.63	1817.3169			
26	0	+ 17.63	310.8169			
27	+120	+137.63	18942.017			
28	- 70	- 52.37	2742.6169			
29	- 80	- 62.37	3890.0169			
30	-100	- 82.37	6784.8169			
31	-130	-112.37	12627.017			
32	0	+ 17.63	310.8169			
33	- 70	- 52.37	2742.6169			
34	- 40	- 22.37	500.4169			
35	-100	- 82.37	6784.8169			
36	0	+ 17.63	310.8169			

A relevant question is whether the two curves labelled "deuterium" and "tritium" in Figure 2.3-1 are random processes belonging to the same distribution, so that the "difference curve" in the same Figure represents just random noise.

We have submitted this hypothesis to statistical test and we have determined that the probability that the "difference curve" is just noise is less than .01 %. Here is the proof.

Let's have a random process X normally distributed, with variance σ^2 , and let's call $S^2 = \frac{1}{N} \sum_{n=1}^N (x_n - \bar{x})^2$, where $\bar{x} = \frac{1}{N} \sum_{n=1}^N x_n$.

Then, we have :

$$\frac{N S^2}{\sigma^2} \sim \chi^2_{N-1}$$

where χ^2_{N-1} is the Chi-square random function with $N-1$ degrees of freedom.

Let's assume, for null hypothesis, $H_0 : \text{var}(x_n) = \sigma^2$, versus the alternative $H_1 : \text{var}(x_n) > \sigma^2$. In our case, $N=36$ (we have 36 samples in an ensemble)

and $x_n = |\text{tritium record}| - |\text{deuterium record}|$. The variance of the noise affecting the difference curve is $\sigma^2 = (0.28)^2 \cdot (8072 \text{ integrations})^2$. For the difference curve of Figure 2.3-1, we have :

$$S^2 = (103.37)^2 = 10,685.$$

Therefore, $\frac{36 S^2}{\sigma^2} = 304 = \chi^2_{35}$. From the Table in Figure 2.3-4, we have :

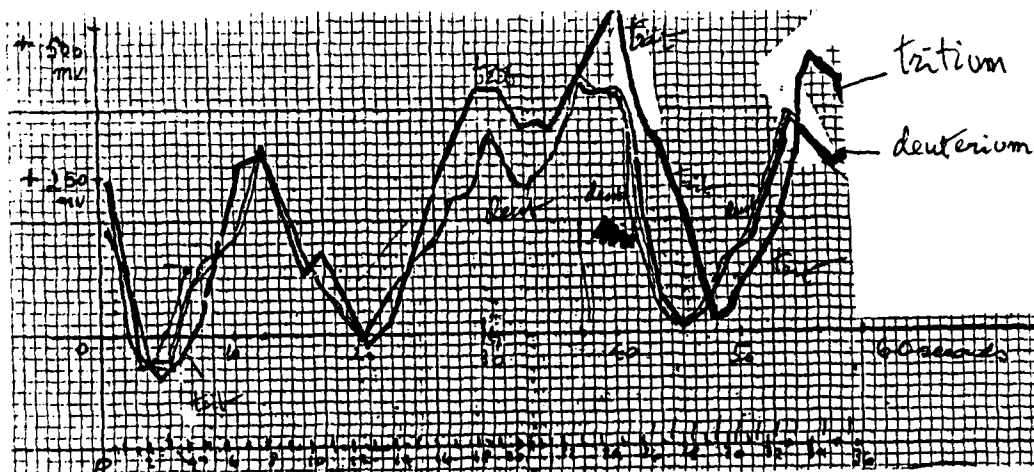
$$\text{Prob} \{ \chi^2_{35} \leq 75 \} = 0.9999$$

Consequently, the hypothesis H_0 is rejected, and we can conclude that the probability that the difference curve in Figure 2.3-1 is just noise is less than 0.01%.

To start exploring the origin of the repulsion force that we have tentatively observed, we wrapped the cylinder that houses the torsion balance with two layers

of lead sheet, each 1/8" thick. This made a major difference and the record obtained with the tritium became close to the curve recorded for the deuterium.

Figure 2.3-2 shows that the period of the torsion balance oscillation did change when going from the 10,400 integrations performed with the tritium to the same number of integrations performed with the deuterium. It is possible that the cause was the strong seasonal temperature changes in our laboratory area at TA-33, that occurred in mid-December 1988. We reported this happening to DARPA and to Prof. Weber, and we included the stabilization of the temperature of the instrumentation among the action items for the proposed 6-month extension of the contractual activity. As a provisional solution of the problem in the data, we applied a change in x-axis, by contracting numerically the period of the curve recorded with the tritium. The results are shown in Figure 2.3-3. Tables 2.3-2 and 2.3-3 give the details of the calculations. The shape of the difference curve changed radically from what we had obtained in Figure 2.3-1. It would seem that the repulsion force has disappeared. We want to stress the point that the lead sheet tests were done only once, at the very end of our stay at LANL, when the contract funds were about to be exhausted. Should the results above be confirmed by the additional measurements that we plan to carry out during next phase of data collection, we would face the need to find an explanation for the appearance and disappearance of the repulsion force, a task that is expected to be far from easy.



Notes: (a) Position of 0 mV line is arbitrary

(b) $\frac{1}{2}$ " lead shield in use

Figure 2.3-2. Plotting of Tritium Record and Deuterium Record (10,400 Integration Cycles = 173 Hours) Showing That Torsion Balance Period of Oscillation Changed From a Week to the Next, Possibly Due to Changes in Room Temperature

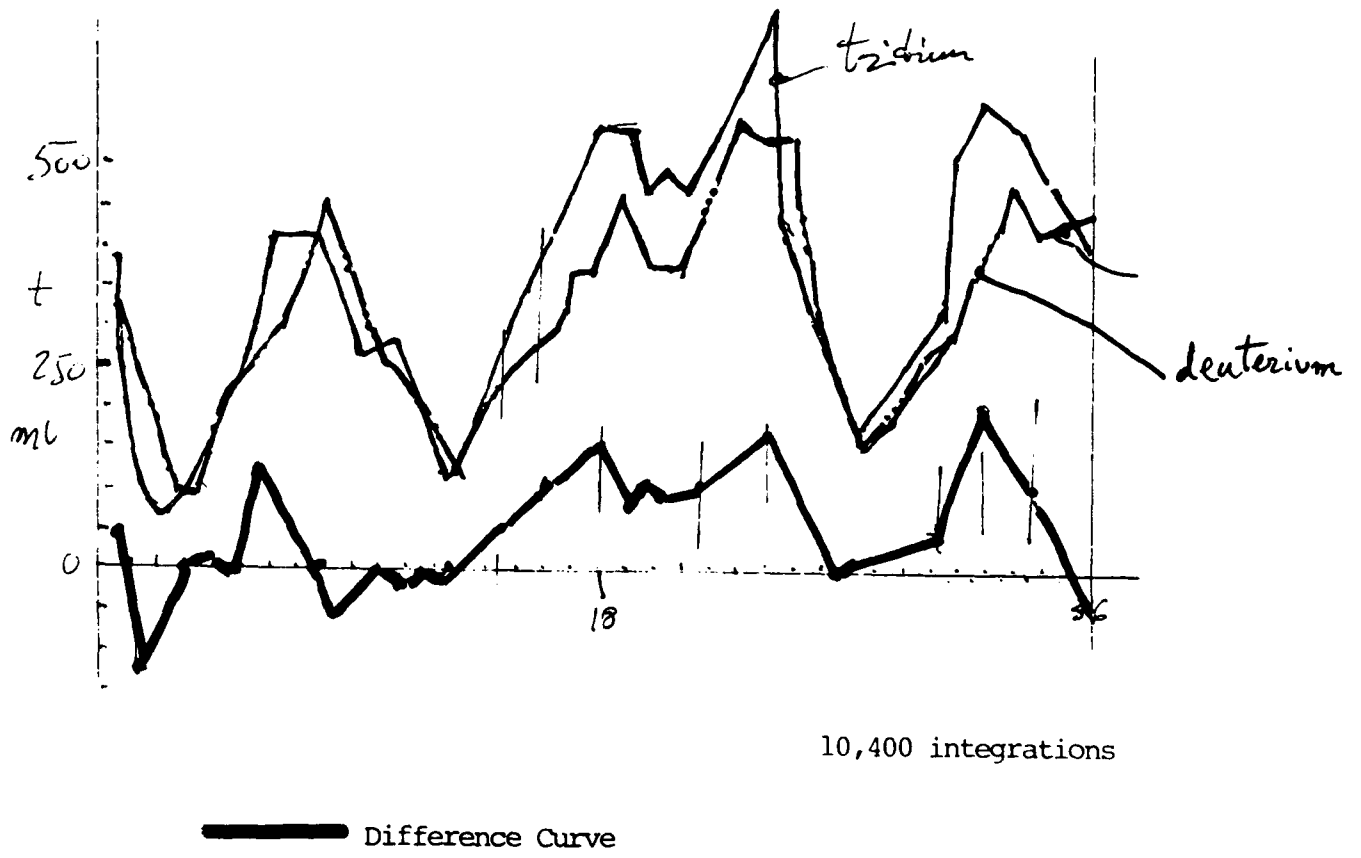


Figure 2.3-3. Plotting of Difference Curve
(|Tritium Record| - |Deuterium Record|),
When the 1/4" Lead Shield Was in Use.

Table 2.3-2. Computation of rms Value of Curve Plotted With the Tritium Source, With 1/4" Lead Shield Wrapped Around the Torsion Balance

Sample No	A (mV)	A _v	A-A _v = A	\sim^2 A	σ^2	After	Before
						σ (S + N)	Signal & Noise
1	+240	+211.	+ 28.3333	802.77776	932766.64	160. 96641 mV _{rms} (after inte- gra- tion) Processing gain=+ 40.17 dB Noise= = 0.278 $\sqrt{10400}$ = 28.35 mV Signal= 158.455 mV	Signal= 15.24 μ V
2	0	66667	-211.66667	44802.779	=		Noise= 277.97 μ V
3	- 60		-271.66667	73802.78	36		
4	- 40		-251.66667	63336.113	= 25510.		
5	0		-211.66667	44802.779	185		
6	+110		-101.66667	10336.112			
7	+270		+ 58.3333	3402.774			
8	+230		+ 18.33333	336.1111			
9	+100		-111.66667	12469.445			
10	+130		- 81.66667	6669.445			
11	+ 70		-141.66667	20069.445			
12	- 20		-231.66667	53669.446			
13	0		-211.66667	44802.779			
14	+110		-101.66667	10336.112			
15	+200		- 11.66667	136.11119			
16	+260		+ 48.3333	2336.1111			
17	+320		+108.3333	11736.11			
18	+380		+168.3333	28336.11			
19	+370		+158.3333	25069.434			
20	+360		+148.3333	22002.768			
21	+320		+108.3333	11736.11			
22	+320		+108.3333	11736.11			
23	+380		+168.3333	28336.11			
24	+430		+218.3333	47669.43			
25	+520		+308.3333	95069.442			
26	+430		+218.3333	47669.443			
27	+320		+108.3333	11736.11			
28	+260		+ 48.3333	2336.1111			
29	+140		- 71.66667	5136.1116			
30	+ 20		-191.66667	36736.112			
31	+ 60		-271.66667	73802.78			
32	+110		-101.66667	10336.112			
33	+160		- 51.66667	2669.4448			
34	+280		+ 68.3333	4669.444			
35	+440		+228.3333	52136.11			
36	+400		+108.3333	11736.11			

Table 2.3-3. Computation of rms Value of Curve Plotted With the Deuterium Source, With 1/4" Lead Shield Wrapped Around Torsion Balance

Sample No	A (mV)	A _v	A-A _v ~ = A	~ ² A	σ ²	After	Before
						σ (S + N)	Signal & Noise
1	+180	167.	+ 12.77779	163.27192	12998.456	114.01077 96641 mV _{rms} (after inte- gration)	Signal= 10.6 μV Noise= 277.97 μV (before inte- gra- tion)
2	+ 70	22222	- 97.2222	9452.1562			
3	- 40		-207.22222	42941.048			
4	0		-167.22222	27963.271			
5	+100		- 67.22222	4518.8269			
6	+120		- 47.22222	2229.9381			
7	+160		- 7.22222	52.160462			
8	+230		+ 62.77778	3941.0497			
9	+130		- 37.77777	1385.4938			
10	+ 80		- 87.22222	7607.7157			
11	+ 40		-127.22222	16185.493			
12	0		-167.22222	27963.271			
13	+ 40		- 87.22222	7607.7157			
14	+110		- 57.22222	3274.3825			
15	+130		- 37.22222	1385.4937			
16	+120		- 47.22222	2229.9381			
17	+210		+ 42.77778	1829.9385			
18	+310		+142.77778	20385.492			
19	+250		+ 82.77778	6852.1592			
20	+240		+ 72.77778	5296.605			
21	+230		+ 62.77778	3941.0497			
22	+260		+ 92.77778	8607.7165			
23	+330		+162.77778	26496.606			
24	+380		+212.77778	45274.384			
25	+380		+212.77778	45274.384			
26	+320		+152.7778	23341.05			
27	+ 90		- 77.22222	5963.2713			
28	+ 20		-147.22222	21674.382			
29	+ 10		-157.22222	24718.826			
30	+ 70		- 97.2222	9452.1562			
31	+130		- 37.22222	1385.4938			
32	+180		+ 12.77779	163.27192			
33	+250		+ 82.77779	6852.1592			
34	+320		+152.77778	23341.051			
35	+300		+132.77778	17629.939			
36	+270		+102.77778	10563.272			

Processing gain= +40.17 dB

Noise= $\sqrt{0.278 \times 10400} = 28.35$ mV

Signal= 110.43 mV

Table 2.3-4 (a)

PERCENTAGE POINTS OF THE χ^2 -DISTRIBUTION—VALUES OF χ^2 IN TERMS OF Q AND ν

ν	0.995	0.99	0.975	0.95	0.9	0.75	0.5	0.25
1	(-5) 3.92704	(-4) 1.57088	(-4) 9.82069	(-3) 3.93214	0.0157908	0.101531	0.454937	1.32330
2	(-2) 1.00251	(-2) 2.01007	(-2) 5.06356	0.102587	0.210720	0.575364	1.38629	2.77259
3	(-2) 7.17212	0.114832	0.215795	0.351846	0.584375	1.212534	2.36597	4.10835
4	0.206990	0.297110	0.484419	0.710721	1.063623	1.92255	3.35670	5.38527
5	0.411740	0.554300	0.831211	1.145476	1.61031	2.67460	4.35146	6.62568
6	0.675727	0.872085	1.237347	1.63539	2.20413	3.45460	5.34812	7.84080
7	0.989265	1.239043	1.68987	2.16735	2.83311	4.25485	6.34581	9.03715
8	1.344419	1.646482	2.17973	2.73264	3.48954	5.07064	7.34412	10.2188
9	1.734926	2.087912	2.70039	3.32511	4.16816	5.89883	8.34283	11.3887
10	2.15585	2.55821	3.24697	3.94030	4.86518	6.73720	9.34182	12.5489
11	2.60321	3.05347	3.81575	4.57481	5.57779	7.58412	10.3410	13.7007
12	3.07382	3.57056	4.40379	5.22603	6.30380	8.43842	11.3403	14.8454
13	3.56503	4.10691	5.00874	5.89186	7.04150	9.29906	12.3398	15.9839
14	4.07468	4.66043	5.62872	6.57063	7.78953	10.1653	13.3393	17.1170
15	4.60094	5.22935	6.26214	7.26094	8.54675	11.0365	14.3389	18.2451
16	5.14224	5.81221	6.90766	7.96164	9.31223	11.9122	15.3385	19.3688
17	5.69724	6.40776	7.56418	8.67176	10.0852	12.7919	16.3381	20.4887
18	6.26481	7.01491	8.23075	9.39046	10.8649	13.6753	17.3379	21.6049
19	6.84398	7.63273	8.90655	10.1170	11.6509	14.5620	18.3376	22.7178
20	7.43386	8.26040	9.59083	10.8508	12.4426	15.4518	19.3374	23.8277
21	8.03366	8.89720	10.28293	11.5913	13.2396	16.3444	20.3372	24.9348
22	8.64272	9.54249	10.9823	12.3380	14.0415	17.2396	21.3370	26.0393
23	9.26042	10.19567	11.6885	13.0905	14.8479	18.1373	22.3369	27.1413
24	9.88623	10.8564	12.4011	13.8484	15.6587	19.0372	23.3367	28.2412
25	10.5197	11.5240	13.1197	14.6114	16.4734	19.9393	24.3366	29.3389
26	11.1603	12.1981	13.8439	15.3791	17.2919	20.8434	25.3364	30.4345
27	11.8076	12.8786	14.5733	16.1513	18.1138	21.7494	26.3363	31.5284
28	12.4613	13.5648	15.3079	16.9279	18.9392	22.6572	27.3363	32.6205
29	13.1211	14.2565	16.0471	17.7083	19.7677	23.5666	28.3362	33.7109
30	13.7867	14.9535	16.7908	18.4926	20.5992	24.4776	29.3360	34.7998
40	20.7065	22.1643	24.4331	26.5093	29.0505	33.6603	39.3354	45.6160
50	27.9907	29.7067	32.3574	34.7642	37.6886	42.9421	49.3349	56.3336
60	35.5346	37.4848	40.4817	43.1879	46.4589	52.2938	59.3347	66.9814
70	43.2752	45.4418	48.7576	51.7393	55.3290	61.6983	69.3344	77.5766
80	51.1720	53.5400	57.1532	60.3915	64.2778	71.1445	79.3343	88.1303
90	59.1963	61.7541	65.6466	69.1260	73.2912	80.6247	89.3342	98.6499
100	67.3276	70.0648	74.2219	77.9295	82.3581	90.1332	99.3341	109.141
X	-2.5758	-2.3263	-1.9600	-1.6449	-1.2816	-0.6745	0.0000	0.6745

$$Q(\chi^2 | \nu) = \left[2^{\frac{\nu}{2}} \Gamma\left(\frac{\nu}{2}\right) \right]^{-1} \int_{\chi^2}^{\infty} e^{-\frac{t}{2}} t^{\frac{\nu}{2}-1} dt$$

From E. S. Pearson and H. O. Hartley (editors), Biometrika tables for statisticians, vol. I. Cambridge Univ. Press, Cambridge, England, 1954 (with permission) for $Q > 0.0005$.

Table 2.3-4 (b)

PERCENTAGE POINTS OF THE χ^2 -DISTRIBUTION—VALUES OF
 χ^2 IN TERMS OF Q AND ν

ν/Q	0.1	0.05	0.025	0.01	0.005	0.001	0.0005	0.0001
1	2.70554	3.84146	5.02389	6.63490	7.87944	10.828	12.116	15.137
2	4.60517	5.99147	7.37776	9.21034	10.5966	13.816	15.202	18.421
3	6.25139	7.81473	9.34840	11.3449	12.8381	16.266	17.730	21.108
4	7.77944	9.48773	11.1433	13.2767	14.8602	18.467	19.997	23.513
5	9.23635	11.0705	12.8325	15.0863	16.7496	20.515	22.105	25.745
6	10.6446	12.5916	14.4494	16.8119	18.5476	22.458	24.103	27.856
7	12.0170	14.0671	16.0128	18.4753	20.2777	24.322	26.018	29.877
8	13.3616	15.5073	17.5346	20.0902	21.9550	26.125	27.868	31.828
9	14.6837	16.9190	19.0228	21.6660	23.5893	27.877	29.666	33.720
10	15.9871	18.3070	20.4831	23.2093	25.1882	29.588	31.420	35.564
11	17.2750	19.6751	21.9200	24.7250	26.7569	31.264	33.137	37.367
12	18.5494	21.0261	23.3367	26.2170	28.2995	32.909	34.821	39.134
13	19.8119	22.3621	24.7356	27.6883	29.8194	34.528	36.478	40.871
14	21.0642	23.6848	26.1190	29.1413	31.3193	36.123	38.109	42.579
15	22.3072	24.9958	27.4884	30.5779	32.8013	37.697	39.719	44.263
16	23.5418	26.2962	28.8454	31.9999	34.2672	39.252	41.308	45.925
17	24.7690	27.5871	30.1910	33.4087	35.7185	40.790	42.879	47.566
18	25.9894	28.8693	31.5264	34.8053	37.1564	42.312	44.434	49.189
19	27.2036	30.1435	32.8523	36.1908	38.5822	43.820	45.973	50.796
20	28.4120	31.4104	34.1696	37.5662	39.9968	45.315	47.498	52.386
21	29.6151	32.6705	35.4789	38.9321	41.4010	46.797	49.011	53.962
22	30.8133	33.9244	36.7807	40.2894	42.7956	48.268	50.511	55.525
23	32.0069	35.1725	38.0757	41.6384	44.1813	49.728	52.000	57.075
24	33.1963	36.4151	39.3641	42.9798	45.5585	51.179	53.479	58.613
25	34.3816	37.6525	40.6465	44.3141	46.9278	52.620	54.947	60.140
26	35.5631	38.8852	41.9232	45.6417	48.2899	54.052	56.407	61.657
27	36.7412	40.1133	43.1944	46.9630	49.6449	55.476	57.858	63.164
28	37.9159	41.3372	44.4607	48.2782	50.9933	56.892	59.300	64.662
29	39.0875	42.5569	45.7222	49.5879	52.3356	58.302	60.735	66.152
30	40.2560	43.7729	46.9792	50.8922	53.6720	59.703	62.162	67.633
40	51.8050	55.7585	59.3417	63.6907	66.7659	73.402	76.095	82.062
50	63.1671	67.5048	71.4202	76.1539	79.4900	86.661	89.560	95.969
60	74.3970	79.0819	83.2976	88.3794	91.9517	99.607	102.695	109.503
70	85.5271	90.5312	95.0231	100.425	104.215	112.317	115.578	122.755
80	96.5782	101.879	106.629	112.329	116.321	124.839	128.261	135.783
90	107.565	113.145	118.136	124.116	128.299	137.208	140.782	148.027
100	118.498	124.342	129.561	135.807	140.169	149.449	153.167	161.319
X	1.2816	1.6449	1.9600	2.3263	2.5758	3.0902	3.2905	3.7190

$$Q(\chi^2|\nu) = \left[2^{\frac{\nu}{2}} \Gamma\left(\frac{\nu}{2}\right) \right]^{-1} \int_{\chi^2}^{\infty} e^{-\frac{t}{2}} t^{\frac{\nu}{2}-1} dt$$

Before resuming the experiments at LANL, during the forthcoming 6-month program extension, we must maximize the ratio "observed repulsion force"-to-"gravity gradient background". This will be done by installing the 26 replicas of the source (that LANL has constructed in the meantime) on the top of the 1 RPM rotating table.

At the same time, we must establish with suitable instrumentation (proportional counter, X-ray detector, Gamma-ray detector, neutron spectrometer, etc.) whether or not there is a measurable radiation, either electromagnetic or corpuscular, that emanates from the source.

On the basis of these measurements, we will decide whether it would be appropriate to use shields around the torsion balance, and perform series of tests, with the shields and without the shields.

3. THE CRYOGENIC FORCE SENSOR (*)

A simplified drawing of the gradiometric, 2-cell arrangement is shown in Figure 3.1. It is made of a single-block aluminum plate, with sapphire rods installed in the upper cell. The plate is attached (by means of two torsion springs that are aligned with the center of gravity) to a rigid frame that supports the condenser plates. A system of masses and springs is used to obtain the necessary attenuation of the mechanical noise. All this is placed inside a vacuum chamber, that is kept at 4.2°K inside the cryostat, suspended with three thin steel rods to the external flange.

The photographs in Figures 3.2, 3.3, and 3.4 illustrate the main components of the gradiometric force sensor. Figure 3.2 shows another version of the 2-cell assembly, that is different from the one that has been mounted in the actual sensor that we have tested. It could be used later, and the relative merits of the two versions assessed. Figure 3.3 shows the holder of the gradiometric plate, while Figure 3.4 depicts the concentric cylindrical containers that house the gradiometer inside the 4°K cryostat. The overall system is depicted in Figure 3.5, where we can see the 4°K cryostat suspended on a support tripod by means of a 2-stage vibration isolator. The sensor was mounted with no particular precautions regarding cleanliness and precision in orientation. Because of this, the gaps were kept at approximately 70 microns.

The pressure of the residual exchange gas inside the experimental chamber was too high (due to inadequacy of the pumping system) to perform measurements at 4.2k. However, the results at 77k indicate a correct working of the apparatus. The following set of data was measured:

(*) Contributed by F. Fuligni and V. Iafolla (SAO Visiting Scientists from IFSI-CNR, Frascati, Italy).

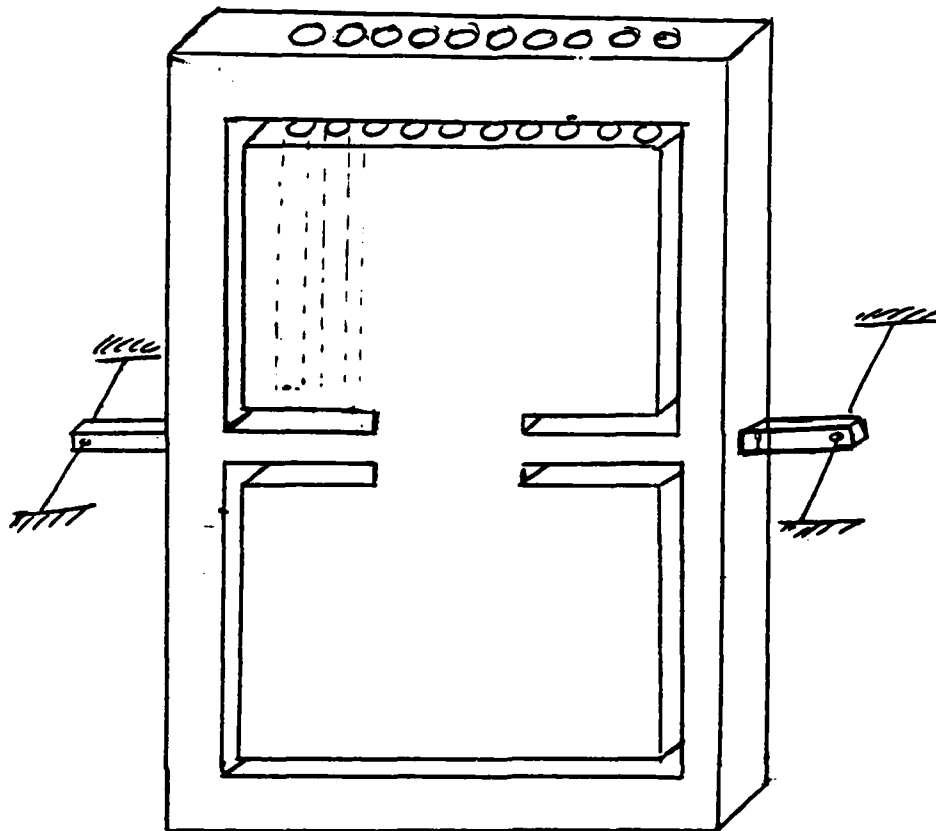


Figure 3-1. Simplified Drawing of the Gradiometric, 2-Cell Arrangement



Figure 3.2. Another Version of the 2-Cell Assembly

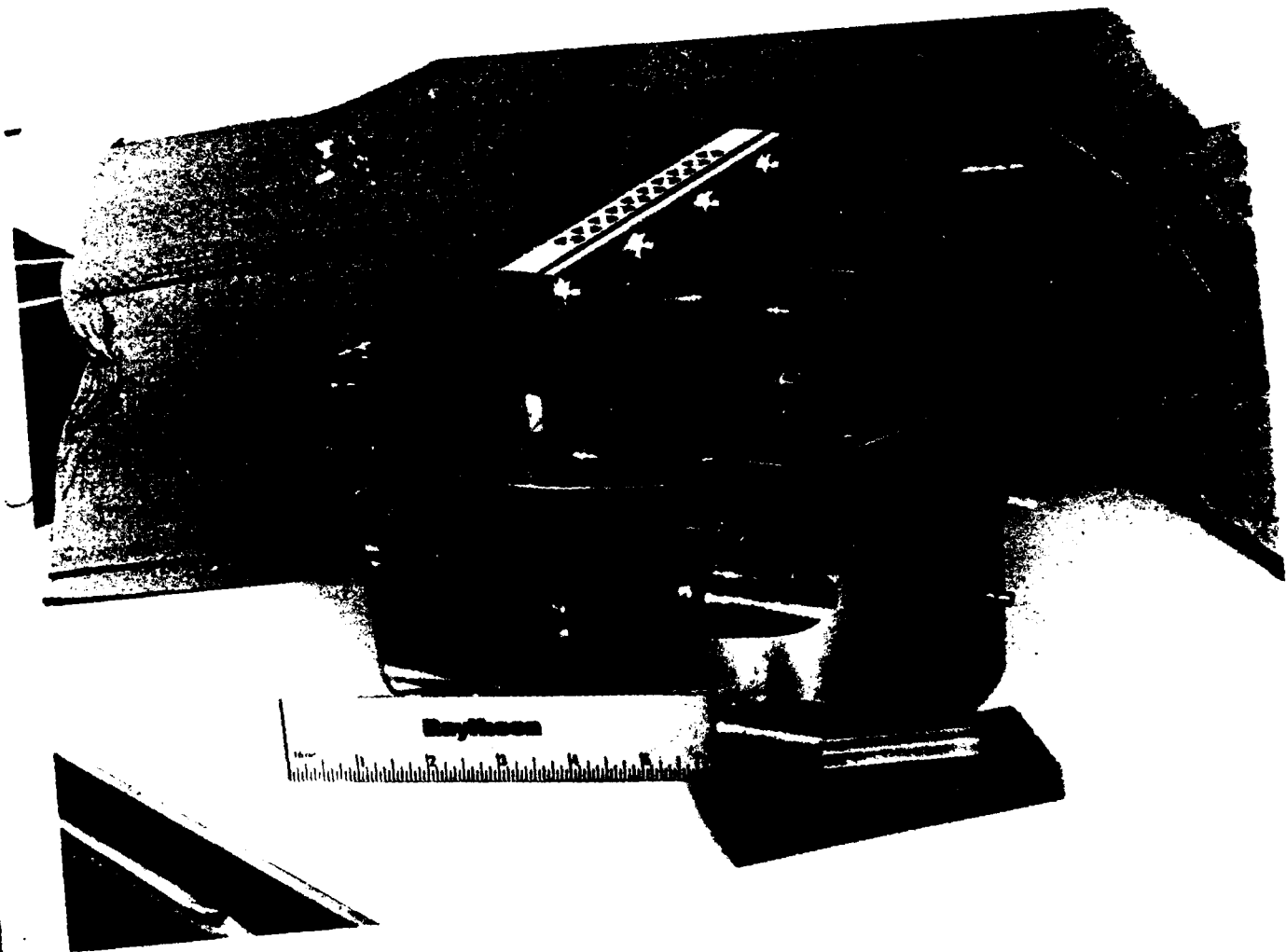


Figure 3.3. The Holder of the 2-Cell Assembly



Figure 3.4. The Cylindrical Containers That, Mounted Concentrically Inside the 4°K Cryostat, House the 2-Cell Gradiometer

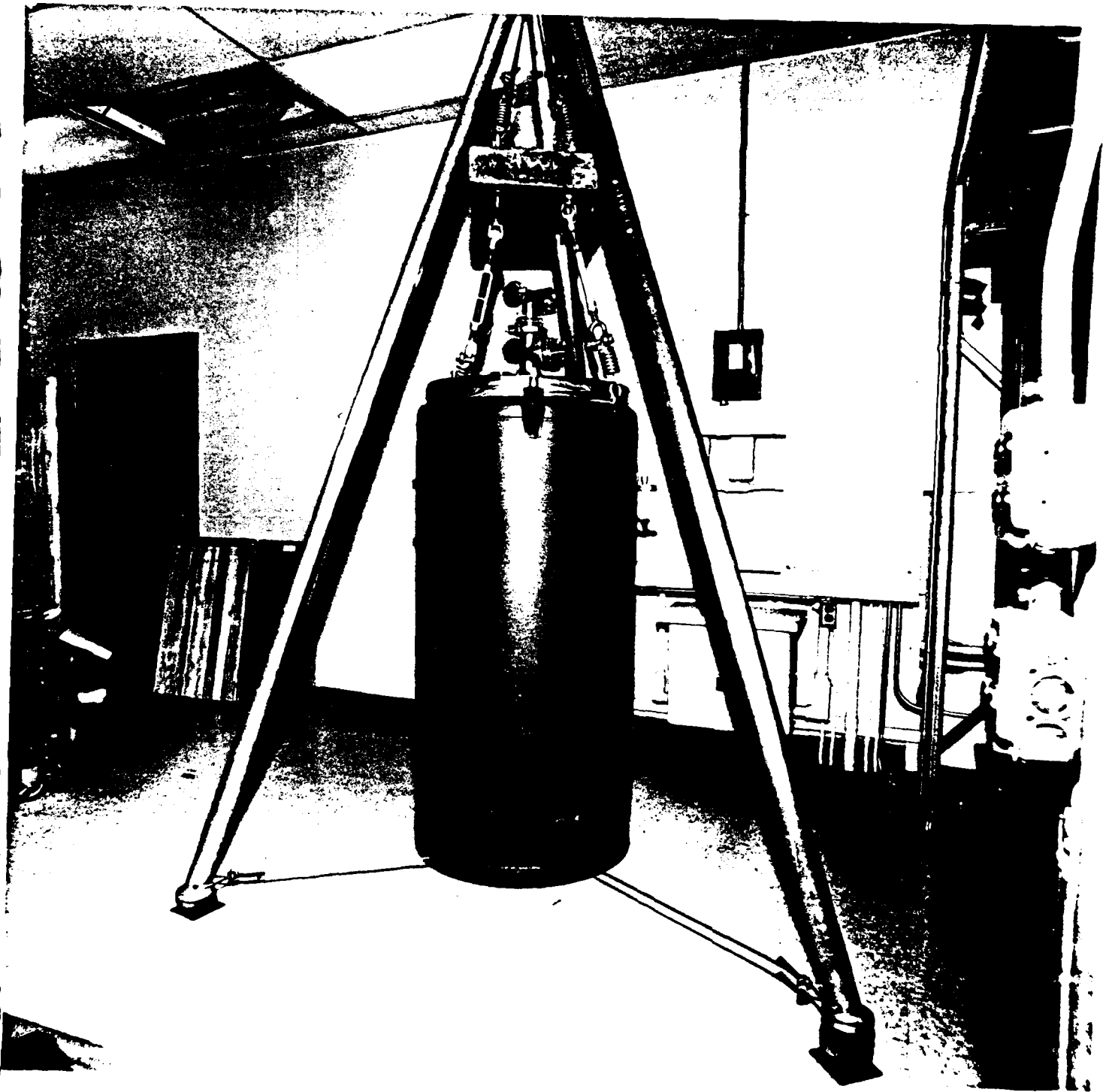


Figure 3.5 Overall View of the Cryogenic Force Sensor, with the 4 K Cryostat suspended From the Support Tripod by Means of a 2-Stage Vibration Isolator

Electric field used 4.3×10^5 V/m.

Resonant frequency of the detector $f_m = 123.500$ Hz

Mechanical quality factor $Q_m = 11,600$

In the laboratory tests performed at Raytheon, Portsmouth, RI the sensor worked as expected, actually with the Q_m exceeding the value that had been adopted as a design goal. From the parameters that were measured, we can infer a force detection sensitivity of about 8×10^{-9} dynes with 10^4 seconds integration time, at liquid nitrogen temperature. We have, in fact, the following system performance:

$$\begin{aligned} m &= 200 \text{ gr} \\ \omega &= 780 \text{ rad sec}^{-1} \\ Q_m &= 1.16 \times 10^4 \\ \Delta t &= 10^4 \text{ seconds} \\ T &= 77^\circ\text{K} \\ K &= \text{Boltzmann's Constant} = 1.38 \times 10^{-16} \text{ erg deg}^{-1} \end{aligned}$$

and, consequently:

$$\text{Minimum Detectable Force} \approx \sqrt{\frac{m \omega^4 K T}{Q_m \Delta t}} \approx 8 \times 10^{-9} \text{ dynes}$$

This corresponds to a minimum detectable force of about 10^{-9} dyne (1 nanodyne) when working at 4.2°K , with the same integration time.

A simplified block diagram of the electronics that follows the mechanical assemblies of the cryogenic force sensor is depicted in Figure 3.6, while the schematic diagram of the low-noise FET amplifier is given in Figure 3.7.

At LANL, TA-33, data acquisition will be performed at the output of the Cryogenic Force Sensor by the DIABASE Hardware/Software

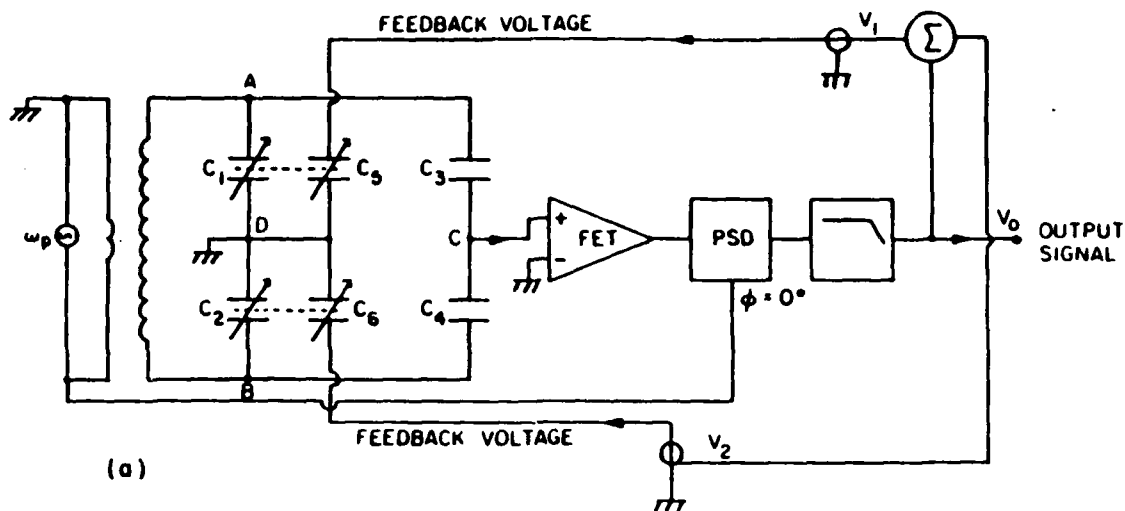


Figure 3.6. Simplified Block Diagram of the Electronics Used in the Sensor

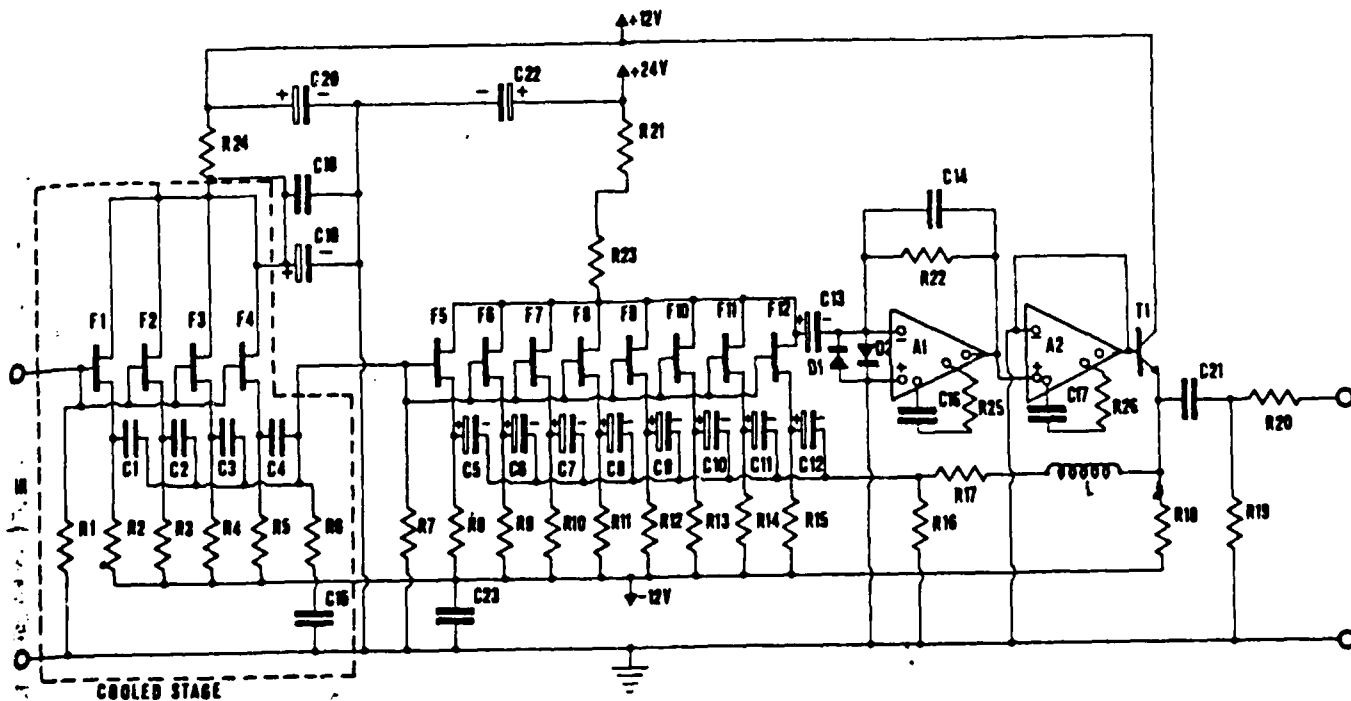


Figure 3.7. Schematic Diagram of Low-Noise FET Preamplifier (Effective Temperature: $0.2^\circ K$, When Sensing Cells are Cooled Down to $4.2^\circ K$)

approach, with the objective of measuring and plotting the spectrum of the signal (the DIABASE system has been already procured by Raytheon, and has been preliminarily tested in Portsmouth laboratories). We expect a spectrum centered at 100 Hz, with a 10^{-2} Hz width.

Hence, the requirement that the 2000 RPM rotating table have a stable velocity, within 1 part in 10^5 , and that a common oscillator drive both the rotating table servomechanism and the coherent detector at the receiving end, in order to make sure that the 100 Hz carrier generated by table rotation falls at the center of the receiver's narrow band.

The DIABASE system (see Figure 3.8) includes the following units:

- Diabase signal processing interface unit, with :
 - 8 Analog S/H input channels
 - 2 Analog output channels
 - 8 Digital I/O channels
 - 12-Bits A/D and D/A converters
- Sky Computers SKY-321-PC Digital signal processing board, with:
 - 5M bytes/sec I/O ports
 - 64 KW data memory
 - TMS 320-10 DSP
 - 4 KW program memory
- Diabase operating system layer over MS-DOS 3.2, that includes:
 - GSS-CGI user license; genhelp. exe., a program for personalized help screens; gencom. exe for default value generation; genmenu. exe for command labelling; a general function and specification help with one screen per application/function/parameter; a direction book consistent with the on line help system.

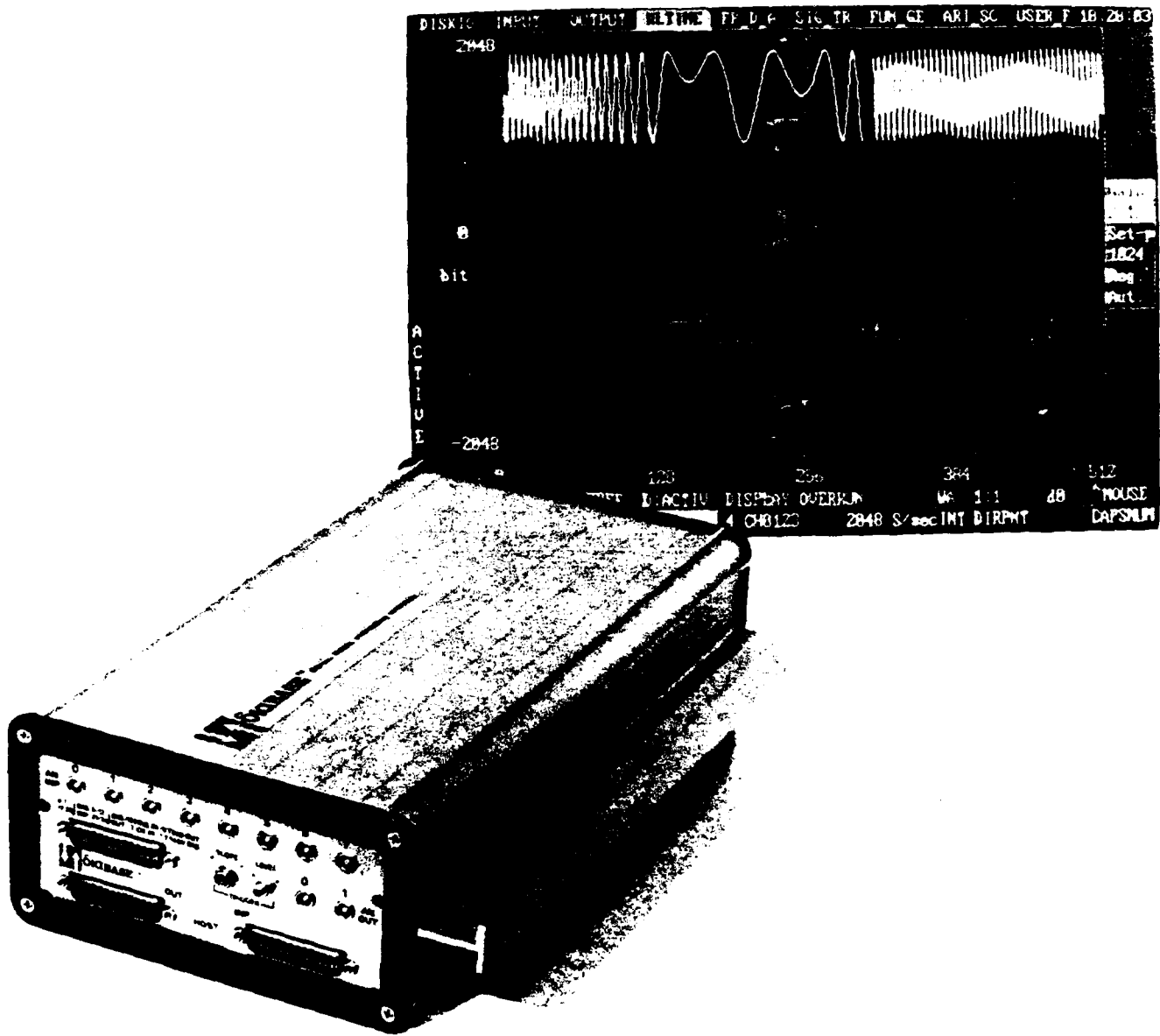


Figure 3.8. DIABASE Hardware and Output Display

NOTE:

Personal Computer compatibility: the diaBASE system works on any PC-AT bus compatible machine, up to 12 MHz, including a mathematic coprocessor 80287, an EGA or Hercules board, 2 Mbytes of extended and expanded memory (Microway Megapage or Intel Above Board); a mouse from Microsoft or Logitech. Compatible machines are Compaq 386-16/386-20 or Epson AX.

Figure 3.9 depicts an example of plot at the DIABASE output: it represents the spectrum of a signal acquired and displayed by the system.

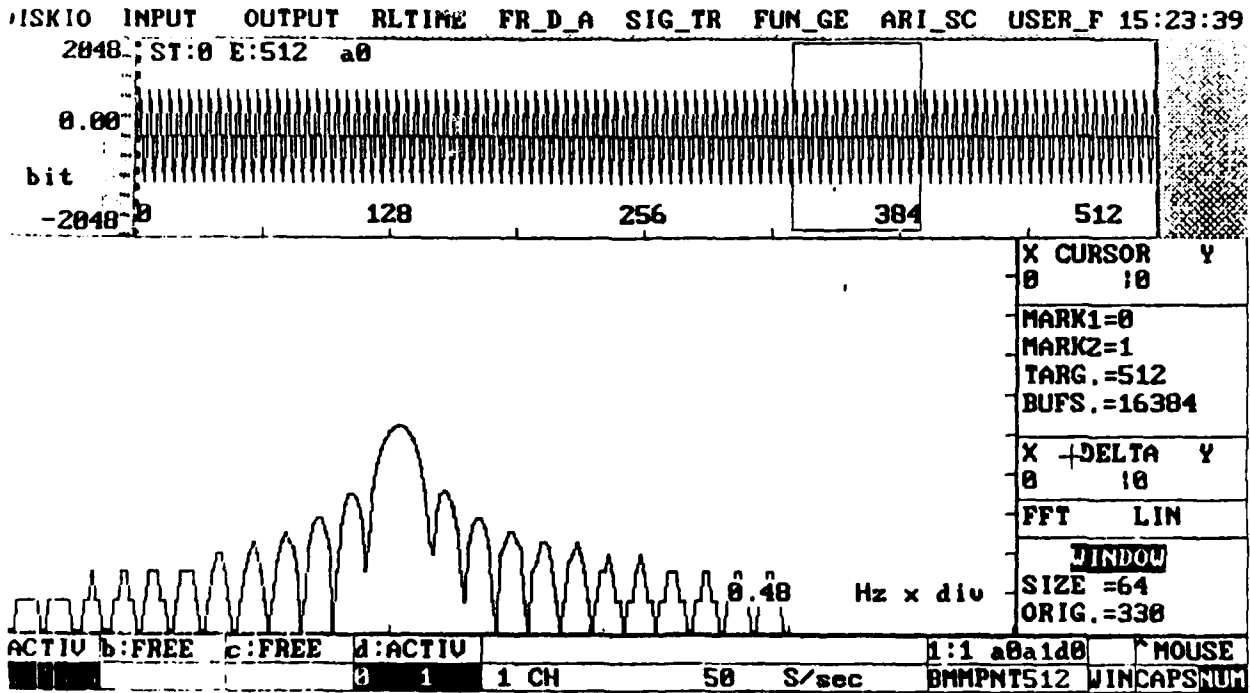


Figure 3.9. Plot of Signal Spectrum Acquired and Displayed by Diabase System

4. LABORATORY TESTS ON THE FEASIBILITY OF THE MAGNETIC INTERACTION SENSOR (*)

The SQUID system that was used in these laboratory tests is illustrated in the photograph in Figure 4.1, In the Figure, the cryostat is shown suspended from a support tripod by means of a two-stage vibration attenuator. The apparatus on the small table in the photograph, is the SQUID control unit. With this SQUID, we carried out tests on two superconducting transformers that were designed and constructed at Raytheon, Portsmouth, RI (see Figure 4.2) to explore the feasibility of effective coupling between the interaction target and the SQUID. The first was a small-diameter ferrite-core transformer (superconducting flux transformer) which was tested at liquid Helium temperature with the SQUID. The dimensions of this small toroidal core were 2.2 mm inner diameter, 4.8 mm outer diameter and 4.1 mm height. We found that there was good coupling to the SQUID in the frequency range from DC to 600 Hz. We also found that the device was quite insensitive to external mechanical and acoustical disturbances. The SQUID system noise, however, increased by a factor of 100. The primary (75 turns) had an inductance of 0.7 milliHenry and the secondary (3 turns) an inductance of about 1.2 microHenry at liquid Helium temperature (thus matching the SQUID input inductance). The primary was then loaded with a 1 Kg core stack, made of several high-permeability materials (two elementary cores of supermalloy and two cores of silectron), with several sheets of metglas, 4" wide, wrapped around the 4" column of sandwiched cores. Pick-up area with this core is about 15 cm^2 . In trying to improve on these loading conditions, the SQUID stopped operating. A possible explanation is that the magnetic core was not perfectly shielded from the outside, so that stray pick-up of e.m. interference caused the SQUID to stop operating. Should these laboratory tests resume in follow-on phases of the program, we are confident that we will determine the source of the problem and eliminate it.

(*) Contributed by D. Bramanti, SAO.

The second transformer was an air-core model, 1" diameter, primary 500 turns, inductance 10 mH; secondary 5 turns, inductance 1 microHenry. We could not test this transformer in Portsmouth. However, a similar air-core transformer has been used in the SQUID magnetometer built by IESS-CNR for CERN, Geneva, Switzerland, and it performs well.

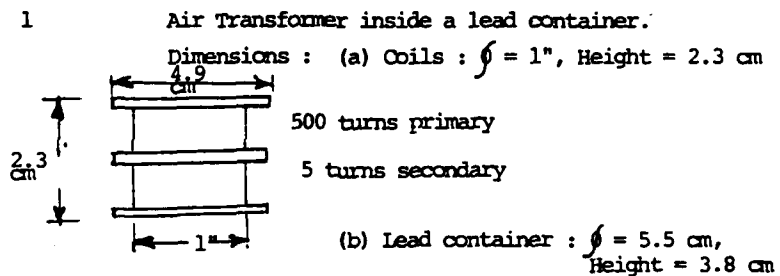
For each transformer, a lead shield was wrapped around the unit, in order to provide effective magnetic shielding (see Figure 4.2). Concerning the measurement of the highest achievable differential μ_r (on the steepest part of the hysteresis cycle), the materials that were investigated were the following:

- (1) Supermalloy, nickel-based, made by Arnold Engineering
- (2) Metglass 2605 S2 (iron-based), made by PERMAG
- (3) Metglass 2826 (nickel and iron based)
- (4) Supermagnetics, Magnetics Inc.
- (5) Conetic AA
- (6) Iron
- (7) Cryoperm 10

The best materials proved to be the first and second items above (the Supermalloy made by Arnold Engineering and the Metglass 2605 S2). For the first, the measurement of μ_r for bulk samples yielded $\mu_r = 23,000$ at room temperature and at 10 Hz (μ_r decreased to 11,000 when the sample was cooled down to liquid Helium temperature). For the second item above, the measurement of μ_r (again for bulk samples) yielded a value of 18,000 at 10 Hz and at room temperature. This value decreased to 3000, when working at 4.2°K.

For single thin strips made of material (1) and (2), μ_r was found, at room temperature, to be respectively $2.7 \cdot 10^5$ and $6.3 \cdot 10^5$. By using very thin strips (1.5 mm wide and 25 μ m thick), we measured a differential μ_r of the order of 10^6 .

<u>Quantity</u>	<u>Title of Component</u>
1	Metglass roll with coil to measure permeability
2	Coils to measure permeability of single strips
4	Toroidal cores made of various magnetic materials (2 made of supermalloy and 2 of silectron)
1	Transformer with ferrite core and lead enclosure External dimensions: (a) Transformer : 5 mm long, $\phi = 7$ mm (b) Lead enclosure: 13 mm long, $\phi = 13$ mm



1 "Copper and Lead" Container for air transformer and large core.

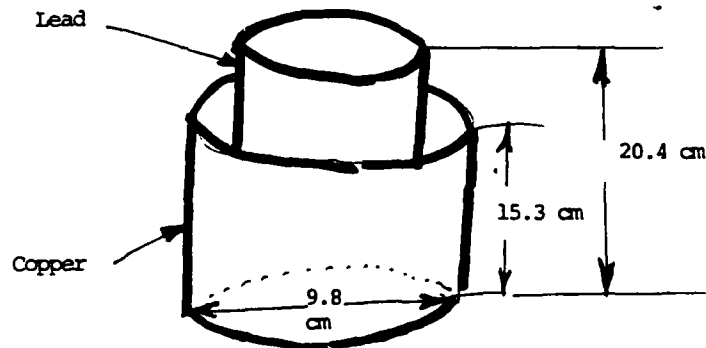


Figure 4.2. Magnetic Components Built in Order to Perform Laboratory Tests

Table 4-1 summarizes the results of the tests that we have carried out.

We can conclude that we are still far from the required performance objectives, but that some progress was achieved. In our opinion, it would be advisable to continue with a low-key, modest cost laboratory test program still using target masses of the order of one Kilogram, to decide, on more conclusive experimental evidence, whether or not to proceed to the procurement of an interim 25 Kg target and then, continue to the final target with a 250 Kg mass.

Table 4-1. Value of Parameters Affecting Feasibility of the Magnetic Interaction Sensor

Parameter	1987 JASON Estimate	1987 Estimate of Required value (Raytheon)	1989 Raytheon Measurements
Relative permeability	$\mu_r < 10^3$	$\mu_r = 10^8$	$\mu_r = 10^6$
Target collecting area	1 cm ²	10 ³ cm ²	<15 cm ²
SQUID system noise	10 ⁻⁴ ϕ_0 Hz ^{-1/2} (loaded SQUID)	10 ⁻⁷ ϕ_0 Hz ^{-1/2} (loaded SQUID)	10 ⁻⁶ ϕ_0 Hz ^{-1/2} (unloaded SQUID)

5. CONCLUSIONS AND RECOMMENDATIONS

The project has attempted to provide an answer to the question that, in the course of our contractual activity, became a first priority issue: did Prof. Weber see radiation pressure from low-energy neutrinos in his experiments at University of Maryland with a room-temperature torsion balance, characterized by a threshold sensitivity of a few microdynes? At the time of this report, we do not yet have a conclusive answer. However, we expect that following the proposed added scope, 6-month contract, we can provide firm conclusions.

The measurements that we have carried out at LANL with the torsion balance have been performed only once: they must be repeated several times, before they can be considered probative evidence. In addition, there were several flaws in the functioning of the torsion balance and the data collection system. These must be removed before resuming the measurements. With these caveats, we can say, most tentatively, that: (a) a repulsion force appears to be present when experimenting with the tritium, using the observations made with the deuterium as reference (the intensity of this force is a few microdynes, in agreement with the observations made by Prof. Weber at U. of Maryland); (b) the above repulsion force seems to disappear when a 1/4" lead shield is wrapped around the torsion balance. The most urgent task of the proposed added-scope activity is to verify these tentative results, using the present instrumentation. If these tentative results are verified, we should proceed to the planned instrumentation improvement.

The most advisable first step in this instrumentation improvement program is to increase the Signal-to-Noise and Signal-to-Background ratios. The unwanted background signals are due to gravity gradient effects caused by the mass of tritium source, and these can be strongly reduced by mounting replicas of the source (26 of them will fill the available space) all around the rim of the rotating table.

Under a direct contract from DARPA, LANL has already fabricated these 26 replicas. Mounted on the table, we expect that the Signal-to-Background ratio will be improved by a factor of 500-to-1000. There is also the possibility of decreasing the noise at the input of the data acquisition chain, by a factor larger than 5. Once the signal of concern (repulsion force) is clearly visible above noise and above background, it will be easier to rigorously investigate the possible shielding effect of lead sheets, gold-coated mylar, etc., wrapped around the torsion balance cylinder.

Additionally, we should install a thermal control to stabilize the temperature of the torsion balance, and change the circuits of the electronic damper to achieve critical damping.

Another recommendation is that DARPA provide support for a 1-year follow-on to fund Raytheon to test the cryogenic force sensor at LANL. This instrument has already been constructed by Raytheon and initially tested in Portsmouth, RI without tritium sources. However, it cannot be tested at LANL with tritium sources, until a 2000 RPM rotating table is available. The construction of this table (its function is to modulate the neutrino flux at 100 Hz) has already been included in Raytheon's 1-year follow-on effort proposal. As an alternative, should the added-scope effort provide experimental proof of the correctness of Prof. Weber's theory of an abnormally large cross-section in the interaction neutrino/crystal, we could use Weber's rotating shutter as a cheaper and simpler alternative to the rotating table. The cost of this shutter has also been included in the Raytheon proposal. Finally, a separate, low-key, two-year effort should be funded to answer conclusively the three basic JASON questions on the feasibility of the magnetic interaction sensor.

6. BIBLIOGRAPHIC REFERENCES

1. Raytheon Co., 1987 a, First Quarterly Report, Contract F49620-87-C-0050, 15 August.
2. Raytheon Co., 1987 b, Second Quarterly Report, Contract as above, 16 November
3. Raytheon Co., 1988 a, Third Quarterly Report, Contract as above, 15 February.
4. Raytheon Co., 1988 b, Fourth Quarterly Report, Contract as above, 15 May.
5. Raytheon Co., 1988 c, Fifth Quarterly Report, Contract as above, 15 August.

APPENDIX A

ON THE SCATTERING OF X-RAYS AND NEUTRINOS IN CRYSTALS:
A COMPARATIVE THEORETICAL STUDY

by

Robert R. Lewis
Department of Physics
University of Michigan
Ann Arbor, MI 48109

23 January 1989

ON THE SCATTERING OF X-RAYS AND NEUTRINOS IN CRYSTALS:
A COMPARATIVE THEORETICAL STUDY

by

Robert R. Lewis
Department of Physics
University of Michigan
Ann Arbor MI 48109

unpublished preprint

January 23 1989

ABSTRACT

We compare the theory of the scattering of X-rays and neutrinos in crystals, in order to understand the current controversy about Weber's work on "abnormally large coherent cross sections" for neutrinos. A calculable standard model is defined, describing scattering from an ideal cubic lattice. Its limitations then are discussed, including the roles of multiple scattering and crystal imperfections, both for neutrinos and X-rays. Since these corrections can be made negligible for neutrinos, the predictions of the standard model should be accurate. We find no abnormalities in the scattering of neutrinos: the net force on a crystal should be proportional to the number of atoms and should be unmeasurably small. A crucial experimental test of Weber's theory of "abnormal coherent scattering" is proposed.

Introduction

My subject is the recent work of Prof J. Weber on the elastic scattering of neutrinos in single crystals. His published results are therefore required reading for the comprehension of this article. He has reported on experiments [1] in which neutrinos from a tritium source (and from a reactor and from the sun) are claimed to exert a measurable force ($F \approx 1 \mu\text{dyne}$) on a single crystal of sapphire, mounted in a room temperature torsion balance. The torsion balance is calibrated by comparison with the gravitational attraction with a dummy source of 27 grams of lead.

He has also published a theory of "abnormal coherent scattering" of neutrinos from crystals [2], which concludes that the total cross section for the entire crystal is

$$\sigma_{\text{total}} = [(\pi^2/3) - 1] \frac{G_F^2 E_\nu^2}{4\pi\hbar^4 c^4} [N_T - Z_T(1-4\sin^2\theta_w)]^2 \quad (1)$$

where N_T and Z_T are the total number of neutrons and protons in the crystal, G_F is the Fermi constant, θ_w is the Weinberg angle and E_ν is the neutrino energy. A cross section proportional to the square of the total number of atoms in the crystal would be enormously enhanced relative to the cross section for a non-crystalline target, which is proportional to the total number of atoms. The claimed proportionality to the square of the number of target atoms is offered as the explanation of the abnormally large scattering cross sections reported in the experiments.

If correct, this is an enormously significant result! To appreciate this, one can simply compare the scale of Weber's "table-top" detector, with another neutrino detector such as Kamiokande. Weber's target is a crystal of mass about 10 grams; Kamiokande has an active target mass of about 2 billion grams. If Weber's claims were correct, his neutrino detector would radically alter the problem of detecting low energy neutrinos. However, there is a lot of scepticism about his experimental results [3], and it is important that they be independently verified.

The purpose of this paper, however, is not to discuss his experiments but to consider the theory for "abnormal coherent scattering" proposed by Weber. Numerous critical comments about his theory have already been published [4]. In order to assess the theoretical work of Weber, I have re-examined the simple model of an "ideal crystal", and many corrections to it. The technique used to carry out this analysis is a comparative one, starting with the conventional theory of X-ray scattering [5] in crystals and then making the modifications appropriate to neutrino scattering. This permits me to rely on well-established results for the Bragg scattering of X-rays, a thoroughly understood subject [6,7]. My work is more pedagogical than creative; I have tried to give a clear exposition of the physics rather than to present new results.

The theory of neutrino scattering can be developed in parallel with that of X-ray scattering, to emphasize their similarities. The first step is to express both calculations in a similar formalism, using for each the quantum theory of single particle scattering. Next I derive some simple formulas for the scattering amplitudes from individual atoms and from an ideal crystal. Various corrections are then discussed, especially multiple scattering and mosaic lattice imperfections. The role of scattering of long wavelengths away from the Bragg peaks is considered, as well as the earlier controversy initiated by Raman about the coherence of X-ray scattering in crystals. Finally, we close with a summary of the dependence of the scattering on the number of atoms, and with some suggestions about ways of checking the assertions made by Weber.

Formalism

There are both similarities and differences between X-rays and neutrinos. While the wave properties of X-rays and the particle properties of neutrinos are usually emphasized, both can be considered as quantum particles with similar behavior. X-rays are massless particles travelling at the speed c ; neutrinos may have a very small mass and travel at speeds very close to c . X-rays scatter from charged particles via electromagnetic interactions, while neutrinos scatter from both charged and neutral particles via weak interactions. Both radiations interact via short-range processes, and are very penetrating. Among the differences between these particles are their spins and statistics (X-rays are spin 1 bosons and neutrinos spin 1/2 fermions) and their discrete symmetries (X-rays preserve C and P but neutrinos do not). Despite these differences, we can draw a close analogy in their elastic scattering. The details of the process by which they scatter are unimportant to our discussion, which is concerned primarily with the extensive properties of the scattering, not its intensive properties. We will suppress the role of the scattering amplitude from a single atom, which appears as a multiplicative factor in most formulas, and emphasize the many body effects in scattering from a macroscopic crystal.

One would like to make this comparison using a similar formalism for both particles. Most of neutrino physics is expressed in the language of particle physics, since one must frequently deal with the annihilation of a neutrino and the creation of other leptons. On the other hand, most of the physics of X-rays has been based on classical Maxwell theory. We can bridge this gap by using the same formalism for both particles: scattering theory of a single particle wave equation. The justification for this lies in the negligible contribution of absorptive processes for both X-rays and neutrinos in condensed matter. The dominant process for both particles is elastic scattering; the crystal behaves like a transparent diffracting medium which preserves the number of both X-rays and neutrinos.

To further simplify the discussion of X-ray scattering, we will suppress their polarization properties. These factors complicate the discussion, but do not significantly change the results. Therefore we will treat X-rays as *spinless* particles satisfying the scalar wave (Helmholtz) equation

$$-\frac{\partial^2 \phi}{c^2 \partial t^2} + \nabla^2 \phi = 0 \quad (\text{X2})$$

in place of Maxwell's equations. Since we are interested primarily in the results for neutrino scattering, this simplification of X-ray scattering is innocuous.

For the neutrino, we will use the Weyl equation for a massless two component particle

$$i\hbar \frac{\partial \psi}{\partial t} - i\hbar c \vec{\sigma} \cdot \vec{\nabla} \psi = 0 \quad (\nu 2)$$

In both cases we are interested in the positive frequency plane wave solutions incident on the crystal,

$$\phi, \psi \propto e^{+i\vec{k} \cdot \vec{x} - i\omega t}$$

Equation ($\nu 2$) implies that the neutrino has negative helicity,

$$\vec{\sigma} \cdot \hat{k} \psi = -\psi$$

Notice that here and in the remainder of this document we will label equations and figures pertaining to X-rays with an (X), and those for neutrinos with an (ν). Equations which pertain to both will have no such label.

Both wave equations are modified in the crystal by a short range interaction with each atom, which we also take as having zero spin. Since both electromagnetic and weak interactions are weak enough to be treated as perturbations, the scattering can be described by an effective central potential of appropriate strength and radial dependence, chosen to give the correct

amplitude in first order. The wave equations inside the crystal become, for the X-ray

$$-\frac{\partial^2 \phi}{c^2 \partial t^2} + \nabla^2 \phi + \sum_{j=1}^N V_X(\vec{x}-\vec{x}_j) \phi = 0 \quad (X3)$$

and for the neutrino

$$i\hbar \frac{\partial \psi}{\partial t} - i\hbar c \vec{\sigma} \cdot \vec{\nabla} \psi + \sum_{j=1}^N V_\nu(\vec{x}-\vec{x}_j) \psi = 0 \quad (\nu 3)$$

Here N is the total number of atoms, which are assumed to be arranged in a three dimensional lattice with sites x_j . The form of the effective potentials will be discussed next.

Scattering Amplitudes for Atoms

X-rays scatter from atoms principally via the absorption and re-emission of the X-ray by the electron cloud. At frequencies below the threshold for pair formation ($\omega \ll m$), the scattering amplitude for an individual electron is just the Compton amplitude ($e^2/mc^2 \approx 10^{-13}$ cm). For an atom in its ground state, the scattering amplitude is given by the coherent sum of amplitudes from the electrons, weighted by a phase factor

$$f_{x,e} = (e^2/mc^2) \int d^3x e^{i\vec{q} \cdot \vec{x}} \rho(x) = (e^2/mc^2) \bar{\rho}(q) \quad (X4)$$

where ρ is the number density of electrons in the atom and where $\vec{q} = \vec{k}_i - \vec{k}_f$ is the momentum transfer. There is negligible energy transfer and the X-ray undergoes elastic scattering from the atom. The scattering amplitude is proportional to the quantity $\bar{\rho}(q)$, called the structure factor of the atom, defined as

$$\bar{\rho}(q) = \int d^3x e^{i\vec{q} \cdot \vec{x}} \rho(x)$$

This result shows the full coherence of the scattering for long wavelengths: for $qa_0 \ll 1$ the structure factor is approximately Z , the total number of electrons. For larger momentum transfers, the structure factor decreases toward zero.

The X-ray scattering from the nuclear charge is like that from a particle of charge Ze and mass AM and therefore has amplitude $(Z^2m/AM)(e^2/mc^2)$, which is smaller than the scattering amplitude from a single electron by a factor smaller than 1%. We neglect this amplitude.

The range of the interaction with each electron is of order $(\hbar/mc) \approx 10^{-11}$ cm, which is much less than the size of the atom, so that the X-ray "sees" each electron as it is locally distributed in the atom. We can replace the interaction with an "effective potential" whose shape and strength are adjusted so that the scattering amplitude is correctly given by the Born approximation. This substitution correctly treats the wave function everywhere outside the atom and is therefore adequate to describe macroscopic effects such as the re-scattering of the X-ray by another atom in a crystal. Examination of equation (X3) shows that we can choose the strength and radial form to be

$$V_x(r) = 4\pi (e^2/mc^2) \rho(r) \quad (X5)$$

This amplitude is real and contributes only to the real part of the refractive index for X-rays. There are also imaginary terms coming from photoionization and photoexcitation of the atoms, which lead to absorption of the X-ray. The cross sections for these processes contain absorption edges, and are strongly dependent on the X-ray energy. However, they are typically of about the same magnitude as the cross section for Compton scattering from a single electron, $\sigma_c = 8\pi(e^2/mc^2)/3 \approx 10^{-24}$ cm². This leads to an absorption length of order $\ell = (n\sigma)^{-1} \approx 10$ cm, in condensed matter.

For neutrinos, the mechanism for elastic scattering is the exchange of a heavy neutral boson Z_0 with each of the particles in the atom. This amplitude is also coherent, with each particle in the atom contributing according to its "weak charge". The scattering amplitude from the nucleus is

$$f_{\nu,n} = G_F [N - Z (1 - 4\sin^2\theta_w)] (E_\nu/\hbar^2c^2) \langle k_f | k_i \rangle \quad (V4)$$

where N , Z are the neutron and proton numbers of the atom, and $|\kappa\rangle$ is the two component spinor for the neutrino. The scattering amplitude from the electron cloud is

$$f_{\nu,e} = - G_F [1 + 4\sin^2\theta_w] (E_\nu/\hbar^2 c^2) \langle \kappa_f | \kappa_i \rangle \bar{\rho}(q) \quad (\nu 4')$$

These two amplitudes add to give the scattering amplitude of the whole atom

$$f_\nu = f_{\nu,n} + f_{\nu,e}$$

The dimensional factor $G_F E_\nu / (\hbar c)^2$ gives a weak scattering amplitude of order $2 \cdot 10^{-24}$ cm for 10 keV neutrinos. The factor $\langle \kappa_f | \kappa_i \rangle$ gives some angular dependence to both terms, causing the back scattering amplitude to vanish. The structure factor of the electron distribution gives an even stronger angular dependence to f_e . This amplitude can also be derived from an effective potential, whose final form consists of a short range part describing the nuclear contribution and a longer range part for the electron cloud,

$$V_\nu(\vec{r}) = 2\pi G_F \{ [N - Z(1-4\sin^2\theta_w)] \delta(\vec{r}) - [1 + 4\sin^2\theta_w] \rho(r) \} \quad (\nu 5)$$

Therefore, the interaction of both X-rays and neutrinos in condensed matter can be described by effective central potentials of similar form but very different strength. This completes our discussion of the formalism needed for calculation of the scattering of X-rays and neutrinos. Subsequent derivations will be based on the techniques of scattering theory for such wave equations, especially including perturbation theory.

Single Scattering from an Ideal Crystal

The simplest model for the scattering of X-rays from a crystal is to treat the atoms as fixed at points on a rigid lattice with no imperfections. The lattice is therefore assumed to have no vibrational motion; only the X-rays play a dynamical role. The calculation of the scattering is reduced to solving the wave equation [Eq. (X²)] for this lattice. We call this the "ideal crystal" model. An approximate scattering amplitude in this model can be found using first order perturbation theory, with a plane wave X-ray incident on the crystal. Multiple scattering of the X-rays is not included by this approximation, which provides a starting point for the later discussion of multiple scattering and thermal effects.

The scattering amplitude for the whole crystal is

$$f(\mathbf{q}) = (e^2/mc^2) \bar{\rho}_j(\mathbf{q}) \sum_{j=1}^N e^{i\mathbf{q} \cdot \mathbf{x}_j} \quad (6)$$

where the \mathbf{x}_j are the lattice vectors. This result is frequently written down as the starting point of a calculation of scattering from a crystal; we have indicated the steps in deriving it from our formalism, either for X-rays or for neutrinos. We note that the extensive variable giving the size of the crystal is the number of terms N in this summation; this is the only extensive variable in the derivation which follows. We must carefully follow this variable through the subsequent derivation, since the dependence on N is the crux of the controversy over Weber's theory.

We must add amplitudes from each point in the lattice before squaring to form the scattering cross section. This gives the crucial property of coherence between amplitudes from different unit cells. If the phases of the individual amplitudes are the same for every cell, they add arithmetically for the whole crystal, giving the Bragg peaks with a total scattering amplitude proportional to the number of cells N and a cross section

proportional to N^2 . Inspection of Eq. (5) shows that this maximal coherence occurs when the scalar (Laue) equations are satisfied

$$\vec{q} \cdot \vec{a}_1 = 2\pi H_1 \quad \vec{q} \cdot \vec{a}_2 = 2\pi H_2 \quad \vec{q} \cdot \vec{a}_3 = 2\pi H_3 \quad (7)$$

Here the vectors $\vec{a}_1, \vec{a}_2, \vec{a}_3$ are the edges of the unit cell of the lattice, and H_1, H_2, H_3 are integers. We can invert these three equations to obtain a single vector (Bragg) equation

$$\vec{k}_f - \vec{k}_i = \vec{K}_j \quad (8)$$

where \vec{K}_j is a reciprocal lattice vector. This condition can be visualized by construction of the "Ewald sphere", which has radius $|k_i| = |k_f|$ and its center shifted by an amount \vec{K}_j from the origin of the reciprocal lattice. The origin of the reciprocal lattice therefore lies on the sphere; the Bragg equation is satisfied whenever another reciprocal lattice point also intersects the sphere. This occurs only for special values of the outgoing wavevector: Equation 7 represents three separate conditions which must be met.

The example of a cubic lattice with spacing b can be evaluated explicitly. The reciprocal lattice is also cubic, with spacing $2\pi/b$. The Laue equations become

$$q_x b = 2\pi H_1 \quad q_y b = 2\pi H_2 \quad q_z b = 2\pi H_3 \quad (9)$$

which gives us the Cartesian components of \vec{q} . For this model, the series in Eq. 5 is a geometric series which can be factorized and summed, giving an explicit formula for the differential cross section

$$d\sigma/d\Omega = (e^2/mc^2)^2 |\bar{\rho}(\mathbf{q})|^2 \left[\frac{\sin(q_x N_x b/2)}{\sin(q_x b/2)} \frac{\sin(q_y N_y b/2)}{\sin(q_y b/2)} \frac{\sin(q_z N_z b/2)}{\sin(q_z b/2)} \right]^2$$

Here N_j is the number of cells in the j^{th} direction; the total number of cells is $N = N_x N_y N_z$. This cross section must be integrated over the directions of k_f and averaged over a broad spectrum, weighted by the spectral density $F(k_i)$ of the source

$$\sigma_{\text{average}} = \int d^3k_i F(k_i) \int d^3k_f (d\sigma/d\Omega) \delta(k_i - k_f) \quad (10)$$

The extensive variables N_x , N_y , N_z appear only in the form

$$\left[\frac{\sin(qNb/2)}{\sin(qb/2)} \right]$$

which has sharp peaks when the Laue equations are satisfied. The peak cross section is

$$(d\sigma/d\Omega)_{\text{max}} = (e^2/mc^2)^2 |\bar{\rho}(q)|^2 N^2 \quad (11)$$

and the width is

$$\Delta q_x = (2\pi/N_x b) \quad \Delta q_y = (2\pi/N_y b) \quad \Delta q_z = (2\pi/N_z b) \quad (12)$$

The volume in reciprocal space occupied by each peak $\Delta q_x \Delta q_y \Delta q_z$ is proportional to N^{-1} . Since the width of the peaks is much less than the distance between reciprocal lattice vectors, they can be replaced by Dirac delta functions, with integrated intensity proportional to N ,

$$\left[\frac{\sin(q_x N_x b/2)}{\sin(q_x b/2)} \right]^2 \Delta q_x \cong N_x \left(\frac{2\pi}{b} \right) \delta(q_x - K_x) dq_x \quad (13)$$

The result for σ_{average} , integrated over one Bragg peak, is

$$\sigma_{\text{av}} = N \left(\frac{2\pi}{b} \right)^3 (e^2/mc^2)^2 \int d^3k_i F(k_i) \int d^3k_f |\bar{\rho}(q)|^2 \delta(k_i - k_f) \delta(\vec{q} - \vec{K})$$

Changing variables in the second integral $k_f = q + k_i$ and carrying out the integration over \vec{q} , we obtain

$$\sigma_{\text{av}} = N \left(\frac{2\pi}{b} \right)^3 (e^2/mc^2)^2 \int d^3k_i F(k_i) |\bar{\rho}(K)|^2 \delta(k_i - |\vec{K} + \vec{K}_i|) \quad (14)$$

which is our final formula, showing the explicit dependence on the extensive variable N . The same formula is readily seen to apply to X-rays in crystals with other space lattices. It also pertains to neutrino scattering; only the multiplicative factors in the scattering amplitude must be changed. The location and shape of the peaks is the same as for X-rays.

The derivation above is consistent with results given in standard textbooks, such as Landau-Lifschitz [8]. They show that the peak cross section is proportional to N^2 , but that this exponent is reduced by any subsequent averaging. The maxima correspond to momentum transfers which are localized at specific points in three dimensional reciprocal space. The width in each dimension is of order $\Delta k \approx (2\pi/b)N^{-1/3}$ and so each successive integration lowers the exponent by 1/3. For example, in section 97 they show that averaging over the *direction* of the outgoing photon but keeping the frequency fixed leads to a cross section proportional to $N^{4/3}$. In section 98 they give three different ways of averaging over momentum transfers, appropriate to different ways of observing Bragg scattering in the laboratory, each leading to cross sections proportional to N , given in Equations (98.5), (98.6) and (98.8).

Role of Multiple Scattering

Since the scattering cross sections of X-rays from light atoms are of order 10^{-23} cm², their mean free path in condensed matter is of order 1 cm. The single scattering approximation is thus a very good one for non-crystalline targets, which are usually "optically thin". This is also true for scattering in crystals except at the Bragg peaks. Because of the coherence of scattering at the Bragg peaks, the effect of multiple scattering becomes significant in quite small crystals. Near a Bragg peak, the incident wave does not remain unperturbed as in single scattering, but is attenuated exponentially as the wave enters the crystal; this is referred to as the "extinction" of the incident wave.

This effect is contained in the "dynamical theory" of X-ray scattering, which does not refer to the lattice dynamics but to the inclusion of the interference between incident and scattered waves. In scattering theory, extinction results from the conservation of probability or "unitarity". It obviously reduces the amplitude of the incident wave and the resultant scattering near the Bragg peaks. The extinction length l , which comes from

multiple elastic scattering and is related to the real part of the refractive index, is not to be confused with the "absorption length", which results from inelastic scattering and is related to the imaginary part of the index. If the effect of extinction is included, the intensity of the Bragg peaks will no longer be proportional to N^2 , but will be reduced by an amount which depends both on N and l .

The simplest model which estimates the extinction length is that of Darwin [9], in which the crystal is represented by lattice planes (not points). Assuming the atoms to be uniformly distributed over the scattering planes, Darwin showed that the scattering from each plane would have a strong maximum in the direction of specular reflection; interference between the planes would be constructive when the Laue condition is met. This model adequately describes the scattering near any single isolated Bragg peak, in terms of the appropriate set of lattice planes. The calculation of extinction in this model requires solving a set of finite difference equations relating the incident and reflected wave amplitudes at each plane.

The Darwin model is exactly solvable and gives an explicit formula for the extinction length, in terms of the atomic scattering amplitudes in the forward direction and in the direction of the Bragg peak. His estimate of the extinction length l for X-rays is

$$l_x = 1/(n\lambda f_x) \cong 1/(10^{+23-8-11}) = 10^{-4} \text{ cm} \quad (\text{X15})$$

where n is the number density of atoms, λ is the X-ray wavelength and f_x is a typical scattering amplitude. Several innocuous factors depending on the direction and polarization of the X-rays have been dropped for simplicity. The proportionality to the scattering amplitude, rather than the scattering cross section is characteristic of coherent scattering. Numerically, this result implies extinction lengths smaller than most crystals, which makes it difficult to calculate the absolute intensity of the Bragg peaks.

For neutrinos, the same formula implies an extinction length

$$l_{\nu} = 1/(n\lambda f_{\nu}) \approx 1/(10^{+23-8-24}) = 10^{+9} \text{ cm} \quad (\nu 15)$$

near a Bragg peak. Although this is much less than the mean free path for incoherent scattering, it is much larger than the size of a crystal, implying that extinction is negligible for neutrinos. This estimate of extinction is *independent* of the neutrino energy, since both f_{ν} and $1/\lambda$ are proportional to the neutrino energy. The extinction length in a crystal is similar to (but not the same as!) the "coherence length" in a homogeneous medium, the distance in which the phase reverses [10].

Mosaic Lattice

In practice, natural crystals rarely have perfect symmetry but are flawed by a mosaic structure, with small micro-crystals joined at boundaries in such a way that the crystal planes are not perfectly flat. The random orientation of the planes will clearly add to the angular width of the Bragg peaks. In a small enough crystal, this broadening would reduce the intensity of the peaks. However, in most crystals, there is a compensation between the effects of extinction and the effects of mosaic structure. The mosaic structure breaks up the crystal into small portions within which there is coherence and extinction; the scattering from different micro-crystals is incoherent. If the micro-crystals are smaller than the extinction length, then the mosaic structure will reduce the overall attenuation of the incident wave and enhance the intensity of the Bragg peaks. It becomes a very difficult job to calculate the intensity of the Bragg peaks; the results depend on the relative size of the extinction length and the size of the micro-crystals. One would not expect to observe an N^2 law for the scattering from most crystals.

For laboratory purposes, it is now possible to obtain strain-free crystals which exhibit coherence over dimensions as

large as a few centimeters. Thus the effects of mosaic structure could be eliminated and this complication removed. Clearly this should be done in any laboratory tests of the radiation pressure of neutrinos [11].

Non-Bragg Scattering of Long Wavelengths

Since there is a lower limit to the spectrum of reciprocal lattice vectors, X-rays or neutrinos of sufficiently low energy cannot satisfy the Bragg equation. The smallest reciprocal lattice vector in sapphire, corresponding to the longest length in the unit cell ($b = 13 \cdot 10^{-8}$ cm), is $K_0 = 2\pi/b = 4.8 \cdot 10^{+7}$ cm⁻¹. The corresponding lower limit for Bragg scattering is

$$k \geq K_0/2 = 2.4 \cdot 10^{+7} \text{ cm}^{-1} \quad \text{or} \quad hkc \geq 480 \text{ eV}$$

The diffraction of X-rays or neutrinos with energies below this limit is not concentrated in peaks; the crystal behaves instead like a homogeneous refracting medium. The propagation of visible light in crystals is an example of this behavior.

Could Weber's results come entirely from this low energy portion of the spectrum, with the increased coherence of longer wavelength particles somehow compensating their smaller numbers? The following derivation shows that this is not the case. For wavelengths longer than the target, the scattered intensity would be proportional to the square of the number of target atoms; but there is a negligible number of neutrinos with λ greater than a few centimeters. For wavelengths shorter than the target dimensions, but longer than the unit cell, we can divide the target into "coherence volumes", which we define as cubes with edge λ . For number density ρ , each coherence volume contains $\rho\lambda^3$ atoms and has a cross section proportional to the square of this number

$$\sigma_a = 4\pi Z^2 (e^2/mc^2)^2 \quad \sigma_{cv} = \sigma_a \rho^2 \lambda^6 \quad (\text{X16})$$

The number of such coherence volumes in a target volume V is V/λ^3 . Since the scattering amplitudes from different coherence volumes

are incoherent, the cross section for the entire target is

$$\sigma_{\text{target}} = \sigma_{\text{cv}} V/\lambda^3 = \sigma_a \rho^2 V \lambda^3 \quad (17)$$

where σ_a is the cross section per atom. This shows that, like the Bragg scattering at shorter wavelengths, the cross section for longer wavelengths is proportional to the target volume or the total number of target atoms, $N = \rho V$, not to their square.

Equation 9 also gives the explicit dependence on the wavelength. For X-rays, the structure factor for these wavelengths is a constant and the cross section per atom is independent of the wavelength. Thus the intensity scattered from the target is proportional to λ^3 , and the rate of momentum transfer is proportional to λ^2 . From Eq. (17), we find for X-rays,

$$\sigma_{\text{target}} = 4\pi (e^2/mc^2)^2 Z^2 N \rho \lambda^3 \quad (\text{X18})$$

This formula shows explicitly the full coherence within each atom ($\sigma \propto Z^2$), and the incoherence of the target ($\sigma \propto N$). It also shows an enhancement of the force exerted by longer wavelength X-rays due to this coherence: X-rays of longer wavelengths exert greater radiation pressure.

For neutrinos, the atomic cross section is proportional to λ^{-2}

$$\sigma_a = 2\pi (G_F/\hbar c \lambda)^2 [N-2Z]^2 \quad (\nu 16)$$

and so Equation 17 gives instead,

$$\sigma_{\text{target}} = 2\pi (G_F/\hbar c)^2 \rho \lambda N \quad (\nu 18)$$

Multiplying by the momentum per neutrino, $p = h/\lambda$, gives a force which is independent of λ . The longer wavelength neutrinos have smaller cross section per atom and carry less momentum, but have larger coherence volume; these two effects balance. A neutrino force sensor simply counts the number of neutrinos, without regard to their wavelength or energy. This conclusion pertains to any

distribution of neutrinos with wavelengths between about 10^{-7} cm and 1 cm . This includes the "relic neutrinos" from the big bang, whose wavelengths are in the millimeter range; similar conclusions have already been published [12].

We can make this calculation more quantitative for the Weber experiments. The distribution of neutrinos from tritium beta decay is given by the phase space density

$$dN \propto p^2 dp q^2 dq \delta(T_e + T_\nu - Q)$$

Here p is the electron momentum and q the neutrino momentum. These variables are related to the energy release $Q = 18.6$ keV by energy conservation. Their kinetic energies are (with $c \rightarrow 1$ for convenience), $T_e = p^2/2m$ and $T_\nu = q$ and so $p = \sqrt{2m(Q - q)}$. The spectrum becomes

$$dN \propto \sqrt{Q-q} q^2 dq.$$

This can be normalized by calculating the integrated spectrum

$$N = \int_0^Q q^2 dq \sqrt{Q-q} = 16 Q^{7/2}/105$$

Hence the momentum spectrum of the neutrinos, normalized to unity, is

$$dN/N = 105 z^2 \sqrt{1-z} dz/16$$

where $z \equiv q/Q$. For example, the fraction of neutrinos below $q = 480$ eV ($z = .026$) is

$$\int_0^{480} dN/N \approx (105/48) z^3 \Big|_0^{.026} \approx 4 \cdot 10^{-5}$$

This is a negligible fraction of the number of neutrinos and, by our reasoning above, a negligible fraction of the total force due to neutrinos. Thus, the long wavelength neutrinos do not play a significant role in exerting radiation pressure.

Raman Controversy

This same controversy about "abnormal coherent scattering" has occurred before, in the literature on X-ray scattering. This completes the analogy between X-ray and neutrino scattering! The subject came up in several papers published by Sir C. V. Raman in the 1940's, in which he argued that the scattering of X-rays should give intensities proportional to the *square* of the number of atoms [13]. This is essentially the same point of view as Weber's. Raman was concerned with the inelastic scattering of X-rays, in which optical phonons were excited. He insisted that this scattering, like the elastic scattering, would give Bragg peaks whose intensities were proportional to N^2 , whereas scattering with the excitation of acoustic phonons would give a background proportional to N . It seemed (to Raman) that experiment bore this out. His theoretical argument was answered by Zachariasen [14], who insisted that while the peak intensity should be proportional to N^2 , the integrated intensity under each Bragg peak should be proportional to N .

In retrospect, it is not clear to me whether Raman was considering the *peak* scattering intensity or the *integrated* intensity. His theory dealt with the intensity in a particular direction; his experiments dealt with integrated intensities. The controversy was only a small part of a larger struggle to understand the vibration spectrum of crystals in general and the X-ray diffraction of diamonds in particular. Some of the trouble was due to dissolved impurities in the diamonds he used, giving extra Bragg peaks.

Raman felt that the optical modes could be considered as a single N -fold degenerate mode, altering the coherence properties of inelastic scattering. Born and von Karman had published a theory which gave a continuous spectrum with $3N$ independent modes. One thing that was missing in the 1940's was an understanding of the "van Hove singularities" in the density of phonon states: singularities occur from the piling up of a large number of modes with similar frequencies, and can resemble the effect of a single

highly degenerate mode [15]. The other missing element was an independent method of determining the phonon spectrum. We now know from neutron scattering that Born was closer to the truth than Raman: the spectrum is continuous and the different phonons behave independently. As shown by Zachariasen, the inelastic scattering from N independent atoms has integrated intensity proportional to N , not to N^2 , just as for elastic (Bragg-Laue) scattering.

One can ask why there was no definitive experimental test of this basic point in the 1940's. At first glance, it would appear easy to resolve the controversy by changing N : a two-fold increase in the crystal size should give a four-fold increase in the integrated intensity of each peak, according to Raman; Zachariasen would predict a two-fold increase. As our discussion has shown, the situation for X-rays is not that simple: one must also consider the extinction of the incident wave and the effect of mosaic structure, both of which alter the intensity as the size is changed. Since extinction begins for crystals of about micron size, it would have been difficult to eliminate extinction by using small samples. The mosaic structure of lattice imperfections was also beyond control. We are not aware of any direct experiment to settle the questions raised by Raman & Zachariasen.

Summary: Dependence on N

We can finally summarize the dependence of the integrated scattering cross section from a crystal on the number of atoms, N , as follows. If we hold the shape and all other variables fixed, changing only the number of atoms, there are three different regimes, for small, intermediate and large N . For N small enough, the size of the target is less than the wavelength and there is complete coherence between the amplitudes from each elementary particle. In this limit the scattering cross section grows like N^2 . For kilovolt X-rays and neutrinos, this regime is confined to

targets of at most a few atoms, and so the cross section is quadratic in the number of constituents within the atoms or molecules of the target.

In the intermediate regime, the integrated scattering cross section continues to grow like N , just as it would for an amorphous solid. The differential cross section shows sharp Bragg peaks, but the integral under these peaks is linear in N . This growth continues until extinction of the incident particle sets in and multiple scattering becomes dominant. In this large N limit, the scattering becomes a surface property of the target, not a bulk property, and the cross section grows only like the surface area or $N^{2/3}$. The onset of this regime is determined by the strength of the interaction and occurs much sooner for X-rays than for neutrinos. We have seen that for X-rays in the vicinity of a Bragg peak, this regime sets in for crystals of millimeter size; for neutrinos this regime is only reached for targets larger than the earth! Throughout the range of interest, neutrino cross sections for crystals of macroscopic size should be proportional to the volume of the crystal.

The force exerted on a crystal by a flux of 10 keV neutrinos can be estimated by multiplying the flux J by the cross section per atom ($\sigma_a \approx 2 \cdot 10^{-45} \text{ cm}^2$), the average momentum transfer per collision ($q_z \approx 7 \text{ keV}$) and the number of atoms per gram ($N/A \approx 0.8 \cdot 10^{22}$). This gives the contribution of a single Bragg peak, and must be further multiplied by the number of Bragg peaks. This can be crudely estimated by counting the number of peaks within the average volume of the "Ewald sphere"; for a 10 keV neutrino in sapphire, this gives

$$\text{number of peaks} \approx 4\pi k^3/3 \cdot [b/2\pi]^3 = (kb)^3/6\pi^2 \approx 4600.$$

Our estimate of the net force is

$$\text{Force} \approx 3 \cdot 10^{-38} J M \text{ dynes} \approx 4 \cdot 10^{-25} \text{ dynes} \quad (19)$$

where J is the neutrino flux $(\text{cm}^2\text{-sec})^{-1}$, and M is the target

mass (gm). Under the conditions of Weber's experiments $J \approx 10^{+12}$ and $M = 13$, the force is predicted to be roughly 19 orders of magnitude smaller than the result reported by Weber! The discrepancy between this estimate and Weber's is of course just the extra factor N , which we assert should not be included in the theoretical result. Our prediction is far below the sensitivity of any existing mechanical sensor.

What Should be Done?

A sensor with sufficient sensitivity to detect neutrinos will respond to many other weak forces, such as air currents, magnetic forces, infrared and X-radiation. The false signals due to many such "systematic corrections" must be eliminated before one can attribute the signal to neutrinos. But how can one finally demonstrate that the sensor is responding to the coherent scattering of neutrinos in the crystal?

It should be much easier to settle the Weber controversy than the Raman controversy by varying the crystal size. Changing the target size is a standard test of coherence which has been successfully carried out, for example, in the "coherent regeneration" of neutral kaons in matter [16]. This effect was proven experimentally to exhibit an N^2 law by removing half of the target and watching the intensity decrease by four.

Since the extinction length of neutrinos is much larger than the crystal size, multiple scattering can be neglected. Strain free crystals as large as several centimeters can be made with current technology. It should therefore be straightforward to compare directly the force exerted on crystals of different size. One cannot hope to prove the validity of the conventional theory since the force is too small to measure, to say nothing of measuring its dependence on N . However, this approach can demonstrate the invalidity of Weber's theory. Since the quoted cross section is comparable to the geometrical size of the target, Weber's explanation must involve some extinction of the incident

wave. Therefore, one should not expect an N^2 increase in the net force for larger crystals, but it should be possible to measure the force on smaller crystals. This would require an increase in the signal to noise ratio for the experiment, which can be achieved by reducing the noise from gravity gradients [17].

Acknowledgements

This work was carried out as part of a project devoted the scattering of neutrinos in crystals, in collaboration with D. Bramanti, F. Fuligni and M. D. Grossi. The work was sponsored by U. S. Department of Defense Advance Research Projects Agency and by Raytheon Company. I am particularly grateful to Mario Grossi for his stimulating discussions of the ideas and the experiments.

Bibliography

1. J. Weber, Phys. Rev. D38, 32 (1988).
2. J. Weber, Found. Phys 14, 1185 (1984);
J. Weber, Phys. Rev. C31, 1468 (1985).
3. T. H. Ho, Phys. Lett. 168B 295 (1986); G. F. Bertsch and Sam M. Austin, Phys. Rev. C34 361 (1986).
4. R. Casella, Nuovo Cimento 94A 42 (1986); M. N. Butler, unpublished Caltech preprint, July 1986; H. J. Lipkin, Phys. Rev. Lett. 58 1176 (1987); Y. Aharonov, F. T. Avignone, A. Casher and S. Nussinov, Phys. Rev. Lett. 58 1173 (1987); G. T. Trammell and J. P. Hannon, Phys. Rev. Lett. 61 653 (1988).
5. The comparison with thermal neutron scattering is much less direct, due to the low velocity of the neutron. The time of flight of a thermal neutron past an atom is of order $\tau \approx 10^{-13}$ sec, which is much more than typical periods of atomic motions $T \approx 10^{-15}$ sec. This implies that significant energy transfers take place. For X-ray scattering, the transit time τ is of order 10^{-18} sec, much less than atomic periods, and the energy transfer is negligible.
6. W. H. Zachariasen, "Theory of X-Ray Diffraction in Crystals", John Wiley (1945).
7. A. H. Compton and S. K. Allison, "X-rays in Theory and Experiment", van Nostrand (1935).
8. L. D. Landau and E. M. Lifshitz, "Electrodynamics of Continuous Media", Addison-Wesley NY (1960); Chapter 15.
9. C. G. Darwin Phil. Mag. 27, 325 & 675 (1914); see also ref. 7 pages 376-380.

10. L. Wolfenstein, Phys. Rev. D17, 2369 (1978).
11. Weber says nothing about imperfections in his crystals.
12. V. F. Schvartsman et al, JETP Lett. 36, 277 (1982).
13. C. V. Raman, Proc. Ind. Acad. Sci., 14 317 (1941). This reference is incorrectly cited by Zachariasen, in a footnote to page 199 of reference 6. This required a lot of added work in sorting through the many papers of Raman, which had its own rewards.
14. reference 6, page 199-200.
15. L. van Hove, Phys. Rev. 89, 1189 (1953).
16. J. H. Christenson, et al, Phys. Rev. 140, B74 (1965).
17. private communication M. D. Grossi.

ADDENDUM TO APPENDIX A

Added Comments on the original Report (Appendix A)

by

Robert R. Lewis
Department of Physics
University of Michigan
Ann Arbor MI 48109

June 1 1989

ABSTRACT

Some minor omissions are corrected, and a key number (the mean number of Bragg peaks) is recalculated more carefully.

Added comments on the original report (Appendix A):

1. (A-5) The formalism used to describe neutrinos requires some further explanation. The neutrino mass is assumed zero throughout the report, and only two components are included in the analysis: left handed particles and right handed antiparticles. These two states are singled out by the operator $\hat{\sigma}$ which specifies the direction of the neutrino spin. If we choose eigenstates of the spin relative to the neutrino momentum \vec{k} , then $\hat{\sigma} \cdot \vec{k}$ negative corresponds to the left-handed particle and $\hat{\sigma} \cdot \vec{k}$ positive corresponds to the right-handed antiparticle. Thus, the quantities $\hat{\sigma}$ are matrices of the usual Pauli form, and they describe the spin of the neutrino. At the same time, since the helicity and the energy are correlated for massless particles, the quantity $\hat{\sigma} \cdot \vec{k}$ labels the particle/antiparticle nature of the neutrino.

2. (A-6) In equations (X-3) and (ν -3), the symbols V_x and V_ν stand for the mean potential energy of the X-ray or neutrino inside matter. The inclusion of these terms results in a change of the wavenumber of the particles inside matter, resulting from scattering, as expected from the index of refraction. The mean potential energy is an average of the interaction energy of the particle with each of the atoms in the sample. For our purposes, it is sufficient to assume that these mean potentials are constants inside the sample and zero outside, and do not depend on the position of the particle. However, the potentials, especially in the case of neutrinos, can depend on the spin of the particle.

3. (A-10) The "Ewald sphere" construction is a standard graphical representation of the solution of the Bragg equation (8)

$$k_f - k_i = k_j$$

which defines the location of the Bragg peaks. Here \vec{k}_f , \vec{k}_i stand for the outgoing and incoming neutrino wavevectors, and \vec{R}_j is one of the reciprocal lattice vectors, normal to the lattice planes. Since the scattering is elastic, the magnitudes $|\vec{k}_f|$ and $|\vec{k}_i|$ are equal. The direction and magnitude of \vec{R}_j is set by the orientation and spacing of the crystal lattice.

If we draw a lattice in reciprocal space, choosing any lattice point O as origin, then the vectors \vec{R}_j go from the origin O to the lattice points; see attached Figure 1. We can visualize a solution of eq (8) by drawing a sphere of radius $|\vec{k}_i|$ passing through the origin, with center at P. This "Ewald sphere" has a radius and orientation determined by the incident neutrino. The wavevector of the outgoing neutrino must also lie on the same sphere. If a second lattice point also touches the sphere, then the Bragg equation is satisfied, and a strong peak occurs in the scattering. One can visualize other peaks which occur as the orientation of the crystal, or the length and direction of the neutrinos is changed. The same figure is useful in counting the total number of Bragg peaks which occur as one integrates over all incident and outgoing neutrinos.

4. (A-19) Why was the "Raman controversy" not settled by experiments with the radiation pressure of X-rays? I couldn't find in the literature any *experimental* proof that Zachariasen was correct ($F \propto N$) and Raman wrong ($F \propto N^2$). There are numerous mathematical "proofs" that the radiation pressure of X-rays is proportional to N , but no direct experimental observation of this basic point. The most important reason for this is role of extinction, which is neglected in these theoretical calculations. In fact, X-rays are strongly attenuated in perfect crystals in the vicinity of a Bragg peak, with attenuation lengths of order 0.1 mm or less, depending on the size and quality of the crystal. An experiment to demonstrate the dependence on N , without large corrections for extinction, would require several very thin samples, and the absolute measurement of very weak forces.

It was obviously thought to be too difficult to settle this point in the 1940's; it is probably seen as unnecessary to do this in the 1990's.

5. (A-20) We estimated the average number of Bragg peaks in the scattering of a beam of neutrinos by simply multiplying the volume of the Ewald sphere by the density of points in the reciprocal lattice. This is the same technique used by Weber [J. Weber, Phys. Rev. C31, 1469 (1985); equation 15.]. It is based on the crude assumption of an *isotropic* beam of *mono-energetic* neutrinos of the same average energy as the actual beam. It gave a large number of Bragg peaks

$$N \approx [\langle k \rangle b]^3 / 6\pi^2 = 4600$$

The large value of this number reflects the large value of the mean neutrino wavenumber and the large size of the unit cell of sapphire. Clearly, a better estimate would require a more detailed description of the distribution of energies and angles in the beam.

In the actual experiment, the angular spread of the incident beam defined by a target of area 200 cm^2 at distance 12.2 cm from the source, giving a solid angle of about $\Delta\Omega = [200/4\pi(12.2)^2] = 0.11 \text{ radian}^2$, which is considerably smaller than $4\pi = 12.57 \text{ radian}^2$. The angular spread is the same for all neutrino energies. The energy spread of the neutrino beam is given by the shape of the allowed spectrum

$$dn = dq q^2 \sqrt{Q-q}$$

where q is the neutrino energy and $Q = 18.6 \text{ keV}$ is the kinetic energy release for tritium decay. This distribution is shown in Figure 2, divided into six energy groups each of width $\Delta q = 3.1 \text{ keV}$. This distribution can easily be integrated, and the fractional number in each group evaluated:

$$f_i = [0.010, 0.061, 0.145, 0.239, 0.304, 0.242]$$

The average energy in each group is

$$\langle q \rangle_i = [1.55, 4.65, 7.75, 10.85, 13.95, 17.05] \text{ keV}$$

We can now re-calculate the number of Bragg peaks by repeating the previous estimate, which is based on one energy group, using instead six separate groups. If we rotate the Ewald sphere for each of the groups relative to the reciprocal lattice (or vice-versa!) through the solid angle $\Delta\Omega = 0.11 \text{ rad}^2$, we must estimate the additional volume of reciprocal space swept out. A graphical construction shows that the additional volume is about 0.89 of the volume of the sphere, $[4\pi\langle q \rangle_i^3/3]$. This volume is then multiplied by the density of points in the reciprocal lattice, which is $[b/2\pi]^3 \cong 8.86 \cdot 10^{-24} \text{ cm}^3$ for sapphire. The resultant product is the number of Bragg peaks for each of the groups, which must be weighted by the fraction of the beam in that group. The final result is

$$\begin{aligned} N &= \sum_i f_i (0.89) [4\pi\langle q \rangle_i^3/3] [b/2\pi]^3 \\ &= (0.2 + 26 + 281 + 1616 + 3565 + 5182) \\ &= 10,670 \end{aligned}$$

We therefore *increase* our previous estimate by a factor of about 2.3. Examination of the individual groups shows that the higher energy groups dominate, and were *underestimated* previously. Figure 2 shows that the energy distribution is skewed to higher energy, and that the mean value of q^3 (which is relevant to the number of Bragg peaks) is considerably higher than $(10 \text{ keV})^3$.

One can also use this estimate to provide some "theoretical error bars" on the validity of either estimate. The six group estimate shows that our original estimate was only valid to within a factor of about 2. Increasing the number of groups could reduce the error bars further. In fact, it is not difficult to do the energy integral analytically, obtaining

$$N = (0.89) [b/2\pi]^3 [4\pi\langle q^3 \rangle/3] = 0.0057 (Qb)^3 = 10,365$$

This shows that our "six-group" calculation was accurate to 3% !

6. (A-23) The first page of the bibliography was inadvertently dropped from the published report. A copy is enclosed.

7. (A-20) It is of interest to compare our estimate of the net force exerted by neutrinos with other published estimates. While there are many discussions of the dependence of the force on N , all concluding that the force is proportional to N , not N^2 , I find only one reference which gives a numerical result:

Y. Aharonov et al, Phys. Rev. Lett. 58, 1173 (1987)

They find an *upper limit*

$$F < 3 \cdot 10^{-10} \text{ dyne}$$

which is compatible with my estimate (based on the revised number of Bragg peaks)

$$F \cong 0.9 \cdot 10^{-24} \text{ dyne}$$

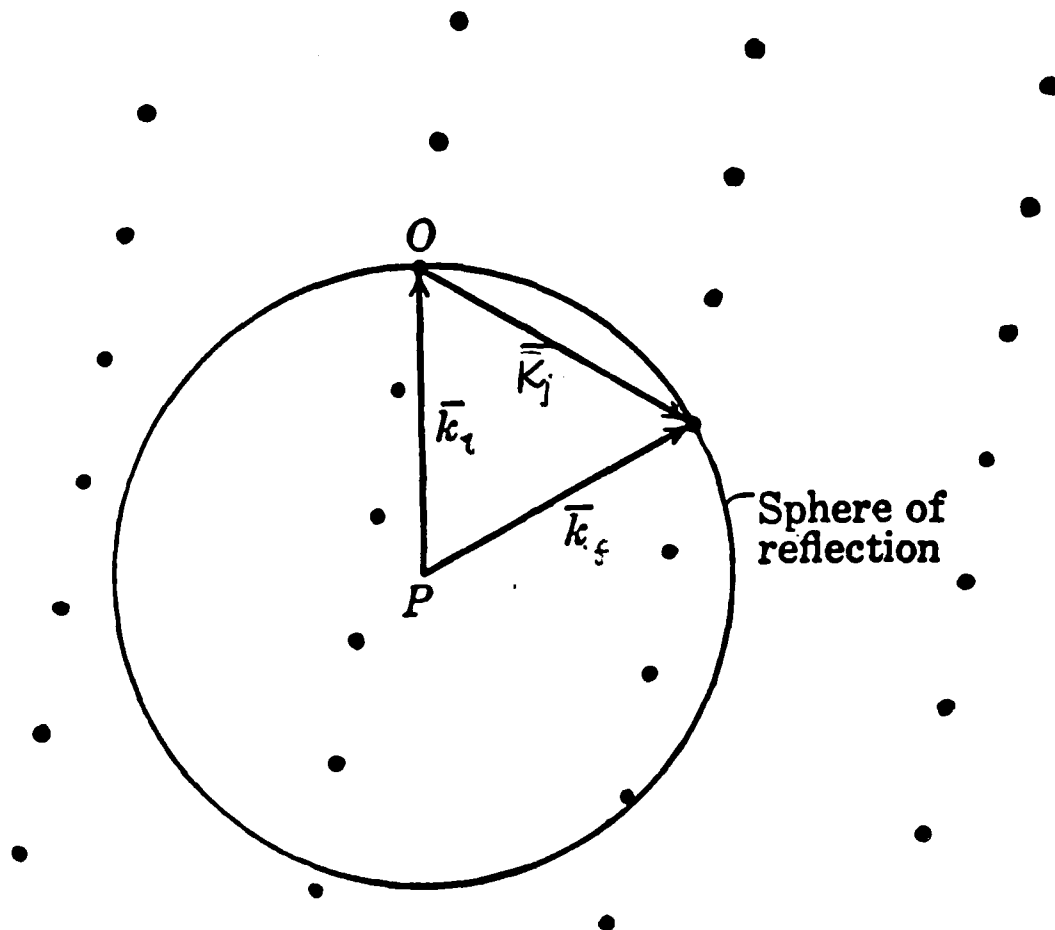


Figure 1. The "Ewald sphere" construction, drawn in two dimensions for clarity, with a reciprocal lattice based on a rectangular unit cell.

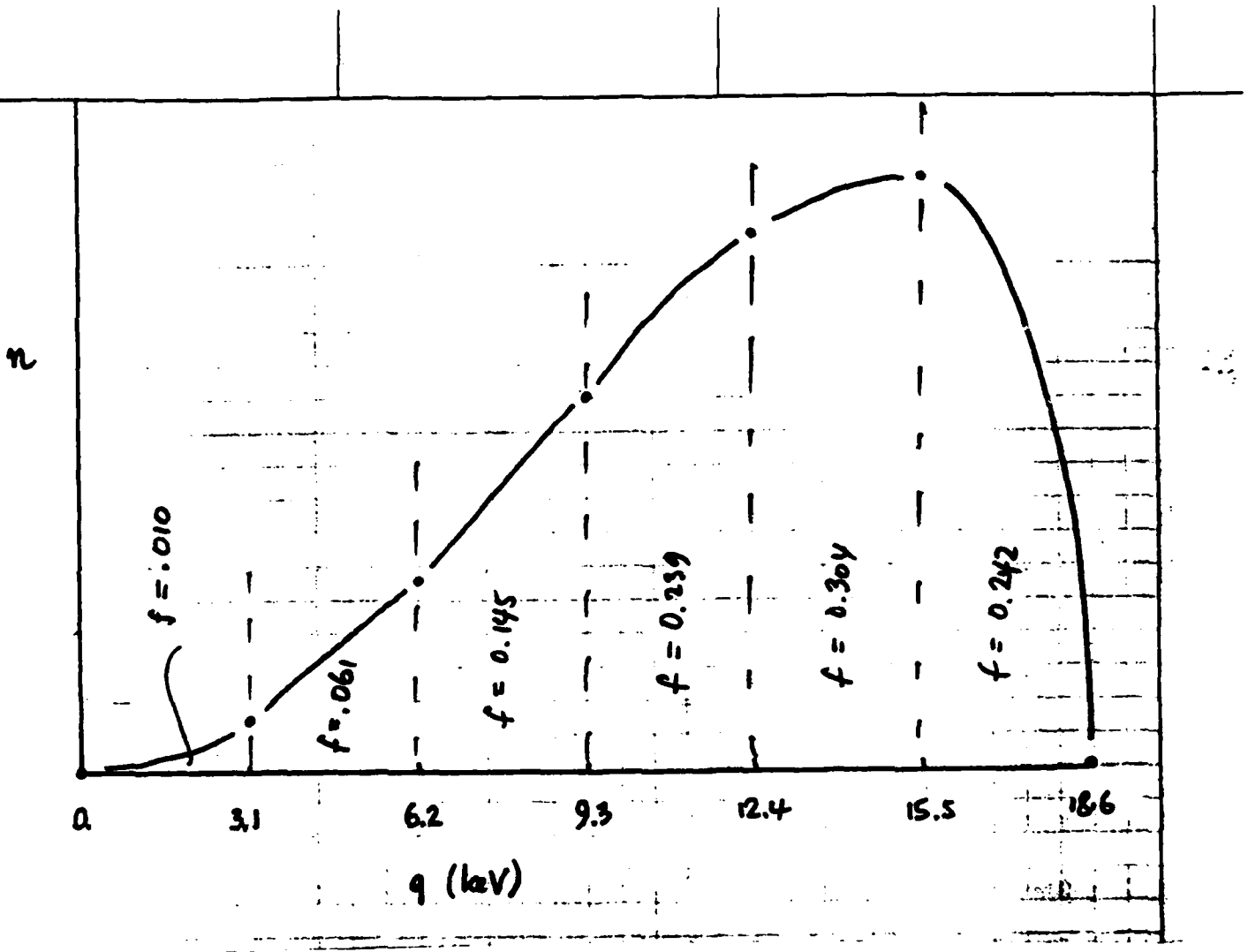


Figure 2. The energy distribution of neutrinos from tritium decay, showing six groups. The fractional population of each group f_i is also shown, normalized to unity.

Bibliography

1. J. Weber, Phys. Rev. D38, 32 (1988).
2. J. Weber, Found. Phys 14, 1185 (1984);
J. Weber, Phys. Rev. C31, 1468 (1985).
3. T. H. Ho, Phys. Lett. 168B 295 (1986); G. F. Bertsch and Sam M. Austin, Phys. Rev. C34 361 (1986).
4. R. Casella, Nuovo Cimento 94A 42 (1986); M. N. Butler, unpublished Caltech preprint, July 1986; H. J. Lipkin, Phys. Rev. Lett. 58 1176 (1987); Y. Aharonov, F. T. Avignone, A. Casher and S. Nussinov, Phys. Rev. Lett. 58 1173 (1987); G. T. Trammell and J. P. Hannon, Phys. Rev. Lett. 61 653 (1988).
5. The comparison with thermal neutron scattering is much less direct, due to the low velocity of the neutron. The time of flight of a thermal neutron past an atom is of order $\tau \approx 10^{-13}$ sec, which is much more than typical periods of atomic motions $T \approx 10^{-15}$ sec. This implies that significant energy transfers take place. For X-ray scattering, the transit time τ is of order 10^{-18} sec, much less than atomic periods, and the energy transfer is negligible.
6. W. H. Zachariasen, "Theory of X-Ray Diffraction in Crystals", John Wiley (1945).
7. A. H. Compton and S. K. Allison, "X-rays in Theory and Experiment", van Nostrand (1935).
8. L. D. Landau and E. M. Lifshitz, "Electrodynamics of Continuous Media", Addison-Wesley NY (1960); Chapter 15.
9. C. G. Darwin Phil. Mag. 27, 325 & 675 (1914); see also ref. 7 pages 376-380.

APPENDIX B

Estimate of X-ray Scattering from Crystals

by

Robert R. Lewis

Department of Physics
University of Michigan
Ann Arbor MI 48109

RR Lewis

June 15 1989

ABSTRACT

Both upper and lower estimates of the net force exerted on a sapphire crystal by X-rays from a tritium source are provided. The estimates are proportional to the unknown intensity of the flux of X-rays.

Introduction

I have already provided an estimate of the force exerted on a sapphire crystal by a beam of neutrinos, for use with the current experiment at LANL. It was based on several idealizations of the real experiment, and gave an *upper limit* to the actual force. Since the neutrino radiation pressure is predicted to be unobservably small, an upper limit was all that was needed. In this note, I will make a similar estimate of the force exerted by X-rays from the same source, to within an unknown factor of the X-ray intensity. Since the observed signal may be due to X-rays, both upper and lower limits are estimated.

X-ray Distribution

It is relatively easy to model the angular and energy distribution of the X-rays, but very difficult to predict their intensity. This permits us to calculate some of the important factors in the force; we will leave the overall X-ray flux density J_x as an unknown factor.

Since the source is isotropic, the angular distribution of the X-rays is uniform within the solid angle subtended by the target: $\Delta\Omega = 0.11$ radian². The energy distribution is harder to model, since the production of X-rays within the source is a complex process. X-rays are a secondary radiation, derived from the primary electron spectrum. The primary spectrum of non-relativistic electrons from tritium is

$$dN_e \propto p_e (Q - T_e)^2 dT_e \quad 0 < T_e < 18.6 \text{ keV}$$

where $T_e = p_e^2/2m$ is the electron kinetic energy and $Q = 18.6$ keV is the energy release in tritium decay. This distribution is zero at both ends and has a broad maximum at $T = Q/5 = 3.7$ keV; it is concentrated at lower energies than the neutrino energy spectrum. The bremsstrahlung cross section for production of X-rays is roughly independent of electron energy, but contains a factor $1/k$ which favors lower energy X-rays. The energy

spectrum for secondary X-rays should therefore be flatter than for the primary electrons. The simplest model for the X-ray energy spectrum is a constant, extending from zero up to the upper end point $k = Q = 18.6$:

$$dN_k \propto dk \quad 0 < k < 18.6 \text{ keV}$$

The calculation of the number of Bragg peaks can be computed in the same way as for neutrinos [1]:

$$N_B = (0.89) [4\pi \langle k^3 \rangle / 3] [b/2\pi]^3 = 0.0038 (Qb)^3$$

giving

$$N_B = 6800$$

Here $\langle k^3 \rangle = Q^3/4$ is the mean of the cube of the X-ray energy, which is proportional to the mean volume swept out by the "Ewald sphere"; the factor $[b/2\pi]^3$ gives the density of reciprocal lattice points within the sphere. The number of Bragg peaks is somewhat smaller for this X-ray beam than for the neutrino beam, because the energy spectrum concentrated at lower energies.

X-ray Cross-sections

The differential cross-sections for scattering X-rays from the atoms in a unit cell of sapphire can be over-estimated by setting the structure factors equal their upper limit:

$$\frac{d\sigma}{d\Omega} \leq (e^2/mc^2)^2 \sum_j Z_j^2 = 4.2 \cdot 10^{-23} \text{ cm}^2,$$

the summation being carried out over the different atoms in the unit cell [2Al + 3O]. For the entire crystal, the mean scattering cross-section under a single Bragg peak, can be evaluated by simply multiplying by the number of unit cells,

$$\bar{\sigma}_x = N \frac{d\sigma}{d\Omega} = 3.2 \text{ cm}^2$$

We are using the well known result [2] that the area under a single Bragg peak is proportional to the number of cells in the lattice, $N = N_A (13 \text{ gm}) / (102 \text{ gm}) = 7.7 \cdot 10^{22}$. Here 13 gm is the mass of the sapphire crystal, 102 gm the molar mass of the unit cell and N_A is Avogadro's number.

Net Force on Crystal

The net force on the crystal can now be over-estimated by combining the number of Bragg peaks N_B , the integrated cross-section per Bragg peak $\bar{\sigma}_x$ (cm^2), the mean momentum per X-ray $\langle hk \rangle = 5.0 \cdot 10^{-19}$ dyne-sec and the flux density J_x ($\text{cm}^2 \text{sec}^{-1}$), as follows:

$$F \leq N_B \bar{\sigma}_x \langle hk \rangle J_x = 1.1 \cdot 10^{-14} J_x \text{ (dyne)}$$

Role of Mosaic Structure, Extinction and Absorption

The discussion above provides an over-estimate of the expected force because it uses single scattering in an ideal lattice, neglecting several complicating effects which tend to reduce the scattering. One of these is lattice imperfections such as mosaic structure, which tilts the lattice planes. This seriously reduces the peak intensity of the Bragg scattering, but not the integrated intensity; we can ignore the mosaic structure of the lattice. Another is absorption of X-rays from the photo-effect, which causes an exponential absorption of the incident X-ray beam. The absorption length is typically of order 10 cm; we can also ignore this for a crystal with dimensions of a few centimeters. The extinction of the incident beam by scattering in the Bragg peaks cannot be neglected; the simplest evidence of this is that the integrated cross section is comparable to the geometrical cross section of the crystal itself.

We have previously used the Darwin model [3] to estimate the extinction length. Using the same method as before [reference 1, equation (X15)], we can under-estimate this as:

$$l_x \geq (n \lambda f_x)^{-1} = 5 \cdot 10^{-4} \text{ cm}$$

This is an under-estimate because we have assumed complete coherence in the evaluation of the scattering amplitude f_x , which would be reduced by the mosaic structure of a real crystal.

The neglect of extinction leads to an over-estimate of the force: only the atoms within a layer of thickness l_x will scatter as we have estimated. Therefore, we can get a lower limit to the force by taking a crystal with thickness l_x , which is about 10^{-8} of the actual dimension. Our final estimate of the force is:

$$1.1 \cdot 10^{-14} J_x \geq F \geq 1.1 \cdot 10^{-17} J_x \text{ (dyne)}$$

We see that a force of *micro*-dynes, would require a flux in the range

$$10^{+11} \geq J_x \geq 10^{+8} \text{ X-ray/cm}^2\text{-sec}$$

which should be readily detectable by other means.

References

1. R. R. Lewis, Addendum to Report "On the Scattering of X-rays and Neutrinos in Crystals", June 1 1989.
2. L D Landau and E M Lifshitz, "Electrodynamics of Continuous Media", Addison-Wesley NY (1960); Chapter 15.
3. C G Darwin, Phil. Mag. 27, 325 & 675 (1914);
A H Compton and S K Allison, "X-rays in Theory and Experiment", van Nostrand (1935); pp 376-380.

APPENDIX C (*)
COMMENTS ON THE RESULTS OF THE MEASUREMENTS CARRIED-OUT
AT LANL/TA-33 DURING FALL 1988

The measurements with the torsion balance carried out at LANL/TA-33 by using tritium and deuterium sources mounted on the 1 RPM rotating table have been performed only once and they must be repeated several times in the forthcoming 6-month program extension, before they can be considered fully probative evidence. In addition, there were several flaws in the functioning of the torsion balance and of the data collection system, which must be removed before resuming the measurements. We will come back to this point of the required instrumentation improvements, later-on in this Appendix.

With the caveat above, lets assume, for the sake of an interim discussion before the resumption of the tests at LANL, that the following two facts are real:

(a) There is a repulsion force when experimenting with the tritium, as compared with the observations made with deuterium. The intensity of this force is of a few microdynes, in agreement therefore with the observations made by Prof. Weber at University of Maryland;

(b) The repulsion force seems to disappear when a 1/4" lead shield is wrapped around the torsion balance.

Should the results (a) and (b) above be confirmed by the forthcoming tests (to be carried out with the improved instrumentation and, most important of all, with the 26 replicas mounted on the 1 RPM table, in order to substantially decrease the unwanted signals due to gravity gradients), the question will arise as to the origin of a radiation pressure that produces a force of a few microdynes on the torsion balance, and then disappears when the lead shield is interposed between source and sensor. We do not expect the answer to this question will be easy.

(*) Contributed by M. D. Grossi, P.I.

The first candidate radiation that comes to mind is X-ray radiation. It was to better understand X-ray induced radiation pressure, as compared to neutrino-induced forces, that Bob Lewis wrote Appendix A, its Addendum, and Appendix B (see Table I, Table II and Table III of this Appendix C for numerical estimates worked out on the basis of Bob Lewis formulas). If what we have observed is indeed X-ray radiation, where do these X-rays come from? Could it be that the X-rays produced by bombardment of the inner spherical wall of the tritium container by the beta-decay electrons leak through the wall? Hardly so. The attenuation of 10 KeV X-rays through the stainless-steel wall of the container, whose thickness (nominal value) is 0.66 cm, amounts to:

$$e^{-\frac{\mu_0}{\rho} \rho \Delta x} = e^{-(250 \text{ cm}^2 \text{ gr}^{-1}) \cdot (7.87 \text{ gr cm}^{-3}) \cdot (0.66 \text{ cm})} = e^{-1300}$$

(another estimate would give e^{-440} , still a leak-proof situation). Unless the information that we obtained at LANL/TA-33 is grossly incorrect, we cannot expect any detectable X-ray leak from the inside of the container.

What else could it be? A supposition that involves a rather exotic mechanism, has been formulated by Richard Maltrud, a physicist at LANL/TA-33, who has been experimenting for about eight years with muon-catalyzed low-temperature fusion (in cooperation with Dr. S. E. Jones of Brigham Young University). According to Dick Maltrud, the tritium container that we have used in our tests may contain some impurities of deuterium. Muons present in the cosmic-ray background, which are relatively abundant at Los Alamos (because of its altitude above sea level of 7,700'), could catalyze inside our container d-t fusion reactions with the consequence of generating 14.1 MeV neutrons.

These neutrons could induce radioactivation of the components mounted in proximity of the source, generating beta and gamma radiation that, directly or indirectly, could produce a radiation pressure on the torsion balance that would vanish when the lead shield is interposed. A quantitative estimate of this effect has not yet been performed, and this should be done as a part of the forthcoming added-scope effort,

if the results of the measurements warrant it (see later-on in this Appendix).

Thus far, we did not formulate other hypotheses of the possible mechanism(s) active here, but we will continue to think about the possible causes of the observations in the forthcoming effort.

As a result of the thinking above, we suggest that the instrumentation system in use at TA-33 should be complemented with additional sensors: a proportional counter, an X-ray detector, a neutron spectrometer, etc., characterized by the appropriate sensitivity and spectral response. Suitable instrumentation already exists at LANL and could be assigned for a few months to our project at TA-33. We have already asked Dick Maltrud to explore this possibility, and he has indicated that there is some chance of success.

To summarize our recommendations, we should proceed as follows:

STEP # 1 - Improve Instrumentation System

(a) Torsion Balance

- add thermal control
- increase damping factor
- determine experimentally the time delay between application of torque and appearance of signal at the output of the servo
- remove DC drifts, if possible

(b) Data Acquisition System

- reduce the 60 cps noise at input of preamplifier down to the rms value of thermal noise (a reduction by a factor of about 5 would be desirable)

(c) 1 RPM Rotating Table

- mount the 26 replicas of the source on the table top, to minimize amplitude of unwanted gravity gradient signals

- (d) Add an Uninterrupted Power Supply System (UPS)

STEP # 2 - Augment the Instrumentation System with New Sensors

- add a proportional counter
- add X-ray detector
- add neutron spectrometer
- add calorimeter to measure heat radiated by source container

STEP # 3 - Construct and Install Radiation Shields

- install IR shield and magnetic shield (already available)
- install lead shield (already available)
- construct and install cadmium/boron/lead shield

(STEPS #1, #2 and #3 can be performed at the same time)

STEP # 4 - Perform Data Acquisition with Tritium and Deuterium sources, as Done in Fall 1988

STEP # 5 - Carry Out Theoretical Work to Interpret the Observations

The specifics of this theoretical activity depends upon the results of the measurements.

- (1) Should the recordings with the tritium and deuterium sources be identical, with or without shields, we would have to conclude that there is no repulsion force. Further theoretical work and experimentation with the torsion balance would not be warranted.

- (2) Should we observe a repulsion force with and without shields, we would have a candidate neutrino event. It would be vital, at this point, to verify with great care the output of the radiation sensors (these will always be in operation when we collect data) in order to exclude any other cause for the observed effect.

- (3) Should we observe a repulsion force without the shield, and should the force vanish with the shield, our task is not yet over: we must formulate an explanation of what is happening, with the aid of the output of the radiation sensors.

We will go through the above steps several times to make sure that there is a clear repeatability of the experiment results. Shields will be interposed, removed, and interposed again to verify that their effects stay the same, thus giving a reliable answer to the project's basic questions.

TABLE I
 BASIC CHARACTERISTICS OF THE TRITIUM SOURCE

● Mass of Tritium	10.5 gr (November 1988)
● Conversion Factor to Curie	9.589 10^3 curie/gr
● Source Intensity	100.6845 Kilocurie
● Neutrino Intensity	$I = 3.42 \cdot 10^{15} \overline{\gamma} \text{sec}^{-1}$
	(1 curie = $3.4 \cdot 10^{10}$ dissociations/sec)
● Flux at a Distance $r = 12.22$ cm	$J = \frac{3.42 \cdot 10^{15}}{4 \pi r^2} = 1.8225 \cdot 10^{12}$ cgs

TABLE II

COMPUTATION OF THE RADIATION PRESSURE (FORCE IN DYNES)
DUE TO NEUTRINOS

(Based on Bob Lewis Theory in APPENDIX A and its Addendum)

$$F_{\nu} = J \cdot \sigma \cdot \frac{E}{c} \cdot \frac{N}{A} \cdot M \cdot \text{Bragg} \quad (\text{dynes})$$

where $J = 1.8225 \cdot 10^{12}$ cgs

$$\sigma = 2 \cdot 10^{-45} \text{ cm}^2$$

$$\frac{E}{c} = \frac{7 \text{ KeV}}{c} = 0.373 \cdot 10^{-18} \text{ cgs}$$

$$\frac{N}{A} = 0.8 \cdot 10^{22} \text{ atoms/gr}$$

$$M = \text{Mass of target} = 26 \text{ gr}$$

$$\text{Bragg} = \text{Bragg enhancement factor} = 10,670$$

Therefore:

$$\begin{aligned} F_{\nu} &= 1.8225 \cdot 10^{12} \cdot 2 \cdot 10^{-45} \cdot 0.37 \cdot 10^{-18} \cdot 26 \cdot 10,670 \cdot 0.8 \cdot 10^{22} = \\ &= 3 \cdot 10^{-24} \text{ dynes} \end{aligned}$$

TABLE III
 COMPUTATION OF THE RADIATION PRESSURE (FORCE IN DYNES)
 DUE TO X-RAYS
 (SEE APPENDIX B)

This is a summarization of the calculations performed by Bob Lewis in Appendix B. He endeavored to answer the question: "What should be the required intensity of the X-ray flux to illuminate the crystal of the torsion balance, whatever its origin, in order to produce a repulsion force F on the order of a microdyne?".

Lewis established an upper limit for the force F, as follows:

$$F \leq N_b \bar{\sigma}_x \langle \hbar k \rangle J_x \quad (\text{dyne})$$

Where: N_b is the number of Bragg peaks

$\bar{\sigma}_x$ (cm^2) is the integrated cross-section for a Bragg peak
 $\langle \hbar k \rangle = 5.0 \cdot 10^{-19}$ dyne.sec, is the X-ray mean momentum.

Therefore:

$$F \leq 1.1 \cdot 10^{-14} J_x \quad (\text{dyne}).$$

The lower limit for this force was derived by assuming that the thickness of the crystal is as small as the extinction length $l_x = 5 \cdot 10^{-4}$ cm (this is about 10^{-3} of the actual dimensions of the crystal). Consequently, the range of values that we should expect for the force F is:

$$1.1 \cdot 10^{-14} J_x \geq F \geq 1.1 \cdot 10^{-17} J_x \quad (\text{dyne}).$$

To conclude, in order to justify an observed force F on the order of a microdyne, the X-ray flux must be in the range of values:

$$10^{11} \geq J_x \geq 10^8 \quad (\text{X-ray}/\text{cm}^2 \cdot \text{sec}).$$

With appropriate instrumentation mounted in the vicinity of the torsion balance, it should be relatively easy to observe a flux of this intensity.